Influence of defects, phonons and strain on the luminescence properties of nitride- and arsenide-based quantum dots

vorgelegt von
Diplom-Physikerin

Irina A. Ostapenko

aus Apatity

Von der Fakultät II - Mathematik und Naturwissenschaften
der Technischen Universität Berlin
zur Erlangung des akademischen Grades
Doktor der Naturwissenschaften

- Dr. rer. nat. -

genehmigte Dissertation

Promotionsausschuss:

Vorsitzender:
Prof. Dr. Dieter Breitschwerdt

Gutachter:
Prof. Dr. Dieter Bimberg
Prof. Dr. Axel Hoffmann
Prof. Dr. Jürgen Christen

Tag der wissenschaftlichen Aussprache: 27.04.2012

Berlin 2012

D 83

Influence of defects, phonons and strain on the luminescence properties of nitride- and arsenide-based quantum dots

Irina A. Ostapenko

Technical University Berlin
Berlin 2012

'What do you mean by that?'
said the Caterpillar sternly.
'Explain yourself!'

Alice's Adventures in Wonderland, Lewis Carroll

Abstract

This work presents the results of experimental investigations of the luminescence properties of two important quantum dot (QD) material systems by means of cathodoluminescence (CL) spectroscopy. Nitride-based QDs are prospective for quantum-communication applications at elevated temperatures due to their large localization energies. Site-controlled InGaAs/GaAs QDs present an example of a novel "bottom-up" approach for deterministic QD alignment. This method, based on strain-modulation controlled QD nucleation, is generally applicable to lateral positioning of nanostructures. The experimental results are substantiated with numerical calculations, some of which are presented for the first time within the frame of this work.

Different manifestations of the so-called spectral diffusion (SD) - the variation of the single QD luminescence under influence of stochastic fluctuations of electric fields in the QD environment - were investigated. The dependence of SD on various excitation conditions and sample fabrication methods was analyzed for nitride-based QDs. The origin of different components of SD is discussed in terms of different defect types. For the spectral jitter of QD emission lines, which can be resolved in the spectroscopic experiments, a model of a moving charge is proposed. The analysis of the spectral jitter of the QD emission lines allows to conclude about the QD excitonic dipole-moment, induced by piezo- and pyroelectric fields.

It is shown, that a large emission linewidth appears to be intrinsic property of the nitride material system using current fabrication methods and is present even in case of resonant excitation of the QD. From the spectral jitter of the emission lines, stemming from the excitonic transitions of the same QD, the ratio of the built-in dipole moments of the respective excitonic complexes can be determined quantitatively. Built-in dipole moments of various excitonic complexes from the same dot are shown to differ significantly. A special type of spectral jitter, reported for the first time in this work, allows to estimate the absolute value of the excitonic built-in dipole moment without applying external electric field.

Interaction of excitons and acoustic phonons is investigated in detail in a combined experimental and theoretical survey for the first time for GaN/AlN QDs, where the impact of vertical and lateral charge-carrier confinement on the coupling mechanisms is analyzed. The independent Boson model using realistic wave-functions from 8-band $\mathbf{k} \cdot \mathbf{p}$ theory accounts very well for the experimental observations of the shape and position of the phonon side-bands. The intensity ratio of the zero-phonon line

and phonon side-band as obtained from the numerical results matches measured data only when SD-induced line broadening is superimposed. The importance of taking SD into account in case of nitride-based QDs is again emphasized and its major impact on the inhomogeneous line broadening is proven. The analysis of temperature dependence of the emission linewidth shows a major role of acoustic phonon scattering for broadening of the linewidth, while the contribution of optical phonons can be neglected here.

Spatially-resolved CL showed itself as a very useful technique for the investigation of the first test-structures of positioned QD. The feasibility of the growth concept is proven on the example of InGaAs/GaAs QD material system. The unambiguous influence of the strain from the buried stressor structure on luminescence properties, such as spectral diffusion and ensemble polarization, is evidenced. CL experiments reveal the formation of different QD luminescence bands, which can be clearly distinguished spectrally and spatially in strong correlation with the stressor position. The possibility to control properties of QD and their formation by means of strain from a buried stressor structure, appears an important step on the way to tailoring single-QD-based devices with desirable properties.

Zusammenfassung

Diese Arbeit stellt die Ergebnisse der experimentellen Untersuchungen der Lumineszenzeigenschaften von Halbleiterquantenpunkten (QP) vor. Zwei wichtige Materialsysteme stehen im Mittelpunkt dieser Arbeit. Beide Systeme sind für die Entwicklung von Anwendungen im Bereich der Quantenkryptografie und Quantencomputer von großer Bedeutung: Nitrid-basierte QP sind wichtige Kandidaten für die Anwendbarkeit bei Raumtemperatur. Am Beispiel des Materialsystems InGaAs/GaAs wurde ein neuer Ansatz der Herstellung positionierter QP untersucht. Für die optische Charakterisierung wurde Kathodolumineszenzspektroskopie (KL) benutzt, da sie eine hohe Orts- und Spektralauflösung bietet. Um die experimentellen Beobachtungen einzuordnen, wurden verschiedene Modellrechnungen durchgeführt und deren Ergebnisse werden zum ersten Mal im Rahmen dieser Arbeit präsentiert. Dabei vermittelt die gesamte Analyse ein besseres Verständnis der untersuchten Prozesse.

Stochastische Fluktuationen lokaler elektrischer Felder in der Umgebung von QP beeinflussen die Lumineszenzenergie, dieser Effekt ist als spektrale Diffusion (SD) bekannt. Die Auswirkungen der SD auf die Lumineszenz Nitrid-basierter QP wurden untersucht. Die vorliegende Arbeit liefert umfangreiche Ergebnisse und Diskussionen zu unterschiedlichen Typen von SD und führt deren möglichen Ursprung auf bestimmte Arten von Defekten zurück. Es wurde festgestellt, dass die großen Linienbreiten auch bei resonanter Anregung auftreten und für die Nitrid-basierten QP, die mittels heutigen Verfahren gewachsen werden, eine charakteristische Eigenschaft darstellen. Ein spezielles Muster im zeitlichen Verlauf der Lumineszenz einzelner QP wird zum ersten Mal beschrieben, ein Model als Erklärung für diese Änderung der Linienlage wird vorgestellt und durch Simulationsrechnungen verifiziert. Pyro- und piezoelektrische Felder in den Nitrid-basierten Heterostrukturen verursachen eine räumliche Trennung der Wellenfunktionen der Ladungsträger in den QP. Für die resultierenden Dipolmomente exzitonischer Komplexe in einzelnen QP wurde aus den Experimenten anhand der SD sowohl die Größe als auch das relative Verhältnis identifiziert.

Die Wechselwirkungen zwischen Exzitonen, eingeschlossen in AlN/GaN QP, und elementaren Gitterschwingungen wurden untersucht. Temperaturabhängige Messungen und spezielle Modelrechnungen zeigen die verstärkte Kopplung an akustische Phononen. Eine detaillierte Analyse der Kopplungsmechanismen in Abhängigkeit von Größe und Form eines QPs wurde mit Hilfe des Independent Boson Modells durchgeführt. Diese Rechnungen benutzen realistische Wellenfunktionen aus

8-Band $\mathbf{k} \cdot \mathbf{p}$ Rechnungen in der Hartree-Fock Näherung als Eingangsparameter und berücksichtigen außerdem die durch die SD verursachte inhomogene Linienverbreiterung. Die Simulationsergebnisse zeigen eine sehr gute Übereinstimmung mit dem Experiment.

KL Untersuchungen haben bestätigt, dass der Einsatz vergrabener Stressor-Strukturen unter einer QP-Schicht das Wachstum der QP steuern kann. Die Ergebnisse deuten darauf hin, dass sich die QP in starker Korrelation mit der Position des Stressors bilden. Die durch den Stressor erzeugte Verspannung im Material beeinflusst auch die optischen Eigenschaften der positionierten QP. So wurden ortsabhängige systematische Variationen der QP nachgewiesen, die sich in der Emissionsenergie, der SD und der Polarisation zeigen. Da die in dieser Arbeit untersuchte Methode des kontrollierten Wachstums von QP auch in anderen Materialsystemen anwendbar ist, erscheint dieses Verfahren ein bedeutender Schritt für die Entwicklung von Anwendungen, die auf einzelnen positionierten QP basieren, die bestimmte optische Eigenschaften aufweisen sollen.

List of publications

Parts of this work were published in the following articles in the scientific journals:

- *"Lateral positioning of quantum dots using a buried stressor"*
  André Strittmatter, Andrei Schliwa, Jan-Hindrik Schulze, Tim David Germann, Alexander Dreismann, Ole Hitzemann, Erik Stock, Irina A. Ostapenko, Sven Rodt, Waldemar Unrau, Udo W. Pohl, Axel Hoffmann, Dieter Bimberg, Vladimir Gaisler, Applied Physics Letters **100**, 093111 (2012).
- *"Exciton acoustic-phonon coupling in single GaN/AlN quantum dots"*
  Irina A. Ostapenko, Matthias-René Dachner, Gerald Hönig, Sven Rodt, Andrei Schliwa, Marten Richter, Satoshi Kako, Andreas Knorr, Yasuhiko Arakawa, Axel Hoffmann, Dieter Bimberg, Physical Review B **85**, 081303 (R) (2012).
- *"Large internal dipole moment in InGaN/GaN quantum dots"*
  Irina A. Ostapenko, Gerald Hönig, Christian H. Kindel, Sven Rodt, André Strittmatter, Axel Hoffmann, and Dieter Bimberg, Applied Physics Letters **97**, 063103 (2010).

Contents

Introduction 1

Objectives of the work 4

Outline 6

Fundamentals 7

1 Theoretical background 9

1.1 Quantum dot in a nutshell 9

1.1.1 Quantum dot growth principles 9

1.1.2 "Artificial atom" 10

1.1.3 Quantum dots as single/entangled photons sources 13

1.1.4 Nitride-based quantum dots 15

1.2 Interaction of excitons in quantum dots and lattice vibrations 17

1.3 Quantum dot in an electric field 20

1.3.1 Quantum confined Stark effect 20

1.3.2 Spectral diffusion 21

1.3.3 Nitride-based quantum dots and electric fields 22

1.4 Homogeneous line broadening 24

Experimental 27

2 Experimental set-up, numerical methods, samples 29

2.1 Cathodoluminescence spectroscopy 29

2.2 Probing a single quantum dot 34

2.3 Numerical modeling 35

2.3.1 Strain distribution 35

2.3.2 Wave-function 36

2.3.3 Exciton-phonon interaction 37

2.4 Growth of nitride-based samples 39

Results: nitride-based quantum dots **47**

3 Interaction with local electric fields **49**
3.1 State of the art . . . 50
3.2 Short-timescale spectral diffusion (line broadening) . . . 54
3.2.1 Influence of sample surface . . . 56
3.2.2 Influence of excitation density . . . 57
3.2.3 Influence of temperature . . . 60
3.2.4 Influence of excitation mechanism . . . 61
3.2.5 Discussion: defects . . . 63
3.3 Long-timescale spectral diffusion . . . 64
3.3.1 On/off blinking . . . 65
3.3.2 Spectral jitter . . . 67
3.3.3 Influence of the excitonic dipole moment . . . 70
3.3.4 Influence of the excitation conditions . . . 74
3.4 Dipole-moment-induced oscillations of emission energies . . . 75
3.4.1 Model of a moving charge . . . 76
3.4.2 Modeling of the energetic shift . . . 78
3.4.3 Estimation of the dipole moment from experiment . . . 80
3.4.4 Observation in other samples . . . 82
3.4.5 Discussion: defects . . . 85
Conclusion . . . 87

4 Interaction with acoustic phonons **89**
4.1 State of the art . . . 90
4.2 Experiment and modeling . . . 92
4.2.1 Low-energy side-band and its temperature dependence . . . 92
4.2.2 Exciton acoustic-phonon coupling modeling . . . 93
4.2.3 Calculated spectra . . . 94
4.2.4 Including spectral diffusion . . . 96
4.3 Influence of charge carrier confinement . . . 97
4.3.1 Investigated dot series and calculated luminescence spectra . . . 97
4.3.2 Influence of dot geometry on coupling mechanisms . . . 99
4.3.3 Line-shapes in dependence on emission energy . . . 100
4.3.4 Discussion . . . 103
4.4 Influence of temperature . . . 104
Conclusion . . . 108

Results: site-controlled arsenide-based quantum dots **109**

5 Strain-induced growth and luminescence properties **111**
5.1 State of the art . . . 112

5.2 Strain engineering by buried stressor . . . 113
5.2.1 Concept . . . 113
5.2.2 Strain distribution calculations . . . 114
5.2.3 Quantum well test-structures . . . 116
5.3 Site-controlled quantum dot growth . . . 118
5.3.1 Sample fabrication . . . 118
5.3.2 AFM investigations . . . 119
5.4 Site-dependent luminescence properties . . . 120
5.4.1 Spatial distribution of luminescence . . . 120
5.4.2 Quantum dot luminescence bands . . . 124
5.4.3 Spectral diffusion . . . 127
5.4.4 Strain-induced polarization . . . 128
Conclusion . . . 133

Summary and outlook **135**

Appendix **141**

Acknowledgments **143**

Abbreviations **144**

Bibliography **147**

Introduction

Introduction

The onrush of modern data communication has moved information technology and opto-electronic device industry into leading economical sectors. Physics of semiconductor nanostructures has achieved a tremendous importance in the last decades. Intensive fundamental investigation of semiconductors is constantly giving rise to novel areas of their application. A number of nanotechnological inventions have revolutionized microelectronics and information technology: in this context quantum well lasers, high-power quantum-well based light emitting diodes, computer read-write disk heads can be named. Giant magnetoresistance effect enabled high capacity computer hard drivers and was acknowledged by Nobel Prize in Physics in 2007.

The ultimate example of quantum confinement in semiconductor heterostructures is a quantum dot (QD). Its size in the order of a few nanometers, allows confinement of charge carriers in all three dimensions and opens a door to completely new physical properties. A QD is an excellent model system to investigate quantum mechanical laws of finite fermionic systems. The development of this field of nanotechnology resulted in proposal of a number of interesting QD-based applications: photodetectors [Kom00, Kri05], semiconductor optical amplifiers [Bim05], nanocrystal solar cells [Noz02], QD lasers [Ara82, Bim97], QD memory device [Mar11].

QDs are promising candidates for quantum information applications (e.g. [Shi07, Bim09]). A single QD can be employed in secure quantum-key-distribution [Ben00]. Recently a large number of brilliant results have been reported, proving a QD as a robust single- and entangled-photon source for quantum communication [Loc06, Joh08, Sal10b].

Among various QD material systems III-V nitrides attract a particular attention. The luminescence of these QDs covers the spectrum from ultra-violet for GaN/AlN QDs [Kak04] to infra-red for InN/GaN QDs [Ruf07]. Large charge carrier localization energy allowed demonstration of single photon emission at 200 K from GaN/AlN QDs [Kak06]. Lasing operation of an optically pumped InGaN QD laser at room temperature was reported in [Tac99]. Long spin decoherence times [Kri03, Lag08] together with the stability of excitonic effects up to room temperature make nitride-based QDs suitable for quantum-communication and solid-state quantum computing systems [De 02, Win08].

In spite of the tremendous development of nitride-QD-based devices, many physical phenomena in these materials are still not fully understood. Some of the effects

arise from built-in electric fields of several MV/cm, present in nitride-based heterostructures, grown along the polar axis (0001). These fields originate from pyro- and piezoelectric effects of the wurtzite crystal structure and lead to a large spatial separation of the confined charge carriers within a QD structure. The resulting electron-hole dipole-moment makes the QD excitons very sensitive to variation of the external electric fields and also enhances the polar interaction of the excitons in the QD with lattice vibrations.

In contrast, the arsenide-based QD material system is far more investigated. A profound knowledge of the optical properties of In(Ga)As/GaAs QDs has been gained in recent years. Well optimized growth approaches for self-assembled QDs of this material system exist. However, many quantum information applications require precise positioning of a single QD and full control over its optical properties. The existing methods of site-controlled growth are predominantly based on sophisticated pre-patterning of the substrate, leading to limitation of the optical performance of the dots afterwards. Thus improvement of the optical quality of such site-controlled QD and a development of alternative methods is necessary.

Objectives of the work

For the last decades semiconductor heterostructures have been successfully studied and a significant progress has been achieved in the development of applications. Among others, QD structures are promising candidates for quantum information systems. The present work is dedicated to the investigation of the luminescence properties of two important QD-systems: nitride-based QDs and site-controlled arsenide-based QDs.

An experimental survey of the optical properties of single QDs by means of cathodoluminescence spectroscopy provides information about the properties of excitonic complexes in zero-dimensional QD-structures. For a substantial comprehension of the experimental observations the work is supported by numerical modeling. Particular electronic properties of single nitride-based QDs are obtained in the framework of 8-band $\mathbf{k} \cdot \mathbf{p}$ theory in combination with Hartree and Hartree-Fock approaches. Coupling of excitons, confined in GaN/AlN QDs, and acoustic phonons is modeled by the independent Boson model with realistic wave-functions for the first time. Continuum elasticity model is applied to simulate strain, induced on GaAs surface by a buried stressor. The joint analysis then contributes to a better understanding of the complex interaction of excitons confined in QDs and their environment. The present work addresses the following aspects:

- Interaction of charge carriers in QDs with fluctuating electric fields in the environment - the so-called spectral diffusion (SD).

What impact does SD have on the QD luminescence? Which parameters can influence the linewidth of emission lines? What information about the intrinsic properties of the system can be obtained from the observation of SD? Which mechanism is behind the SD? Can SD be eliminated?

Stable intensity and emission energy is a key point for potential implementation of QD. SD can be detrimental for single QD-based applications. Due to the strong pyro- and piezoelectric fields in the nitride-based heterostructure large built-in dipole moments are induced in the QDs. As a result, the excitonic emission is very sensitive to the changes of the electric fields in the environment and makes nitride-based QDs beneficial for the investigation of SD.

- Interaction of charge carriers in the QDs with the lattice vibrations.

  How do the acoustic phonons manifest themselves in the luminescence of single QDs? Which role do the different coupling mechanisms play? How does the confinement of charge carriers and QD morphology influence the interaction between acoustic phonons and excitons? How do phonons contribute to emission linewidth? Which part of the linewidth is related to inhomogeneous broadening?

  A thorough investigation of the influence of interaction with phonons is a prerequisite for development of single-QD devices. The impact of phonons on exciton dephasing becomes decisive at elevated temperatures and can be limiting for room temperature QD-applications. For the polar system of wurtzite nitride-based QDs different coupling strengths than for e.g. the InGaAs system are expected and exciton acoustic phonon interaction should be examined in details.

- Influence of the strain fields.

  Can the QD nucleation be controlled by a specific stressor layer underneath? Are these QDs of good optical quality and are they comparable to the "conventional" self-assembled QDs? How does the modulated strain of the stressor influence the QD nucleation and growth? What impact does the strain distribution have on the luminescence properties of the site-controlled QD?

  The existing methods of QD positioning involve sophisticated fabrication steps and still produce QDs of a low optical quality. The new approach, combining strain modulation and principles of self-assembled growth presents a promising alternative of site-controlled QD growth. InGaAs/GaAs system is a perfect candidate for the test implementation, since growth procedures of the QDs of this type are well established and the optical properties of InGaAs/GaAs QDs have been extensively studied. This facilitates the investigation of the impact of the modulated strain fields on the growth and luminescence of the site-controlled QDs.

One of the ultimate aims of the research community, this work belongs to, is a single-QD based device functioning at elevated temperatures. Nitride-based QDs are of tremendous importance for such applications and have to be explored more extensively. Thus one focus of the work is pointed to nitride-based QDs, which are not as broadly investigated as arsenide QDs. Robust single-QD devices on the basis of arsenide QDs already exist. However, fabrication of QDs with controlled position and desirable optical properties is still cumbersome. This work presents the results, which evidence the feasibility of the new site-controlled QD growth.

Outline

The thesis is divided into six chapters. Chapter 1 briefly introduces fundamental concepts of self-assembled QDs. Chapter 2 outlines cathodoluminescence spectroscopy, the experimental set-up and numerical methods, used in the subsequent analysis of experimental results. The growth and structure of the nitride-based samples is also presented in Chapter 2. A compact overview of the investigated samples can be found in the appendix on page 160.

Chapters 3 to 5 constitute the main part of the work, presenting the results of experiments and analysis. Each of the chapters begins with a brief overview of important surveys already reported and related to the main focus of the chapter.

The investigation of nitride-based samples is described in chapters 3 and 4: the results concerning interaction of the QDs with stochastic electric fields in the environment (spectral diffusion) are discussed in Chapter 3. Exciton-acoustic phonon coupling in GaN/AlN QDs follows in Chapter 4.

Chapter 5 describes the concept of site-controlled growth with a buried stressor and presents first test-structures, grown in the InGaAs/GaAs material system. The experimental investigations of these site-controlled QDs are presented and discussed.

The last Chapter summarizes the findings of the work and gives a conclusion as well as a brief outlook.

Fundamentals

1 Theoretical background

This chapter explains some fundamental concepts, important for understanding the experimental results of the present work. It is restricted to type-I self-assembled quantum dots (QDs). The method used to grow QDs is introduced briefly. The basic electronic properties of excitons confined in QDs and the resulting optical properties, important for the application of the single QDs, are explained. In a few words the essential features of group III-nitride materials are described. Influence of the interaction between excitons and external electric fields as well as lattice vibrations is explained. A more extensive description can be found in various textbooks on low-dimensional system physics or quantum dots, see e.g. [Bim98].

1.1 Quantum dot in a nutshell

1.1.1 Quantum dot growth principles

Modern epitaxial technologies make possible the precise atomic deposition and building of semiconductor heterostructures with desired compositions and dimensions. Metal-organic chemical vapor deposition (MOCVD) and molecular beam epitaxy (MBE) are regarded as first choice for the fabrication of optoelectronic devices.

Both techniques enable growth of high-quality materials and abrupt interfaces between semiconductor materials. In MBE atoms and molecules are directly evaporated onto the substrate in a high vacuum. In MOCVD under lower pressure more complex molecules are used, which then react chemically at the heated surface, and the semiconductor materials crystallize.

The atoms of one semiconductor deposited on another, would first adopt the structure of the substrate, even if the lattice constants differ. The lattice mismatch creates strain in the overgrown material. Strain increases with increasing thickness of the mismatched layer. Minimization of the overall free energy of the system triggers the transformation of the deposited structure. Competition between strain, surface, volume and chemical bonding energies can lead to the formation of three-dimensional islands.

In the present work QDs grown in the Stranski-Krastanow growth mode are investigated. The main steps of the growth process are shown in figure 1.1. The QD material is deposited onto the thick layer of the matrix material, which has a smaller

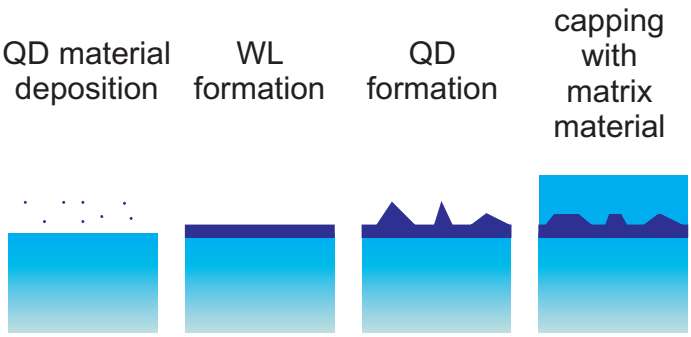

Figure 1.1: Steps of the self-assembled QD growth in the Stranski-Krastanow growth mode.

lattice constant than the QD material. A two-dimensional (2D) layer is formed, the so-called wetting layer (WL). Depending on surface energy and lattice parameters of both materials, it is favorable for the overgrown layer to build three-dimensional (3D) islands on a nanometer scale to reduce the total energy. These islands - QDs - are capped with a certain amount of matrix material to avoid recombination of the charge carriers in the surface states. The capping process can change the form of the free-standing islands.

Localization of charge carriers can also take place in alloy fluctuation within a thin layer of ternary material, embedded into a matrix with a smaller lattice constant. The best example are InGaN QDs, where the varying concentration of In in a thin 2D InGaN-layer deposited on the GaN [Bar07] result in optical properties very similar to the Stranski-Krastanow QDs.

For numerous applications controlled positioning of a single QD as well as small distribution of the QDs in size is desired. A number of methods are being developed to pre-define the QD nucleation. This can be achieved e.g. by patterning of the substrate by means of lithographic techniques, etching methods etc. Details are discussed in chapter 5.

1.1.2 "Artificial atom"

A layer of material embedded in another material with a larger band gap constitutes a potential well for charge carriers. If the dimension of the inclusions is in the range of the charge carrier de-Broglie wavelength, quantum effects dominate the optical and electronic properties of the resulting heterostructure. In case of the QD the charge carriers are confined in all three spatial directions. The size of the dots is in the nanometer range. The wave-functions of the charge carriers extend no longer over the crystal, as is the case in bulk material, but are spatially localized. The density of states is represented by δ-functions. The electronic states are quantized,

leading to discrete transition energies of the electron-hole recombinations. Due to their similarity to atoms, the QDs are called “artificial atoms”.

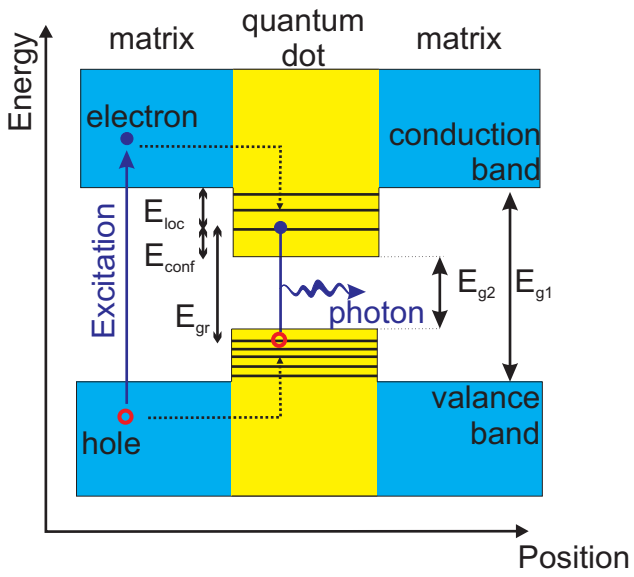

Figure 1.2: Schematic energy diagram of a QD (type I).

A QD represents an actual example of the quantum mechanical problem known as “particle in the box”. A simplified energy diagram of a type I QD is shown in figure 1.2. Here the E_{g1} of the matrix (also barrier) material is larger then E_{g2} of the QD material. The solution of the Schrödinger equation for a confined charge carrier results in discrete energy levels. The holes have a larger effective mass in comparison to electrons, therefore the holes are stronger confined, and the hole energy levels are more closely spaced. A few of the energy levels are shown in the figure. The confinement energy E_{conf} denotes the increase of the ground level of a confined charge carrier relative to a free particle. The localization energy is the distance between the ground state and the respective band edge of the matrix material. In the figure E_{loc} and E_{conf} are indicated for the electrons. Electrons and holes, generated in the matrix material, can be captured in the QD. When an electron and a hole in ground states recombine, i.e. the electron lowers its energy in E_{gr}, a photon is emitted.

Due to strong confinement, the Coulomb interaction between the single particles plays a significant role. Electrons and holes form new quasi-particles, so-called excitonic complexes. The two-particle system, consisting of one electron and one hole, is called exciton (labeled X throughout the present work). It is described by the Hamiltonian:

$$H_X = H_e + H_h + H_{Coul} \tag{1.1}$$

where H_e and H_h are the Hamiltonians of electron and hole and H_{Coul} is the energy of Coulomb interaction between them. The attractive Coulomb interaction lowers the total energy of the electron-hole pair. Similar to the bulk exciton the Coulomb term defines the binding energy of the exciton. However, in contrast to the bulk no "free" charge carriers can exist in the dot. The energy of the photon, emitted at recombination of the electron and a hole is then $E_{gr} - H_{Coul}$ (see figure 1.2: this energy is larger than the band gap E_{g2}).

The optical properties of single QDs strongly depend on their morphology: composition, strain, size and form. The composition determines the QD transition energy due to band gaps of the matrix and the dot materials. The strain fields, induced by a mismatch of the lattice constants, also influence the band gap parameters of the heterostructure. The confinement energy is determined by the size of the dot: smaller QDs have larger E_{conf}, hence larger E_{gr}. The shape of the QD influences the spatial distribution of wave-functions of the charge carriers, and thus the oscillator strength of the electron-hole recombination. When exchange interaction is taken into account, the degeneracy of the energetic levels strongly depends on the symmetry of the dot.

Self-organized QDs vary in height, lateral size and shape. Since each QD exhibits different excitonic transition energies with different oscillator strengths, single emission lines with different spectral positions and intensity are observed in the luminescence experiments. If all the lines superimpose, an inhomogeneously broadened ensemble peak is detected.

The excitonic complexes consisting of three charge carriers are called trions: X^+ (electron-hole pair and a hole) and X^- (electron-hole pair and an electron). Two pairs of electrons and holes form a biexciton, called XX in work. Addition of the further charge carriers leads to the formation of other multiexcitonic complexes. When one of the electron-hole pairs recombines, a photon is emitted, while the remaining charge carriers stay in the dot. The energy of the emitted photon, here also called the transition energy of the initial multiexcitonic complex, differs from the emission energy of a single electron-hole pair, forming an exciton. This difference is called binding energy of the multiexcitonic complex and can be both positive and negative.

For the (multi)excitonic complex consisting of n electrons and m holes, the following general description, similar to equation (1.1), is valid:

$$H_{ne,mh} = H_e + H_h + H_{Coul} = \sum_{1<i\leq n} H_e^i + \sum_{1<i\leq m} H_h^i +$$

$$\frac{1}{2} \sum_{\substack{1<i,j\leq n \\ i\neq j}} H_{e,Coul}^{i,j} + \frac{1}{2} \sum_{\substack{1<i,j\leq m \\ i\neq j}} H_{h,Coul}^{i,j} + \sum_{\substack{1<i\leq n \\ 1<j\leq m}} H_{e,h,Coul}^{i,j} \tag{1.2}$$

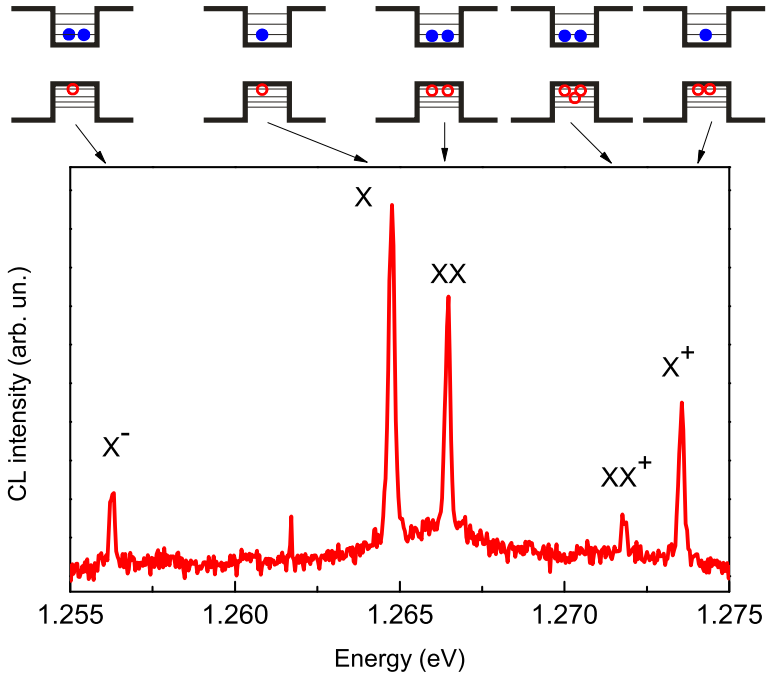

Figure 1.3: A luminescence spectrum of the InAs/GaAs QD from [Rod05] with indicated transitions of various excitonic complexes. CL - cathodoluminescence (see the next chapter).

Here H_e^i and H_h^i are the Hamiltonians of electrons and holes respectively, $H_{h,Coul}$ ($H_{e,Coul}$) is the energy of Coulomb repulsive interaction between the holes (electrons) and $H_{e,h,Coul}$ the energy of Coulomb attractive interaction between single electrons and holes. These Coulomb terms determine the binding energy and differ in magnitude due to different distributions of the wave-functions of single charge carriers. Consequently, the transition energies of different (multi)excitonic complexes vary, resulting in a number of single sharp lines in the luminescence spectra. Figure 1.3 shows an example of the real luminescence spectra of an InAs/GaAs QD with different transitions of excitonic complexes.

1.1.3 Quantum dots as single/entangled photons sources

Electrons and holes are fermions and obey the Pauli principle. An electron with a spin projection $s = \pm 1/2$ and a heavy hole with an angular momentum $j = \pm 3/2$ constitutes the ground state in the dot of the zinc-blende material system. The resulting exciton states are four-fold degenerated: two dark states with an angular momentum $M = \pm 2$, and two bright states with $M = \pm 1$. The bright states couple to an electromagnetic field, since a photon has a spin 1.

Additionally to Coulomb interaction the quantum mechanical exchange interaction

should be taken into account when describing the exciton quasi-particle. Exchange interaction mixes up the dark states and lifts up this degeneracy, creating a dark doublet ($|2\rangle \pm |-2\rangle$). The recombination of the electron and the hole of the exciton involving pure states results in luminescence with circular polarization. However, the lowering of the symmetry of the confinement potential below C_{3v} mixes up the bright states into a doublet ($|1\rangle \pm |-1\rangle$) too. The resulting energetic separation of these two states is called fine structure splitting (FSS). Recombination of the electron-hole pairs in the mixed states produces luminescence with linear polarization.

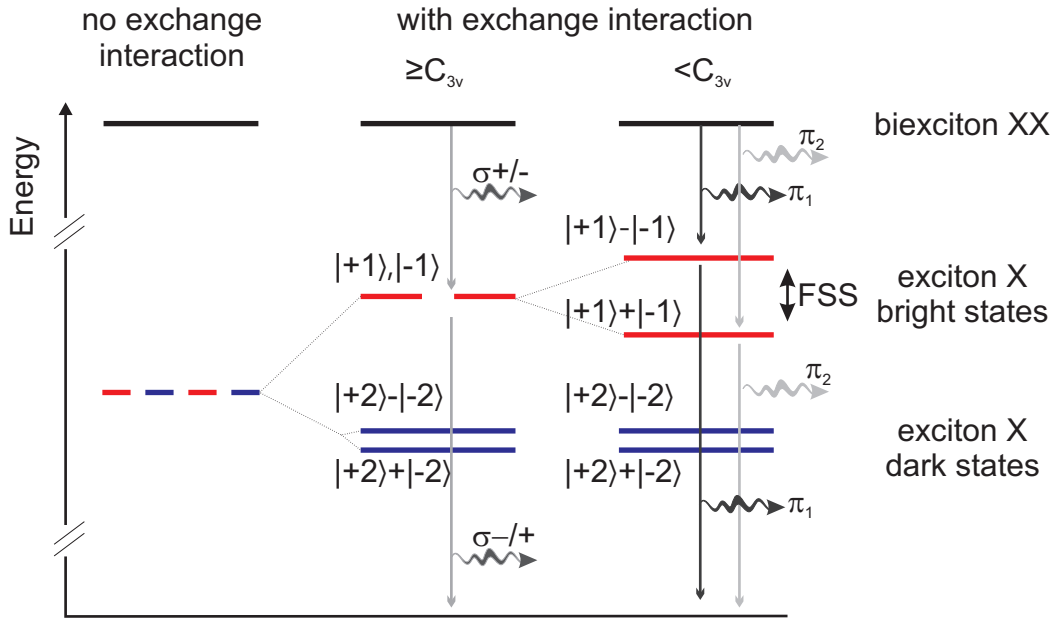

Figure 1.4: Energy schema of decay $XX \rightarrow X \rightarrow$ *empty dot*. $|M\rangle$ stays for total exciton angular momentum, C_{3v} - for confinement potential symmetry. $\sigma + /-$ denotes circular polarized light, $\pi_{1,2}$ - linear polarized light, here $\pi_1 \perp \pi_2$. (Figure adopted from [Tür01, Seg05]).

The anisotropy of the confining potential results from strain-induced piezoelectric fields and structural elongation. The polarization directions are parallel and perpendicular to the anisotropy axes of the confining potential. In the zinc-blende material system in the growth direction [001] these axes are [110] and [1$\bar{1}$0].

The spin number of the biexciton is zero and there is no exchange interaction splitting of the biexciton state. Recombination of the biexciton occurs in two steps with an exciton as an intermediate state. Figure 1.4 shows the schema of the decay of a biexciton through exciton states into the empty dot, taking into account polarization of the emitted photons in dependence on confinement potential symmetry.

In case of non-zero FSS, the transition energy of one of the bright exciton states differs from that of another bright state and from both biexciton energies. After the emission of a photon at this particular energy, a QD can emit the photon

of the same energy again only after refilling in the same state. This way, a QD is ideal as a single photon source [Kim99]. Moreover, the recombination cascade $XX \rightarrow X \rightarrow$ *empty dot* can be also used to generate of polarization-entangled photon pairs [Ben00], when the FSS is zero. Both these cases can be implemented in quantum cryptography applications [Gis02], making the FSS a key issue in single QD spectroscopy.

The experimental values of FSS in In(Ga)As QDs grown on GaAs(001) substrates are found to range from -80 μeV up to 520 μeV [Bay02b, Hög04, Lan04, Kow05, Seg05]. Various techniques are applied to tune the FSS in order to use the QD as entangled-photon pair source by means of post-growth annealing [Seg05, You05], stress [Sei06, Plu11] or electric fields [Hög04, Kow05, Vog07]. Another approach for generating entangled photons is growing QDs on (111) substrates to achieve the symmetry of the confinement potential at least C_{3v} resulting in zero FSS [Sch08a, Sch09b, Sin09, Bim09]. Successful attempts were reported for droplet-epitaxy grown In(Ga)As/GaAs(111) in [Sto10] as well as for QDs grown on pyramidal shaped recesses in [Moh10a].

Recent investigations on single GaN/AlN QDs reported the excitonic FSS up to 7 meV [Kin10a]. There are still many ambiguities, e.g. no transitions $XX \rightarrow X$ were found in the luminescence spectra. It should be possible, however, to use the opportunity of nitride-based QDs as single-photon sources as well [Win08]. The mixing of valance band states leads to polarized excitonic emission. These transitions involve ground and first excited states, resulting in perpendicular-polarized lines with a large energetic distance (~10 meV). This large separation assures stable single-photons emission up to elevated temperatures. Indeed, in arsenide-based QDs the FSS becomes smaller than the homogeneous linewidth with increasing temperature, inhibiting a spectral separation of the co-polarized line pair.

1.1.4 Nitride-based quantum dots

The hexagonal wurtzite structure is the thermodynamically stable phase for III–V nitride-based semiconductors GaN, AlN and InGaN. This crystal structure is non-centrosymmetric, and the lack of inversion symmetry can result in spontaneous polarization for these polar materials. Such nitride-based QDs possess properties essentially different from the zinc-blende materials. For a description of the crystal structure of group III-nitrides a four-index system is used. The last index relates to the polar crystal direction (it is also called *c*-axis) and the first three describe the directions in the basal plane.

In a wurtzite crystal the cations and anions shift so that a dipole moment is induced in the unit cell, leading to spontaneous polarization. This effect, called pyroelectricity, is illustrated in figure 1.5. For AlN and GaN the spontaneous polarization values along the *c*-axes are $0.081\,{}^{C}/_{m^2}$ and $0.029\,{}^{C}/_{m^2}$ respectively. In the grown

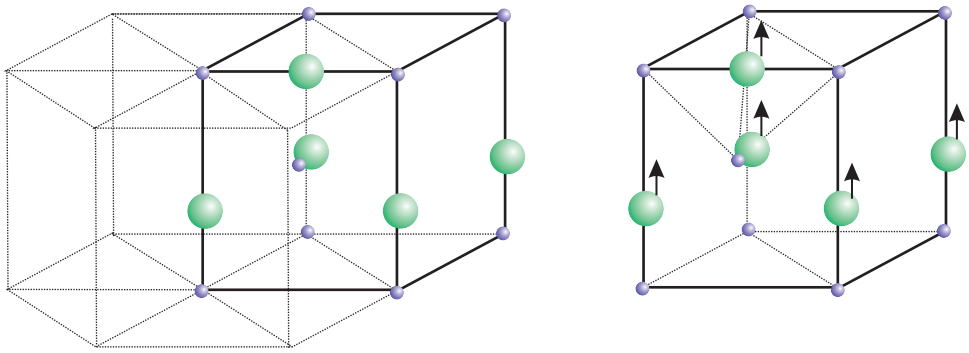

Figure 1.5: Left: The ideal wurtzite crystal, when the cation-anion sublattices are not shifted. Right: The shift of the atoms create a net polarization. (Figures adopted from [Sin03]).

heterostructures the intrinsic lattice parameters of the constituents differ. The resulting deviation of the bond length from the ideal structure in conjunction with strain existing in the heterostructure leads to additional net polarization - the so-called piezoelectric effect.

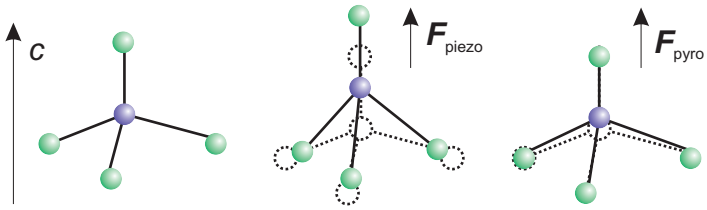

Figure 1.6: Illustration of the piezo- and pyroelectrical polarization in a wurtzite structure.

Both effects are depicted in figure 1.6. The ideal tetrahedron in the unit cell (e.g. GaN-bond) is shown in the left panel. If a biaxial strain is applied in the basal plane, the bonds of the ions here are reduced and an electric field in the c-direction $\boldsymbol{F}_{piezo}$ is induced: the piezoelectric effect (see middle panel). Even without external stress the bonds can deviate from the ideal tetrahedron, the center of mass of the ions is shifted and a residual dipole moment exists in the unit cell, inducing electric field $\boldsymbol{F}_{pyro}$ (see right panel) [And01, Fon03].

For a heterostructure consisting of materials with different net polarization a charge plane is created on the interface between the materials. This is schematically shown in figure 1.7. The polar charge results in a built-in electric field:

$$F_A = \frac{\sigma}{2\varepsilon_0\varepsilon_A}, \text{ and } F_B = \frac{\sigma}{2\varepsilon_0\varepsilon_B}$$

here F_A and F_B are the fields in the materials A and B respectively, $\sigma = P_A - P_B$ is the interface charge density.

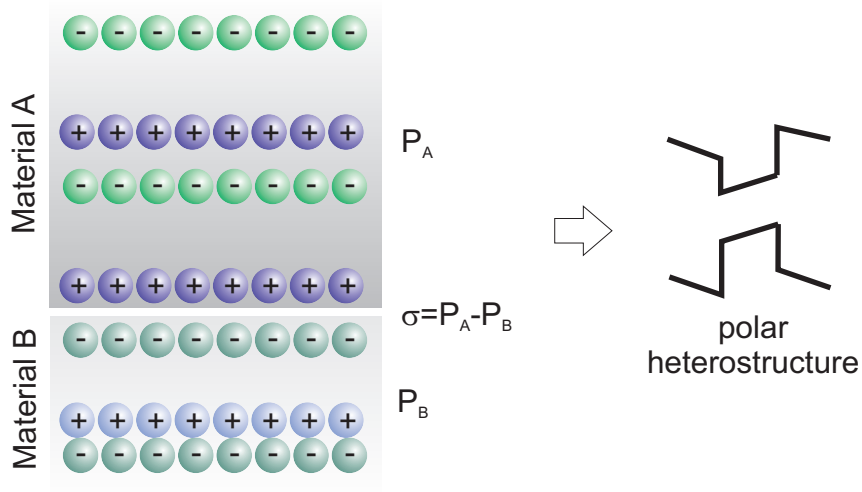

Figure 1.7: Left: Interface charge produced in the heterostructure. Right: Resulting band profile in the polar heterostructure.

The built-in fields are in the order of several MV/cm. This was shown in numerous theoretical works [Ber97, And00, And01, Ran03, Win06, Win08] and confirmed experimentally [Tak98, Wid98, Dau98, Sim03, Bre06]. The built-in field modifies the band structure of the material. The valance and conduction bands in a polar heterostructure in the absence of any external field is illustrated in the right panel of figure 1.7.

The polarization effects play a crucial role for the QD properties. Built-in fields result in spatial separation and reduced overlap of the electron and hole wave-function.

There is a wide range of applications for the group-III nitride heterostructures: violet laser diodes in Blu-ray disc players, white light emitting diodes, single-QD based devices for quantum information processing. In particular, the nitride-based QDs are promising candidates for development of such devices at elevated temperatures. Single-photon emission from single GaN/AlN QDs at 200K was reported already in 2006 in [Kak06]. Long spin relaxation times, relevant for spin-based information processing, were predicted for GaN/AlN QDs in [Kri03] and proved experimentally [Lag08].

1.2 Interaction of excitons in quantum dots and lattice vibrations

The vibrations of the atoms in a crystal are one of the most important scattering mechanisms for charge carriers. These vibrations increase with rising temperature. Some basic concepts of lattice vibration in the bulk material are described first.

The motion of the atoms can be described with a picture of oscillating particles attached to a spring: When an atom shifts from its equilibrium position, it experiences the restoring force arising from the interaction with the neighboring atoms. This physical problem can be easily solved for the simplest case: a crystal lattice consisting of two atoms in the basis with masses M_1 and M_2.The eigenvalues of their vibration around their equilibrium point at small values of the wave vector $\mathbf{k}$ are

$$\omega^2 \backsim (\frac{1}{M_1} + \frac{1}{M_2}), \text{ and } \omega^2 \backsim (\frac{1}{M_1} + \frac{1}{M_2}) \cdot k^2 \tag{1.3}$$

These two solution are the so-called optical and acoustical branches of dependence $\omega(\mathbf{k})$ respectively. For each type there is one longitudinal mode (atoms oscillate in the direction parallel to $\mathbf{k}$), and two transverse ones (atoms oscillate in one of the directions, perpendicular to $\mathbf{k}$). The acoustical branch represents the vibrations of both atoms in the same direction and is similar to the propagation of sound. The optical branch represents the oscillation of the atoms against each other with the center of mass in constant position. Here a time dependent electric dipole can be induced, and the vibrations can couple to an electromagnetic field.

In terms of quantum mechanics this is the problem of the quantum oscillator. The vibrations are quantized and a new particle is introduced, called a phonon. For each state of the quantum oscillator there is a finite number of phonons in this mode. Phonons are bosons and can share the same quantum state with an energy $\hbar\omega$, the phonon number is then

$$n_\omega = \frac{1}{\exp \frac{\hbar\omega}{\kappa_B T} - 1}$$

Here κ_B is a Boltzmann constant. Relation (1.3) shows that the optical phonon branch has a finite ω at $k = 0$ in contrast to the acoustic phonon branch, where ω goes to zero with decreasing k. Hence for low temperatures the occupancy of optical phonon branch is very small $n_\omega \approx 0$ and only becomes significant at higher temperatures. Acoustic phonons exist already at small T.

For a description of the electron-phonon interaction, the adiabatic approximation, also called Born–Oppenheimer, is used. As electrons have much smaller masses compared to atoms, they are supposed to follow the movements of the atoms. The atoms in contrast do not experience any change of the potential due to the electron motion. The variation of the overall Hamiltonian is considered to be so slow that the problem can be regarded as stationary at each moment.

The system is then described with the Hamiltonian

$$H = H_{atom} + H_{elec} + H_{e-lattice}$$

H_{atom} is the Hamiltonian of the atoms in the background “adiabatic” potential, which changes very slowly. The phonon eigenvalues and eigensolution can be obtained from this operator. H_{elec} represents the electron motion if the atoms would

stay in their equilibrium position. $H_{e-lattice}$ describes the interaction between the electrons and phonons, i.e. this part is influenced by the shifts of the atoms relative to their equilibrium positions.

In theory the $H_{e-lattice}$ is divided into different parts, or in other words different electron-phonon interaction mechanisms. The displacement of the atoms represents a deformation in the crystal and therefore changes the electronic energies. This change is related to the deformation potentials of the crystal. The corresponding interaction mechanism and the respective part of the Hamiltonian are called deformation-potential electron-phonon coupling. This type of electron-phonon coupling is different for optical and acoustic phonons. The acoustic phonons represent the "macroscopic" distortion of the lattice, and the optical ones the "microscopic" one. Optical phonons change the bond length or angles between the bonds within a primitive unit cell.

In polar materials a change of the atom positions leads to a macroscopic polarization. The induced electric field is proportional to the strain (as long as the deformations are small enough), which is known as piezoelectric effect. The polar interaction of electrons with the polarization field, related to acoustic phonons, is called piezoelectric coupling. In case of optical phonons only longitudinal vibrations induce an electric dipole. The transverse optical mode of the atomic motion is indeed similar to the movement of the capacitor plates parallel to each other, which does not influence the energy of the electrons. The polar interaction of the electrons and longitudinal optical phonons is called Fröhlich coupling.

Generally speaking, lattice dynamics within a QD is different in comparison to the bulk. Confined optical phonon modes and interface phonons appear in the heterostructure. When the embedded and host materials have an almost identical lattice structure, interaction of the phonons and excitons can still be treated as in bulk. The same interaction mechanisms prevail. However, the coupling strengths of different mechanisms are different in QDs. The significant changes occur due to localization of the charge carriers. A stronger coupling to short-wavelength phonons occurs due to the discrete energy level of the dot [SR87]. Special attention should be paid to the strain distribution and spatial confinement of the wave-functions of the charge carriers.

Coupling of the phonon and excitons confined in the dot can be clearly observed in the luminescence experiments. The δ-like emission line of exciton decay (i.e. a photon emitted at recombination of the electron and the hole), called zero-phonon line, is surrounded by acoustic-phonon side-bands: e.g. [Bes01]. These side-bands result from emission and absorption of the acoustic phonons. Coupling to longitudinal optical phonons produces to so-called replicas in the spectra: an intense emission spaced by one optical phonon energy relative to the zero-phonon line: e.g. [Hei96, Hei99].

Exciton-phonon interaction is vital for study of QD properties. Timescales, during which the coherence of the excitonic state is preserved, are limited by the lattice

vibrations. The phonons can also be involved into dark-bright state transitions. The energies of the states with different spins differ (see figure 1.4). If a spin-flip process occurs, a phonon is necessary for the energy conservation. These phonon-mediated spin-flip processes arise from scattering with the nuclear spin of an atom [Erl02, Mer02, Sem03, Bra05] or spin-orbit coupling [Kha00, Kha02, Woo02, Gol04]. These processes can be crucial for applications of the QDs, mentioned in the previous section.

1.3 Quantum dot in an electric field

1.3.1 Quantum confined Stark effect

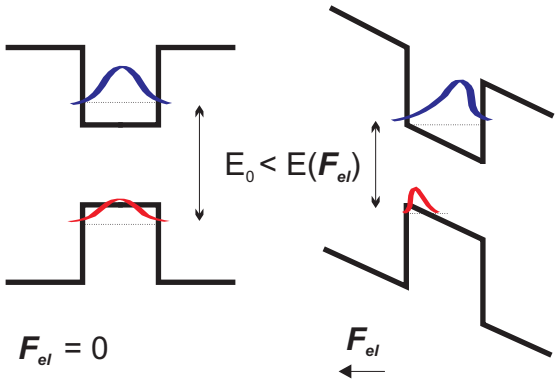

Figure 1.8: The band structure of a QD with and without electric field. Red and blue curve represents the distribution of the wave-function of the hole and electron respectively.

An electric field influences the properties of the QD. This fact is usually referred to as quantum confined Stark effect (QCSE) [Mil85, Mil86, Fry00]. When an external electric field is applied to a heterostructure, the following effects must be considered:

(i) The band structure changes (see figure 1.8). The electric field pushes the charge carriers in opposite directions. This lowers the electron and raises the hole energy level. Overall, a red shift in the energy of the excitonic transition is observed.

(ii) The overlap of the wave-functions and the oscillator strength of the excitonic transition is reduced. This decreases the intensity of the excitonic transition and increases the exciton lifetime.

(iii) Coulomb interaction between the charge carriers decreases with reduction of the overlap of the electron and hole wave-functions, resulting in altering the binding energies of the multiexcitonic complexes in the QD: see equation (1.2).

(iv) The spatial separation of the electron and hole can create an electric dipole. The dipole influences the interaction of the exciton with all external electric fields and makes the exciton sensitive to the fluctuations of the external electric field.

The change of the energy of the exciton in the electric field is described as follows: An electron and a hole, spatially separated at a distance $\boldsymbol{l}$, constitute an electric dipole $\boldsymbol{\mu_0} = e\boldsymbol{l}$. This dipole interacts with the external electric field $\boldsymbol{F}$ and its energy: $\boldsymbol{\mu_0} \cdot \boldsymbol{F}$. However, the electric field influences the charges of the dipole and can induce an additional dipole $\boldsymbol{\mu_{ind}} = \alpha \boldsymbol{F}$, where $\alpha = \frac{d\boldsymbol{\mu_0}}{d\boldsymbol{F}}$ is the polarizability. The energy of the dipole is then

$$E(F) = \boldsymbol{\mu_0} \cdot \boldsymbol{F} + \boldsymbol{\mu_{ind}} \cdot \boldsymbol{F} = \boldsymbol{\mu_0} \cdot \boldsymbol{F} + \alpha \boldsymbol{F}^2 \tag{1.4}$$

Depending on the value of polarizability and the intrinsic electric dipole moment one of the terms in equation (1.4) can be dominating, resulting in either a linear (e.g. [Nak06a]) or quadratic (e.g. [Rob05, Nak06b]) QCSE. An intrinsic dipole moment, i.e. the separation of the center of masses of charge carrier wave-functions when an external field is zero, was predicted for pyramidal QDs [Gru95, Sti99]. It can stem e.g. from a composition gradient in the growth direction [Fry00]. The external electric field can have different origins: externally applied to a heterostructure, permanent built-in fields, dynamically changing electric fields induced in the close vicinity of the QD. The last two cases are described in detail below.

1.3.2 Spectral diffusion

Defects, a crystal surface or even neighbor QDs can lie in close neighborhood to a QD and act as charge traps. The process of charge capture and release is stochastic and can occur on different timescales. At every moment a charge (which can be positive or negative, e.g. captured by a donor or acceptor) near a QD then would create a static electric field, influencing the transition energy of the exciton, confined in the QD: see equation (1.4). Constant charge trapping and release results in a random change of the QD emission energy. This exciton energy change, induced by fluctuating electric fields in the QD environment, is called spectral diffusion (SD).

If the change of the local electric field happens faster than the lowest measurement time for a luminescence spectrum, then the line appears broadened. While some defects can trap or release the charge for a period of time in the range of hundreds of milliseconds or seconds, in luminescence experiments it is observed as a continuous change or discrete shift of the spectral position of the emission line [Rob00, Bes02, Rod05, Bar06, Rol07]. This phenomenon is also attributed to SD and is often called spectral jitter.

The SD, which can be resolved in the luminescence experiments as (dis)continuous spectral shifts of the excitonic emission line, is sometimes referred to as long-

timescale SD. In contrast, the inhomogeneous line broadening resulting from interaction of the exciton and fluctuating electric fields in the environment is called short-timescale SD. To distinguish between the jitter, which can be resolved with the measurement set-up, and the jitter, which cannot be resolved, the term long- or short-timescale SD is used here. This is, however, an arbitrary decision, because it depends on the properties of the measurement system.

The term SD was first introduced for the colloidal QD in [Emp96] and then applied to self-assembled QDs. Sometimes it is also used to describe the intensity fluctuation or quenching observed in various QD material systems. Strictly speaking, this phenomenon is not necessarily a result of the interaction between an exciton and an electric field. If for instance the energy of electron-hole recombination is transferred to the remaining charge carriers in the dot, then ejecting them out of the dot, the emission line is "off". Such Auger-mechanism was proposed to explain the luminescence intermittence in colloidal QDs [Emp96, Nir96, Neu00]. To simplify matters, in the present work the spectral shift of the transition line (long- or short-timescale) and the variation of the emission intensity are both called SD.

1.3.3 Nitride-based quantum dots and electric fields

In a heterostructure the electric fields can be permanently present: these fields result from piezo- or pyroelectric effects or interface charge-planes. A good example are the III-nitride heterostructures briefly described above in section 1.1.4. As a consequence of the large built-in electric field the QCSE, often called giant in case of nitride-based materials, can red-shift the excitonic transition. Emission energies of the GaN/AlN QDs well below the band gap of GaN were indeed often reported [Dam99, Bre03, Bre06].

Let some electric field $\boldsymbol{F_{int}}$ be constantly applied to the QD with a dipole moment $\boldsymbol{\mu_0}$. Assuming, this electric field does not change the intrinsic dipole moment $\boldsymbol{\mu_0}$ and polarizability α of the confined charge carriers, the additional local field $\triangle\boldsymbol{F}$ then changes the exciton transition energy E relative to the exciton energy without local field is

$$\begin{aligned}\Delta E(\triangle\boldsymbol{F}) &= E(\boldsymbol{F_{int}}+\triangle\boldsymbol{F}) - E(\boldsymbol{F_{int}}) = \\ &\boldsymbol{\mu_0}\cdot\triangle\boldsymbol{F} + 2\alpha\boldsymbol{F_{int}}\cdot\triangle\boldsymbol{F} + \alpha\left(\triangle\boldsymbol{F}\right)^2 = \\ &\left(\mu_0\cos(\boldsymbol{\mu_0},\triangle\boldsymbol{F}) + 2\alpha F_{int}\cos(\boldsymbol{F_{int}},\triangle\boldsymbol{F})\right)\triangle F + \alpha\left(\triangle\boldsymbol{F}\right)^2 \end{aligned} \tag{1.5}$$

or similar to equation (1.4):

$$\Delta E(\triangle\boldsymbol{F}) = \boldsymbol{\mu_{built-in}}\cdot\triangle\boldsymbol{F} + \alpha\left(\triangle\boldsymbol{F}\right)^2 \tag{1.6}$$

here an effective dipole moment $\boldsymbol{\mu_{built-in}} = \boldsymbol{\mu_0} + 2\alpha\boldsymbol{F_{int}}$ is introduced. This electric dipole moment $\boldsymbol{\mu_{built-in}}$ is called built-in or permanent dipole moment of the QD

and results from separation of the charge carriers in the electric field $\boldsymbol{F_{int}}$. In nitride QDs $\boldsymbol{F_{int}}$ is in the order of 4-10MV/cm and approximately $\boldsymbol{\mu_{built-in}} \parallel \boldsymbol{F_{int}}$.

For $\triangle \boldsymbol{F} \perp \boldsymbol{F_{int}}$ the QCSE appears as a pure quadratic

$$\Delta E(\triangle \boldsymbol{F}) = \alpha \left(\triangle \boldsymbol{F}\right)^2$$

For small variations of local field $\triangle F \ll F_{int}$ with a non-zero component in the growth direction can be approximated as linear

$$\Delta E(\triangle \boldsymbol{F}) = \boldsymbol{\mu_{built-in}} \cdot \triangle \boldsymbol{F}$$

Multiexcitonic complexes

According to equation (1.2) the energy of a multiexcitonic complex, consisting of n electrons and p holes, is

$$H_{n,p} = H_{ne} + H_{ph} + H_{ne,ph,Coul} \tag{1.7}$$

here H_{ne} and H_{ph} - the energies of the single particles and $H_{ne,ph,Coul}$ - terms, describing the Coulomb interaction among all the particles. If one of the electron-hole pairs recombines, a photon is emitted and $(n-1)$ electrons together with $(p-1)$ holes remain in the dot. Then the energy of the photon, the so-called emission or transition energy of the multiexcitonic complex $E^{n,p}$, detected in the luminescence experiments, is

$$E^{n,p} = H_{n,p} - H_{n-1,p-1} = H_{e*} + H_{h*} + H_{e*,p*,Coul}$$

here H_{e*} and H_{h*} - the energies of the electron and hole which recombined, and $H_{e*,h*,Coul}$ - terms describing the Coulomb interaction of the recombining electron-hole pair with the remaining charge carriers and their own attractive Coulomb interaction.

When the fluctuation of the local electric field $\triangle \boldsymbol{F}$ is small enough and does not change the distribution of the charge carriers in the QD, the energy $H_{n,p}$ changes in electric field $\triangle \boldsymbol{F}$ as

$$H_{n,p}(\triangle \boldsymbol{F}) = H_{ne} + H_{ph} + H_{ne,ph,Coul} + \boldsymbol{D^{n,p}_{built-in}} \cdot \triangle \boldsymbol{F}$$

here H_{ne} and H_{ph} - the same energies of the single particles and $H_{ne,ph,Coul}$ - the same terms describing the Coulomb interaction of all the particles without electric field $\triangle \boldsymbol{F}$ as in equation (1.7). $\boldsymbol{D^{n,p}_{built-in}}$ is the electrostatic dipole moment of the charge distribution in a QD, filled with n electrons and p holes.

When an electric field is applied to the dot, transition energy $E^{n,p}$ changes according to the formula (1.6), then neglecting the quadratic term of QCSE:

$$\Delta E^{n,p}(\Delta F) = E^{n,p}(\triangle \boldsymbol{F}) - E^{n,p}$$

$$\approx \left(\boldsymbol{D}^{n,p}_{built-in} - \boldsymbol{D}^{n-1,p-1}_{built-in}\right) \cdot \triangle \boldsymbol{F} = \boldsymbol{\mu}^{n,p}_{built-in} \cdot \triangle \boldsymbol{F} \tag{1.8}$$

Here the effective dipole moment of the multiexcitonic complex $\boldsymbol{\mu}^{n,p}_{built-in} = \boldsymbol{D}^{n,p}_{built-in} - \boldsymbol{D}^{n-1,p-1}_{built-in}$ is introduced in analogy with QCSE.

1.4 Homogeneous line broadening

An exciton is a quantum-mechanical state and is defined by its phase and energy. According to the Heisenberg uncertainty principle, the energy of the exciton is only determined up to a small value $\triangle E$:

$$\triangle E \leq = \frac{2\hbar}{\tau_2}$$

where τ_2 is the so-called dephasing time. The uncertainty in energy results in the homogeneous broadening of the linewidth of the excitonic transition or, in other words, lifetime broadening

$$\Gamma_{hom} = \frac{2\hbar}{\tau_2}$$

The exciton lifetime τ_2 takes into account the following processes:

(i) processes, which only change the quantum mechanical phase of the excitonic state. For example, scattering with free charge carriers, excitons, elastic phonon scattering.

(ii) processes, which change the energy of the excitonic state and thus the phase. These processes are distinguished between radiative (with emission of a photon) and non-radiative. These processes include phonon emission, non-elastic scattering with the phonons, excitation into a higher energy state and are determined with time constant τ_1 is energy lifetime.

When only processes (ii) occur, then $\tau_2 = 2\tau_1$. The factor 2 arises from the relation between induced polarization $\boldsymbol{P} = \boldsymbol{P_0} \exp\left({}^{-t}/_{\tau_2}\right)$ and population decay $N = N_0 \exp\left({}^{-t}/_{\tau_1}\right)$; $N \sim \boldsymbol{P}^2$. The processes (i) decrease τ_2 and generally the following expression is valid [DB68]:

$$\frac{1}{\tau_2} = \frac{1}{2\tau_1} + \frac{1}{\tau_p}$$

here τ_p determines the pure phase-relaxation under energy conservation.

The dephasing time τ_2 can be defined directly by four-wave mixing experiments. For arsenide-based QDs it was found to be in the range of hundreds picoseconds

[Bor01, Bir01], resulting in a homogeneous width of the excitonic transition in the range of few µeV. No such experiments are reported for nitride-based QDs.

The radiative lifetime measured for InGaN/GaN QDs is in the order of a few nanoseconds [Bar04], for GaN/AlN QDs it ranges from nanoseconds up to milliseconds [Sim03, Kak03, Bre06]. Thus a simple estimation for the homogeneous linewidth can be made, when neglecting τ_p:

$$\Gamma_{hom} = \frac{2\hbar}{\tau_2} \approx \frac{\hbar}{\tau_1} \leq \frac{\hbar}{1\,\mathrm{ns}} = \frac{4.13\,10^{-15}\,\mathrm{eV}\cdot\mathrm{s}}{10^{-9}\,\mathrm{s}} = 4\,\mu\mathrm{eV} \tag{1.9}$$

Inhomogeneous broadening arises from the shifts of the excitonic emission energy due to fluctuation of the electric field in the environment (SD - see section 1.3.2). These processes take place on a much longer timescale [Pal03, Sal10a].

With rising temperatures the contribution of the phonon-induced processes to the homogeneous linewidth increases. The homogeneous linewidth of excitonic transition in a bulk semiconductor can be described as

$$\Gamma_{hom}(T) = \Gamma_0 + \Gamma_{ac} + \Gamma_{opt} = \Gamma_0 + \sum_{\boldsymbol{q},\kappa} C(\hbar\omega_{\boldsymbol{q},\kappa}) S(\hbar\omega_{\boldsymbol{q},\kappa}, T)$$

Γ_0 gives the homogeneous line broadening part, and the summation term arises from all possible phonon-scattering channels. Here $C(\hbar\omega_{\boldsymbol{q},\kappa})$ - is the coupling element to the phonons (including mechanism of exciton-phonon interaction) and $S(\hbar\omega_{\boldsymbol{q},\kappa}, T)$ - the spectral density of the phonons with a phonons number κ, wave vector $\boldsymbol{q}$ and energy $\hbar\omega_{\boldsymbol{q},\kappa}$. The phonon number κ corresponds to transverse-acoustic (TA), or longitudinal optical (LO), or longitudinal acoustic (LA) phonons.

When taking into account the interaction mechanisms and phonon population occupation in dependence on temperature [Rud90]:

$$\Gamma_{hom}(T) = \Gamma_0 + \gamma_{ac} T + \gamma_{LO} N_{LO}(T) \tag{1.10}$$

γ_{ac} and γ_{LO} denote the so-called coupling parameters to acoustic and optical phonons respectively, and $N_{LO}(T)$ is the Bose-Einstein occupation function of optical phonons of average energy $\overline{\hbar\omega}$:

$$N_{LO}(T) = \frac{1}{\exp(\frac{\overline{\hbar\omega}}{kT}) - 1}$$

This formula is generally also applicable to QDs [Bay02a].

With account for inhomogeneous broadening and measuring system the homogeneous linewidth is described with

$$\Gamma^2(T) = \Gamma^2_{app} + \Gamma^2_{inhom}(T) + \left(\Gamma_0 + \gamma_{ac} T + \gamma_{LO} N_{LO}(T)\right)^2 \tag{1.11}$$

Here Γ^2_{app} is the broadening resulted from the experimental set-up, and Γ^2_{inhom} - the inhomogeneous broadening (e.g. induced by SD). The third term includes the zero-temperature linewidth Γ_0 and the line broadening by means of elastic scattering, with the phonons: $\gamma_{ac}T$ - for acoustic phonon scattering and $\gamma_{LO}N_{LO}(T)$ - for optical phonon scattering. $N_{LO}(T)$ is the occupation function of optical phonons.

Experimental

2 Experimental set-up, numerical methods, samples

This chapter presents an overview of the experimental and theoretical methods used in the work. The main advantages of cathodoluminescence spectroscopy and a technical description of the set-up are outlined in section 2.1. The methods of probing single quantum dots (QDs) are summarily described in section 2.2. Section 2.3 is dedicated to the numerical methods applied to calculate strain distribution in heterostructures, wave-functions of the charge carriers and exciton-acoustic phonon coupling in nitride-based. Section 2.4 concludes the chapter with the description of the investigated nitride-based QD samples. Details on the growth of site-controlled arsenide QDs are outlined in chapter 5 after introducing the concept of strain-mediated growth. The table on page 160 contains a brief overview of the main details with the names of the samples originally given by the institutes, where the samples were grown.

2.1 Cathodoluminescence spectroscopy

It takes a special effort to address an individual QD and investigate its optical properties. A commonly used technique is micro-photoluminescence spectroscopy (µPL). In µPL a photon of the excitation light, e.g. from a laser pulse, excites an electron into the conduction band, creating an electron-hole pair in the heterostructure. Depending on the energy of the excitation light this pair can be created either in the barrier material (non-resonant excitation), in the wetting layer, or directly in the QD (resonant excitation). The excitation light is focused through an optical microscope objective, and the luminescence is gathered with the same objective to the detector. Under the best alignment conditions, the excitation spot can be as low as 1-2 µm.

In this work cathodoluminescence (CL) spectroscopy was used. The electron beam of the scanning electron microscope (SEM) is used as excitation instead of light in µPL (figure 2.1). The high energy electrons of the SEM induce various processes in the solid state: secondary electrons, back-scattered electrons, generation of electron-hole pairs, thermal effects, characteristic X-rays, some Auger processes and so-called cathodoluminescence. Collection of the secondary electrons from the sample provides the SEM image of the sample surface. Depending on beam current

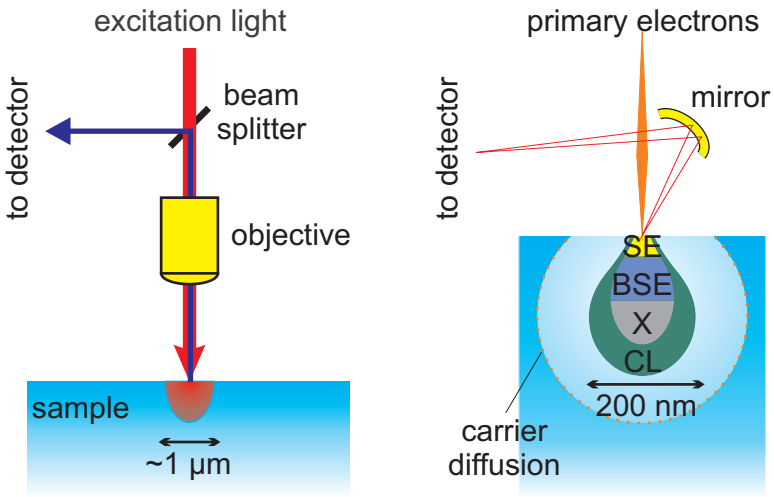

Figure 2.1: Schema of µPL (left) and CL (right) excitation in spectroscopic experiments. SE - secondary electrons, BSE - backscattered electrons, X - X-rays, CL - cathodoluminescence, dimensions of the excitation volume - 200 nm.

and electron acceleration voltage, the resolution in the nanometer range is possible for the SEM images.

Spatial resolution of the CL spectroscopy is defined by the size of the so-called excitation volume - part of the crystal, where electron-hole pairs are generated by primary electrons. Depending on the energy of the primary electron and the material properties of the crystal, one primary electron of an electron beam generates up to thousands of electron-hole pairs. These electron-hole pairs are relevant for the investigation of the QDs. When an electron-hole pair is captured in a heterostructure, a photon is emitted. This emission, called CL in the present work, can be coupled to a detector and then reveals spectroscopic information about the sample.

According to the review [Yac86] for materials with atomic numbers $Z < 40$ the excitation volume can be approximated as a sphere with diameter R_e. R_e denotes the average range of electron penetration. The empirical formula in [Kan72, Yac86] gives $R_e[\mu\text{m}]$ as a function of the electron-beam energy $E_b[\text{keV}]$

$$R_e = \frac{0.00276A}{\rho Z^{0.0889}} E_b^{1.67} \tag{2.1}$$

here $\rho[g/\text{cm}^3]$ is the molar density, $A[g/\text{mol}]$ and Z are the atomic weight and number. The spatial resolution is also restricted by the charge carrier diffusion in the crystal, which in turn depends on the crystal quality. Better spatial resolution can therefore be achieved for a sample with a high concentration of defects as compared to a high-quality crystal.

Figure 2.2 shows the excitation volume dimension in dependence on the electron beam energy for the three QD material systems investigated in the present work.

For calculation of the displayed curves see formula (2.1). The parameters are always taken for the matrix material, as the volume of the QD can be neglected in estimation of R_e. Spatial resolution as low as ~ 200 nm can be achieved for the electron acceleration voltages of 3 kV.

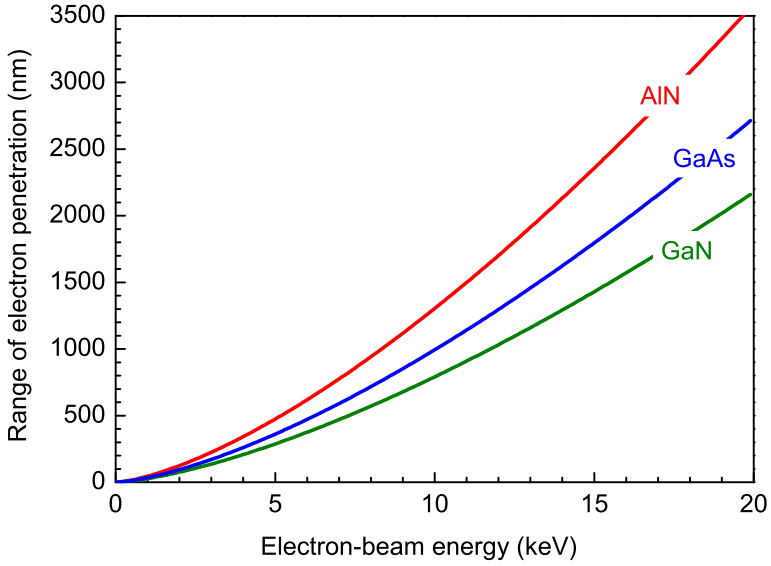

Figure 2.2: Dependence of the excitation volume dimension on the electron-beam energy, calculated for AlN, GaAs, GaN.

The excitation density in CL experiments can be influenced by various parameters: electron-beam current, electron-beam energy, and position of the electron beam. However, due to the complexity of the charge carriers diffusion only qualitative statements could be made about the increase/decrease of the excitation density, and it is not possible to calculate a value as straightforward as the one in µPL. Increase of the electron beam current leads to an increase of the excitation volume, and it is not clear, how the excitation of a low dimensional structure like a QD changes (see [Tür01]). At a larger acceleration voltage the same number of primary electrons penetrate into a larger excitation volume. However, the excitation density is not necessarily reduced, since every primary electron has a larger energy and can induce larger numbers of electron-hole pairs, relative to the lower acceleration voltage. To check the influence of excitation density qualitatively the method of changing the excitation density by scanning the beam across the sample surface was often used in this work.

Experimental set-up

The experimental set-up used in this work is schematically shown in figure 2.3[1]. The commercially available microscope SEM JEOL JSM 840 was modified. The in-

[1]Figure was kindly provided by Sven Rodt.

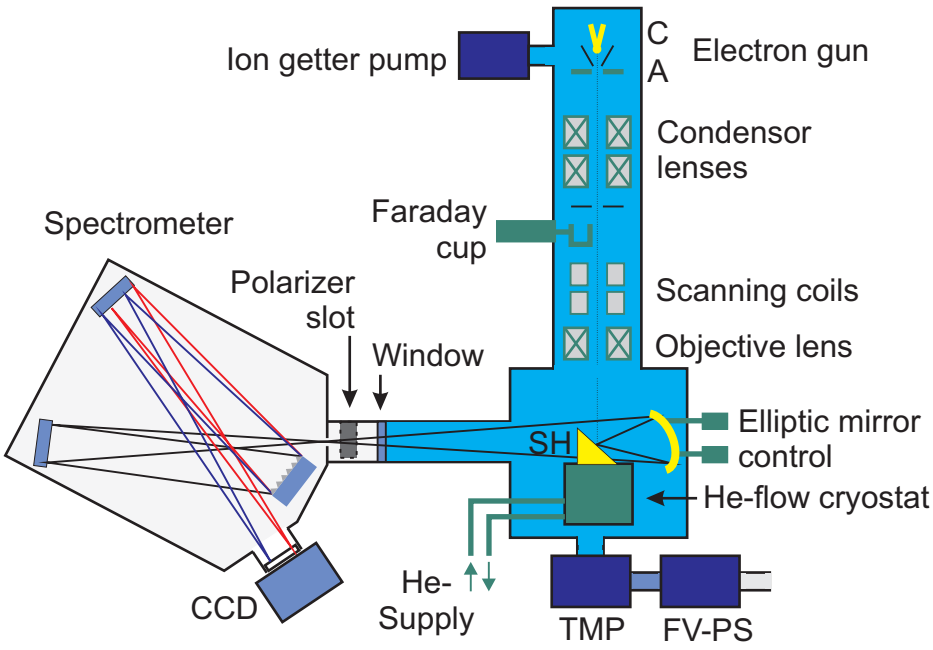

Figure 2.3: Schema of the CL set-up. TMP - turbo molecular pump, FV-PS - fore-vacuum pump stage, SH - sample holder, A - anode, C - cathode (for further descriptions see text).

stalled custom-made sample holder and elliptical mirror allow efficient luminescence collection (for more details see [Chr91]).

The electrons are emitted by a lanthanum hexaboride cathode and accelerated in the gun section. The acceleration voltage can be set from 2 kV up to 40 kV. Different sections of the lenses adjust focusing and control scanning of the electron beam on the sample surface. The retractable Faraday cup is used to measure the electron beam current, which can be varied from 20 nA down to pA. The He-flow cryostat provides measurement temperatures from room temperature (RT) down to 5 K.

Operation of the SEM is only possible in a high vacuum. The vacuum is provided by a pump system, consisting of a turbo molecular pump and a fore-vacuum pump stage, and a cryogenic trap. A pressure of the order of 10^{-7} mbar is achieved. To assure longer lifetime of the cathode, an ion getter pump is additionally installed close to the gun section.

An aluminum-coated mirror collects the luminescence from the sample. The sample holder and the entrance slit of the spectrometer are located in the two foci of the elliptic mirror. The luminescence from the sample is out-coupled through a quartz window into a 30-cm monochromator. The gratings with different numbers of lines and various blaze angles provide the following spectral resolution:

1.65 meV at 4.2 eV with the grating with 2400 lines/mm and entrance slit of 100 µm

0.5 meV at 4.2 eV with the grating with 2400 lines/mm and entrance slit of 30 µm

140 µeV in the spectral range of 1.20 eV-1.40 eV with the grating with 1200 lines/mm and entrance slit of 30 µm

Using line shape analysis and taking into account the signal-to-noise ratio of the analyzed peak, the energetic position of single lines could be determined within a better accuracy, than given by the set-up resolution [Tür01]. For example, in case of InGaAs the fine structure splitting of the excitonic bright states could be defined with the accuracy of 20-40 µeV with this set-up [Rod06, Seg06].

A linear polarizer can be placed into the slot in front of the entrance slit to perform the polarization-dependent measurements. As a detector, a silicon charge coupled device camera (CCD) of Princeton Instruments is used. It consists of 1340x100 pixels and is sensitive between the wavelength of 250 nm and 1050 nm (4.96 eV down to 1.18 eV detection energy). An efficient custom-made software, controlling both the SEM and CCD, allows different measuring procedures.

Measurement modes

While the electron beam is moved over the sample and the spectra are recorded, site-dependent information about the luminescence can be obtained simultaneously. The set-up is extended by the software, allowing to measure the CL spectra for each point of a rectangular area on the sample together with an SEM image of the surface. The resulting 4D arrays of data (I, E, x, y) represent the dependence of CL intensity I on detection energy E for a particular point on the sample (x, y). For analysis of the results, presented in chapter 5, the following two types of graphs can be extracted from these data arrays:

CLSI (cathodoluminescence spectra images) - 2D graphs, showing the spatial distribution of the CL intensity $I(x, y)$. Intensity is coded in color and can be taken for particular energy $I(E_0)$ or be calculated as integrated intensity over some energy range (E_1, E_2).

CLWI cathodoluminescence wavelength images - 2D graphs, showing spatial distribution of the wavelength of maximum CL intensity $E_m(x, y)$, where $I(E_m) = max\, I(E_1, E_2)$. Wavelength is coded in color, maximum intensity is found for some energy range (E_1, E_2). Although in this work always the spatial distribution of the emission energy of maximum CL intensity will be shown, by tradition they are called "CL wavelength images", not the "CL energy images".

Similar to automatized CLSIs the spectra can be recorded simultaneously by moving the electron beam over the sample (in the so-called spot mode of the SEM, when no raster occurs and the beam is focused onto a constant site on the sample). Such measurements can be performed moving the electron beam "by hand". In cases when no CLSIs can be measured (e.g. due to a long time necessary for the measurement) still some qualitative information can be obtained since changing the position of the

electron beam relative to a QD under investigation influences the local excitation density.

The series of CL spectra can be recorded directly one after another. The data show the evolution of the spectrum and are important for evaluating the spectral diffusion (SD) effects. Such spectra are called SD-patterns and are described in chapter 3.

Advantages of cathodoluminescence spectroscopy

CL spectroscopy has special advantages due to high spatial resolution. For nitride-based QDs there are additional aspects in favor of this spectroscopy method. First, it permits high excitation energies: wide bandgap materials can be investigated. The electron-hole pairs are excited in the matrix material and then relax into the QD structure, providing non-resonant excitation. Second, no collecting or focusing lenses are used in the CL set-up (they are necessary for µPL - see figure 2.1). The lenses can introduce additional polarization into the transmitted beam, thus influencing either exciting light or collected luminescence, which can in turn complicate the investigations. The ultraviolet spectral range is critical due to high absorption of the optical elements (lenses, objectives), which in addition are very expensive. The only optical elements used in the set-up - the elliptical mirror with aluminum coating and the quartz window - do not change any of the properties of the collected light. This was carefully checked for a wide range of detection energies.

2.2 Probing a single quantum dot

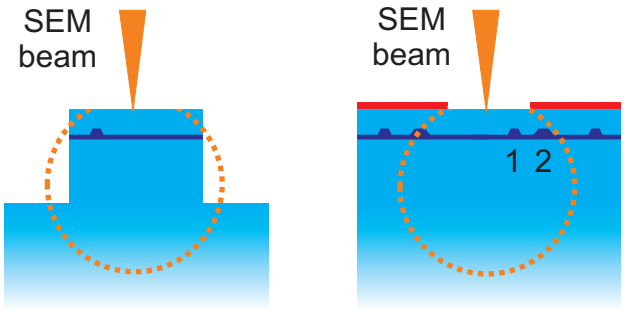

Figure 2.4: Probing single QDs. Left: Mesa structure. Right: Metal shadow mask.

The major aim of this work is to investigate the luminescence properties of single QDs. This is a difficult task, because of the large areal density of self-assembled QDs all optical spectroscopy methods using either optical far-field excitation (PL, µPL) or electron beam excitation (CL) will excite a large number of QDs simultaneously. Two basic approaches allow investigation of the single QD: either reducing the number of the excited dots or reducing the number of the dots, from which luminescence

is detected. The first approach is achieved by post-growth etching mesa structures with a small diameter. The second approach is realized by applying a metal masks with small apertures. The metal mask then absorbs all the light emitted by the QDs underneath.

This is illustrated in figure 2.4. The circle represents the excitation volume of CL. For the mesa structure only one dot is located in the mesa. By using the metal mask only luminescence of the QD1 can be detected, while all the luminescence of QD2 is absorbed by the mask.

Both methods, shadow mask and mesa structures, were applied for nitride-based QD samples, investigated in the present work. Lowering the density of the QDs during growth is undoubtedly an alternative to the post-processing of the samples. This method, however, requires accurate control of the growth parameters. Site-controlled QD growth with pre-definition of the QD nucleation site permits growth of dots with very low density. These aspects are discussed in chapter 5.

2.3 Numerical modeling

2.3.1 Strain distribution

The strain is calculated within the framework of the continuum elasticity model. Its advantages in comparison to the competing models are discussed in detail in [Sti99]. For each point of a given structure the displacement vector field $\boldsymbol{u} = \boldsymbol{r} - \boldsymbol{r'}$ is calculated. Here $\boldsymbol{r}$ and $\boldsymbol{r'}$ describe the position of a certain point in the crystal before and after deformation. The strain components are obtained as follows:

$$\varepsilon_{ij} = \frac{\partial u_i}{\partial x_j}$$

The Hook's law for the stress components is $\sigma_{ij} = \sum_{k,l} C_{ijkl}\varepsilon_{kl}$. Here C_{ijkl} is the compliance tensor, its components can be expressed by the material parameters C_{11}, C_{12}, C_{13}, C_{33} and C_{44}.

Subsequently the total strain energy is calculated:

$$U_{cm} = \frac{1}{2}\sum_{i,j,k,l} C_{ijkl}\varepsilon_{ij}\varepsilon_{kl}$$

U_{cm} is minimized for a given structure, using finite differences for the strains ε_{ij}.

The calculations of strain distribution for the structures with a buried stressor, presented in chapter 5, were performed by Andrei Schliwa.

2.3.2 Wave-function

For an adequate description of the confined charge carriers, the wave-functions are calculated by means of 8-band $\boldsymbol{k} \cdot \boldsymbol{p}$ theory and followed by either Hartree or Hartree-Fock approximation. This method can be implemented for arbitrarily shaped QDs. It includes the effects of strain (as described in the previous section), piezoelectricity and pyroelectricity, spin-orbit and crystal-field splitting, valence-band mixing, and conduction band-valence band interaction. The material parameters for InGaN/GaN QDs are listed in [Win06]. The material parameters for GaN/AlN QDs from [Vur03, Rin08] were included as described in [Win08].

The numerical method is schematically shown in figure 2.5. First, strain and pyroelectric potentials are calculated for a realistic 3D model of a QD of particular geometry and composition. The piezoelectric potentials are calculated correspondingly. The single-particle states are obtained for the potentials within the formalism of 8-band $\mathbf{k} \cdot \mathbf{p}$ theory.

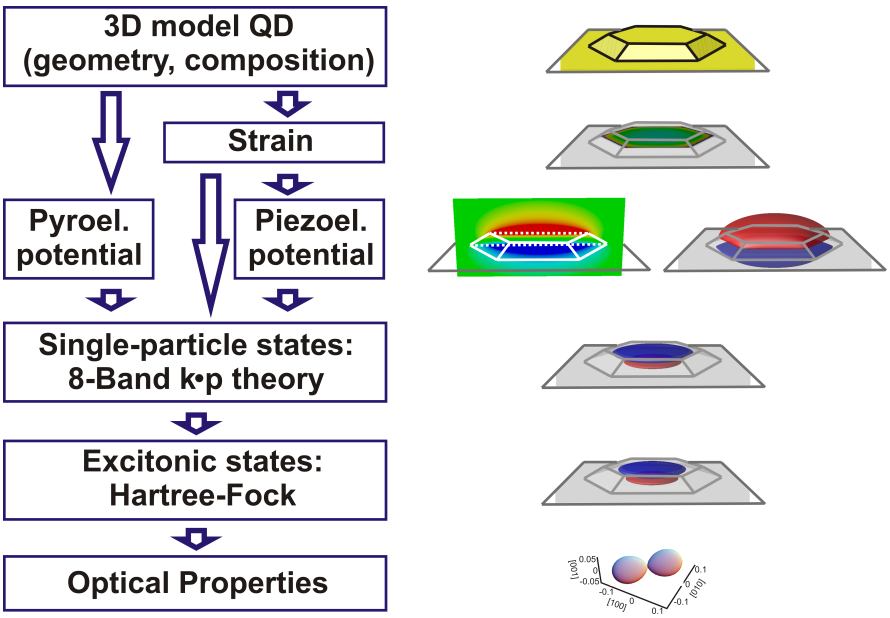

Figure 2.5: Schema of the calculation method for wave functions of the excitonic states of the charge carriers, confined in a QD. (Figure adopted from [Rod06]).

The few-particle effects have to be considered to obtain realistic excitonic states from single-particle states. For the electrons and holes, confined in the dot these are: Coulomb and exchange interaction as well as correlation effects. The configuration interaction scheme [McW69] was successfully applied to InAs/GaAs QDs [Bra00, Sti01, Wil01]. For the nitride-based materials it was extended by the self-consistent Hartree method [Win06]. This approach is applied in this work to model optical properties of the InGaN QDs.

Within the Hartree approximation, however, a many-body problem of N non-interacting particles is solved by an average potential [Sla74]. Thus it does not take exchange and correlation effects into account. For modeling of optical properties of GaN/AlN QDs the self-consistent Hartree-Fock approach is used in the present work. In contrast to the Hartree method, a Slater-determinant is used as a multi-particle wave-function. It automatically satisfies the Pauli exclusion principle and thus accounts for the exchange interaction: the determinant is zero if two wave-functions have the same quantum numbers, i.e. are linearly dependent.

The Hartree-Fock equation is solved self-consistently for four Hartree-Fock states of A and B excitons, taking into account spin of the charge carriers. The resulting states and their four linear combinations are used as a basis for the matrix expansion of the exchange operator. Diagonalizing the matrix gives the true excitonic states. These resulting wave-functions of excitonic complexes of the charge carriers, confined in the dot, can be further applied: as wave-functions of the excitonic states in the independent Boson model and for modeling the optical properties of the QD.

The calculations of wave-functions, built-in dipole moments and excitonic energies of nitride-based QDs, presented in chapters 3 and 4, were performed by Gerald Hönig.

2.3.3 Exciton-phonon interaction

To describe the interaction of the phonons and excitons in the QDs, the Hamiltonian in the framework of the independent Boson model [Tak93, Kru02] is used:

$$H = \sum_{i=\mathrm{v,c}} \epsilon_i a_i^\dagger a_i + \sum_{\boldsymbol{q},\kappa} \hbar\omega_{\boldsymbol{q},\kappa} b_{\boldsymbol{q},\kappa}^\dagger b_{\boldsymbol{q},\kappa} + \sum_{\boldsymbol{q},\kappa} \left(g_{\mathrm{vv}}^{\boldsymbol{q},\kappa} - g_{cc}^{\boldsymbol{q},\kappa}\right) a_c^\dagger a_c \left(b_{\boldsymbol{q},\kappa} + b_{\boldsymbol{q},\kappa}^\dagger\right)$$

The first term describes the creation and annihilation of the exciton of energy ϵ_i QD. Only the uppermost valence band level and the lowest conduction band level are taken into account. Interaction with the wetting layer states is neglected.

The second term describes creation and destruction of bulk phonons with phonon number κ, wave vector $\boldsymbol{q}$ and energy $\hbar\omega_{\boldsymbol{q},\kappa}$. The phonon number κ corresponds to transverse-acoustic (TA) or longitudinal optical (LO) or acoustic (LA) phonons. The dispersion relation for the phonons is taken as obtained from a standard diatomic linear chain model (Debye-Einstein approximation). All phonon branches are considered isotropic. For LO $\hbar\omega(\boldsymbol{q}) = \hbar\omega_{LO}$, for LA and TA $\hbar\omega(\boldsymbol{q}) = \hbar c_s q$, where c_s is the respective sound velocity for LA and TA phonons.

The last term describes the exciton-phonon interaction. The non-diagonal coupling (to the excited states of the QD) is neglected [Zim02, För03, Kru05b, Vag11]. Index v(c) denotes valence (conduction) band. The effective coupling element depends on coupling mechanism (deformation potential and piezoelectric coupling for the respective material system) and electron (hole) wave-functions $\varphi_c(\varphi_\mathrm{v})$:

$$g_{\mathrm{vv}}^{\boldsymbol{q},\kappa} - g_{cc}^{\boldsymbol{q},\kappa} = \widetilde{g}_{\mathrm{vc}}^{\boldsymbol{q},\kappa} \sim \left\langle \varphi_{\mathrm{v}} \left| e^{i\boldsymbol{q}\cdot\boldsymbol{r}} \right| \varphi_{\mathrm{v}} \right\rangle - \left\langle \varphi_c \left| e^{i\boldsymbol{q}\cdot\boldsymbol{r}} \right| \varphi_c \right\rangle$$

When including the phonon dispersion relation, the coupling elements for acoustic and optical phonons, the effective coupling element turns to:

$$\widetilde{g}_{ij}^{\boldsymbol{q},LO} \sim \frac{1}{q} \left\langle \varphi_j \left| e^{i\boldsymbol{q}\cdot\boldsymbol{r}} \right| \varphi_i \right\rangle;\ \widetilde{g}_{ij}^{\boldsymbol{q},LA(TA)} \sim \sqrt{q} \left\langle \varphi_j \left| e^{i\boldsymbol{q}\cdot\boldsymbol{r}} \right| \varphi_i \right\rangle$$

To predict the luminescence spectra of the QD the absorption coefficient for a δ-like excitation pulse is calculated as

$$\alpha(\omega) \sim \omega Re \int_0^\infty dt e^{i(\omega-\omega_{gap}-\triangle)t} e^{R(t)} e^{-S_{HR}}$$

Here $\triangle$ is a polaron shift of the electronic energies due to virtual phonon emission and absorption; S_{HR} - Huang-Rhys factor:

$$\triangle = -\sum_{q_\kappa} \frac{\left|\widetilde{g}_{\mathrm{vc}}^{q_\kappa}\right|^2}{\hbar^2 \omega_{q_\kappa}},\ S_{HR} = \sum_{q_\kappa} \frac{\left|\widetilde{g}_{\mathrm{vc}}^{q_\kappa}\right|^2}{\hbar^2 \omega_{q_\kappa}^2} \left(2n_{q_\kappa}+1\right)$$

$R(t)$ is determined with phonon spectral density $S(\omega)$ and phonon distribution at particular temperature $n(\omega)$

$$R(t) = \sum_{q_\kappa} \frac{\left|\widetilde{g}_{\mathrm{vc}}^{q_\kappa}\right|^2}{\hbar^2 \omega_{q_\kappa}^2} \left(\left(n_{q_\kappa}+1\right) e^{-i\omega_{q_\kappa} t} + n_{q_\kappa} e^{i\omega_{q_\kappa} t} \right) =$$

$$\int d\omega' S(\omega') \left(\left(n(\omega')+1\right) e^{-i\omega' t} + n(\omega') e^{i\omega' t} \right)$$

Phonon spectral density, giving the coupling strength to the phonons of energy $\hbar\omega$, is calculated as

$$S(\omega) = \sum_{\boldsymbol{q}_\kappa} \frac{\left|\widetilde{g}_{\mathrm{vc}}^{\boldsymbol{q}_\kappa}\right|^2}{\hbar^2 \omega_{\boldsymbol{q}_\kappa}^2} \delta\left(\omega - \omega_{\boldsymbol{q}_\kappa}\right)$$

The modeling of coupling excitons and acoustic phonons, presented in chapter 4, was performed by Matthias-René Dachner.

2.4 Growth of nitride-based samples

Up to now optimization of the growth of nitride-based QDs could not succeed in lowering the QD densities while maintaining the good optical quality of the dots. To perform single-QD spectroscopy in this work, post-processing methods as etching mesa structures or using a metallic shadow mask were applied to the nitride-based QD samples, as described above in section 2.2.

For the investigation of the nitride-based QDs four samples were chosen: two of GaN/AlN QDs and two of InGaN/GaN QDs. The two samples of GaN/AlN QDs were grown by Stranski-Krastanow mode (S-K) with metal-organic chemical vapor deposition (MOCVD) and molecular beam epitaxy (MBE) respectively. One of the samples was prepared to have a shadow mask, the other to have mesa structures. Using a metallic shadow mask is an approved method for single-QD CL spectroscopy [Tür01, Rod06] which is not necessarily suited for µPL spectroscopy as well. In contrast to this, mesa structures allow to investigate the same QDs with different spectroscopic techniques. Since thorough experiments with µPL spectroscopy had already been performed for the sample of MOCVD-grown GaN/AlN QDs, the present work paid to this sample. For the first time identical QDs were investigated by means of µPL and CL. From the comparison of the results new conclusions could be drawn regarding fundamental interaction mechanisms of excitons and phonons in the QDs.

Table 2.1: Overview of the investigated nitride-based samples.

	T	**L**	**B**	**W**
QD material	S-K GaN		In-concentrations fluctuations in InGaN	
Active layer	6.4 ML	5ML	8ML	indeterminable
Matrix material	AlN		InGaN/GaN	InGaN
Substrate	SiC	GaN	Si(111)	GaN (miscut of 2.3°)
Growth technique	MOCVD	MBE	MOCVD	MBE

The samples with InGaN QDs present an alternative fabrication approach as compared to S-K GaN/AlN QDs. No structurally-distinct islands are formed on the wetting layer. Instead, the zero dimensional confinement of the charge carriers takes place in regions of increased In-concentration: In one of the samples, grown with MOCVD, In-segregation is observed in a thin InGaN layer, included in a GaN-matrix. In another sample such In-rich QD-like structures are formed on the steps of atomic monolayers, created through miscut of the substrates.

The growth process has an immense impact on the crystal quality and consequently the optical properties of the QDs. Various QD growth approaches are particularly important for the investigation of SD of the exciton luminescence. Comparison of the different samples allows to suggest which effects are customary for the nitride

QD material system and which features are induced by certain types of defects, characteristic for the respective growth mode.

Table 2.1 contains a short overview of the investigated nitride-based samples. More detailed information about sample structure, growth parameters, and structural investigations follows below in this section. An integral CL spectrum on a linear intensity-scale for each sample is included as well.

GaN/AlN: sample T

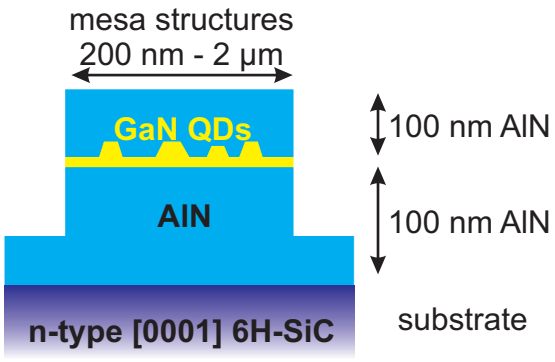

Figure 2.6: Structure of the sample T.

Sample T was grown and processed in the Research Center for Advanced Science and Technology, University of Tokyo, Japan. The sample structure is depicted in figure 2.6. A detailed growth description can be found in [Hos04]. Wurtzite-type GaN/AlN QDs were grown by low-pressure MOCVD in the S-K mode on (0001)-oriented 6H-SiC substrates. A 100-nm thick AlN layer was grown at 1180° C. Afterwards 6.4 monolayers (ML) of GaN were deposited at 975° C, subsequently the growth was interrupted to allow QD formation. The capping layer was grown in two steps, as good-quality AlN requires a higher growth temperature than the GaN QDs. A 4 nm-thick layer of AlN was first deposited at 975° C, followed by 96 nm of AlN at 1180° C.

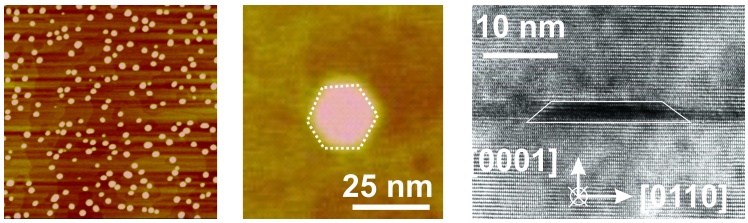

Figure 2.7: Left: AFM image of an uncapped sample T. Right bottom: AFM of an uncovered QD. Right top: Cross-sectional TEM image of a covered QD. Images are taken from [Kak05].

The transmission electron microscopy (TEM) and cross-section TEM investigations of the sample confirm the S-K QD growth mode and WL formation [Hos04]. The thickness of the wetting layer (WL) is determined to be 2-3 MLs. The TEM analysis of overgrown as well as of atomic force microscopy (AFM) images of the uncapped samples reveal, that the QDs have the form of a truncated hexagonal pyramid (see figure 2.7), an average height of ~4 nm, and an average diameter of 25 nm.

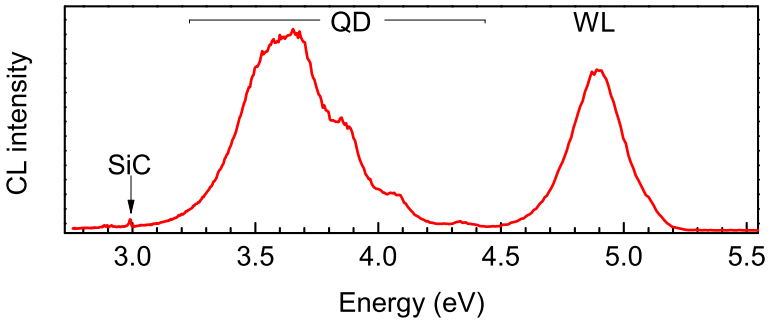

Figure 2.8: CL of the QD ensemble of sample T.

Figure 2.7 shows the AFM image of the uncapped sample. The estimated QD density is $6{\times}10^9$ cm^{-2}. The samples were processed into mesa structures by means of electron-beam lithography. The mesas have diameters ranging from 200 nm to 2 µm. Approximately two QDs are to be found in the smallest mesa.

The CL of a QD ensemble, measured at 5K, is depicted in figure 2.8. WL has almost the same intensity as the QD ensemble. The QD ensemble shows a pronounced oscillatory behavior. These luminescence bands correspond to subsets of dots of different heights, in a sequence following an integer number of MLs. The luminescence of around 3.0 eV is attributed to SiC.

GaN/AlN: sample L

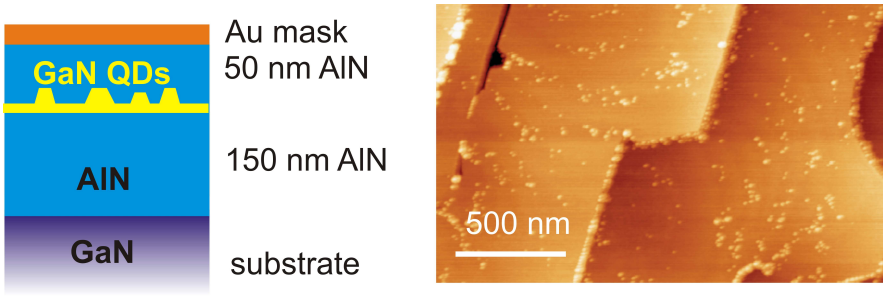

Figure 2.9: Left: Sample structure of sample L. Right: AFM image of an uncapped sample [Sim08a].

Sample L was grown at the École Polytechnique Fédérale de Lausanne, Switzerland. The structure is similar to that of sample T and is shown in figure 2.9. A gold mask with apertures between 200 nm and 1 µm in size was put on top of the sample.

These QDs were grown with MBE in the S-K mode. A detailed growth description can be found in [Sim08a]. 100 nm of relaxed AlN were deposited on a 2 µm thick *c*-plane GaN template. 5 ML of GaN were deposited at 830° C subsequently the ammonia flux was interrupted to reduce the GaN island density. The higher temperature of 830° C instead of conventional 800° C [Dam99] is used to promote Ga ad-atom diffusion an the surface.

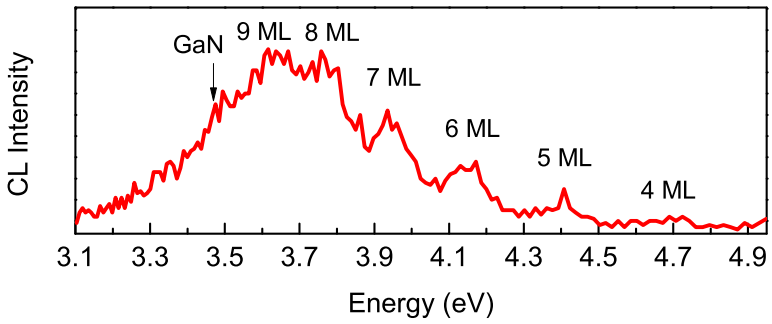

Figure 2.10: CL of the QD ensemble of sample L.

Multiatomic step edges on the AlN layer, decorated with large GaN islands, can be seen in the AFM image of an uncapped sample, shown in figure 2.9. These step edges act as preferential dot nucleation sites [Mat05], the dot density on the terraces is therefore reduced. The average height of the GaN islands on the edges is ~ 4.5 nm, on the terraces ~ 1 nm (here the estimated aspect ratio of height to width of the islands is ~ 0.15). The island density is of the order of 10^9 cm^{-2}, the WL thickness is around 2 ML.

The CL of the QD ensemble, measured at 5K, is displayed in figure 2.10. Similar to sample T the QDs of different heights are easy to identify. GaN-template luminescence at 3.48 eV is indicated by an arrow. For more details on the luminescence properties of the sample see [Sim08a, Sim08b].

InGaN(/GaN) QDs: sample B

Sample B was grown with MOCVD at Technische Universität Berlin, Germany. A detailed description can be found in [Rod06]. The structure is shown in figure 2.11. The sample was grown on Si(111)-substrate. The initial layer of AlN, 400 nm $Al_{0.05}Ga_{0.95}N$ and 600 nm GaN were grown at 1150° C. A layer of InGaN of a nominal thickness of 2 nm was grown at 800° C, followed by 20 nm GaN grown at 1100° C.

In-concentration fluctuates in the InGaN layer. Under certain growth conditions this can lead to the formation of nanometer scale In-rich domains, which present strong

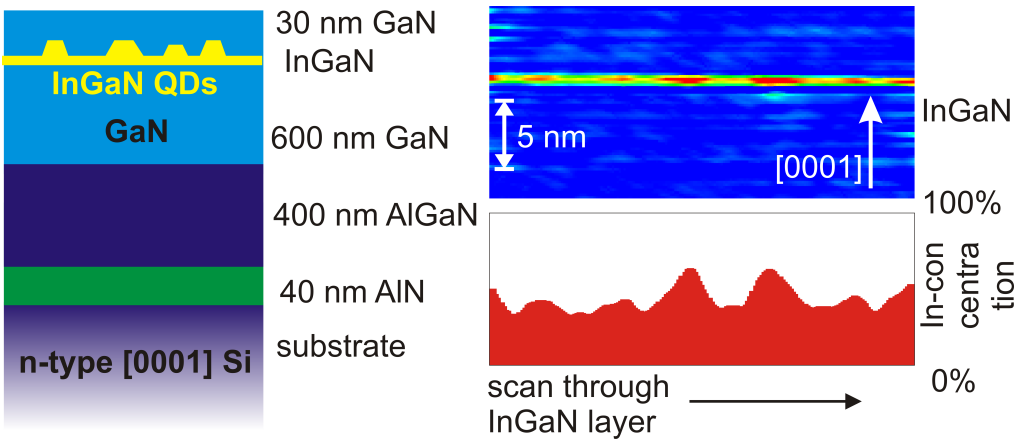

Figure 2.11: Left: structure of sample B. Right (top): High resolution TEM image, DALI-processed; (bottom) The profile of In-concentration along the InGaN-layer. Figure adopted from [Rod06].

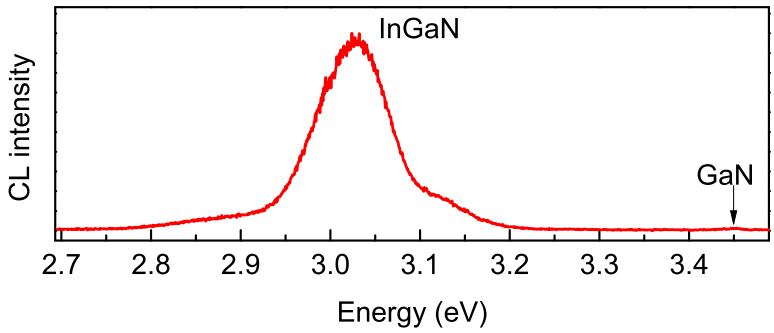

Figure 2.12: CL of the QD ensemble of sample B.

charge carrier localization centers and exhibit QD-like optical properties [Seg04, Win07].

Structural information about the samples was obtained from high resolution TEM measurements, performed under short irradiation times to prevent electron beam induced artifacts [Sme03]. The DALI-processed[2] results are depicted in figure 2.11. In-concentration varies along the InGaN-layer and the In-rich domains have the lateral size of up to 5 nm.

A platinum mask with apertures from 200 nm to 2 µm in diameter was applied on the surface of the sample to allow investigation of individual QDs. Such shadow masks were already used in earlier experiments with CdSe [Tür00a] and InAs [Rod03] QDs. The mask is fabricated as follows: A solution containing polystyrene spheres of various diameters is applied to the sample surface. The metal film is sputtered onto the sample subsequently. Finally, the spheres are removed from the sample in an ultra-sonic bath with ethyl acetate. The metal should preferably have an absorption

[2] DALI - digital analysis of lattice images [Ros99]

coefficient as high as possible at the emission wavelength of the investigated QDs.

The CL of the QD ensemble of the sample, measured at 5K, is depicted in figure 2.12. The broad luminescence band, marked "InGaN" in the figure, disintegrates into sharp peaks, when resolved through metal mask. No luminescence of the 2D InGaN layer is found. A weak luminescence of GaN is indicated with an arrow.

InGaN: sample W

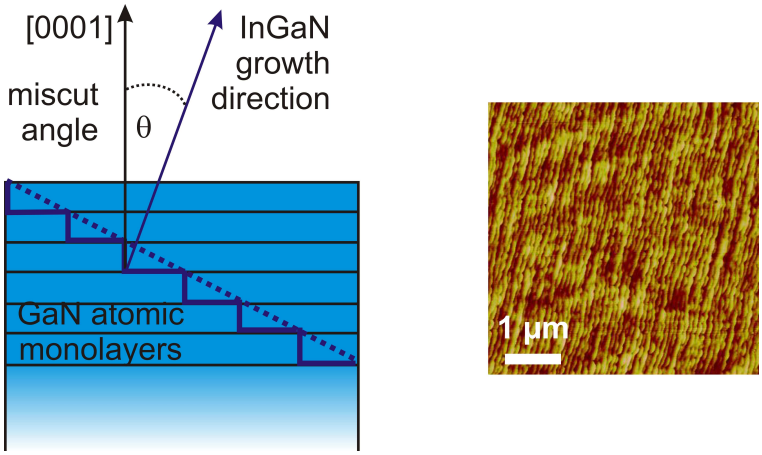

Figure 2.13: Left: Miscut schema of sample W (adopted from [Per09]). Right: AFM image of the sample surface, showing the terraces created after polishing.

Sample W was grown at the Institute of High Pressure Physics Unipress, Polish Academy of Sciences, Warsaw, Poland. A different approach compared to sample B was used. Here 120 nm thick $In_{0.1}Ga_{0.9}N$ layers were grown at 820° C with MOCVD on a 0.5 µm GaN buffer layer. Finally, InGaN was capped by 25 nm of GaN [Kry07]. Here the crucial point is the miscut of the free-standing GaN substrates. The miscut is produced by mechanical polishing. The miscut angle is $\theta = 2.3°$ toward $[11\bar{2}0]$ (see figure 2.13). Reactive ion etching was applied subsequently to remove the mechanical damage. The substrates were fabricated by means of vapor phase epitaxy and have a dislocation density of about 10^7 cm^{-2}.

The intentional miscut of the substrates controls the spacing of the growth steps on the growth surface. Figure 2.13 shows an AFM image of the polished sample surface, where the steps of the GaN atomic monolayers can be seen.[3] Depending on the miscut angle larger, or smaller edges can be created. The diffusion of the ad-atoms to the steps is limited. Under certain growth conditions and for certain miscut angle the assembled In-nuclei at the step edges can create small areas, which provide strong charge carrier localization. It is observed as QD-like emission lines in

[3] AFM measurements done in Institute of High Pressure Physics, Polish Academy of Sciences, Poland.

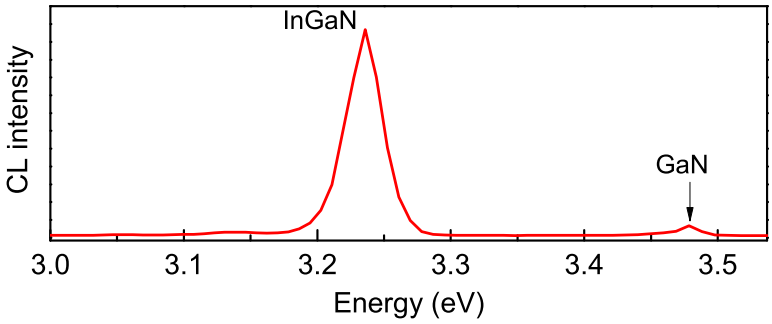

Figure 2.14: CL of the QD ensemble of sample W.

the CL experiments. Similar to sample W, the fluctuation of the In-concentration in the InGaN layer creates 0D charge carrier localization centers.

The CL of QD ensemble of the sample, measured at 5K, is depicted in figure 2.14. Luminescence of GaN-template is indicated.

Results: nitride-based quantum dots

3 Interaction with local electric fields

This chapter deals with the interaction of charge carriers confined in a quantum dot (QD) and an electric field in its environment. Such interaction affects the luminescence of a QD and leads to an effect called "spectral diffusion" of QD luminescence (SD). In the investigation of QDs by means of cathodoluminescence (CL) spectroscopy the SD was found to be composed of different components, which exhibit significantly different timescales.

The first section gives a short overview of important results, related to the topic of the chapter. Section 3.2 is dedicated to the short-timescale SD, resulting in line broadening of emission lines. The influence of sample surfaces and excitation conditions on the linewidths is studied. Section 3.3 refers to long-timescale SD and describes observed luminescence intermittence and slow spectral jitter of the single QD emission lines. This section explains how the slow SD is used as a tool for the investigation of single QDs. A particular case of the long-timescale SD, the so-called χ-pattern, is presented for the first time within the frame of this work in section 3.4. A model of this process is proposed and can be generalized to give an explanation of slow spectral jitter of excitonic emission of nitride-based QDs. In addition, this chapter shows for the first time how to determine the absolute value and the ratio of the built-in dipole moments of different excitonic complexes from characteristic shifts of the QD emission lines.

Exclusively experiments on the nitride-based QDs are presented in this chapter. Additional results on SD for site-controlled InGaAs/GaAs QDs are presented in chapter 5. Investigations of QD samples, grown with different growth approaches, allow to draw conclusions about defects responsible for particular component of SD and specific properties of the nitride QD material systems. Earlier micro-photoluminescence (μPL) experiments on a GaN/AlN QD sample have investigated the luminescence properties with a resonant excitation. The same mesa structure can be investigated with CL. Comparing the results of CL and μPL experiments allows to reveal the influence of resonant and non-resonant excitation on SD.

©Calculations of the excitonic shifts of a model InGaN QD in an electric field of a point charge and dipole moment ratios of the model GaN/AlN QDs were performed by *Gerald Hönig*.

3.1 State of the art

The term "spectral diffusion" was introduced in connection with spectroscopic studies of colloidal CdSe QDs in [Emp96]. In self-assembled QDs the effect of SD is widely observed too. SD was observed in the luminescence of QDs of different material systems: selenides [Tür00a, Seu00, Bes02], arsenides [Rob00, Bes01, Rod05], nitrides [Ric04, Bar06, Rol07], and phosphides [Pis99, Blo00, Pis01].

The origin of SD is commonly explained by the interaction of the excitonic state in the QD with stochastically fluctuating electric fields in the vicinity of the QD, which are generated by random charging and discharging processes in the barrier material: see section 1.3 for quantum confined Stark effect (QCSE) in QDs.

A profound understanding of the mechanism behind the phenomenon of SD is needed, since SD can become a significant obstacle in the context of efficient single-QD applications. SD manifests itself in broadening (in this work distinguished as short-timescale SD), spectral jitter and on/off blinking (in this work both types distinguished as long-timescale SD) of the emission lines. Unstable intensity, random positions and broadening of the luminescence lines are detrimental for potential use of QDs. Up to now, however, no detailed microscopic model of the interaction process has been presented. Such a model would probably allow to draw conclusions for the growth process, finally allowing to utilize or eliminate SD.

Defects can act as charge traps or non-radiative centers, thus playing a crucial role for the SD. The surface of a crystal possesses a huge number of natural defects. If a QD is situated close to the surface, enhanced SD can be induced. Interactions with surface states become crucial for QDs situated very close to the surface. For InAs/GaAs QDs it ranges between 10 and 14 nm, as shown in investigations of luminescence linewidths in [Kam98, Faf00, Wan04].

QDs farther away from the surface are affected by fields generated by a large variety of defects in the bulk material. Large efforts have been made to reduce SD by optimized growth approaches. However, it is probably impossible to eliminate SD completely.

SD tremendously affects the widths of emission lines of excitonic transitions in QDs. A large number of experimental studies have been performed to investigate the influence of the excitation conditions on the linewidths: e.g. [Tür00b, Blo00, Ber06, Fav07, Abb08, Kin10b]. In [Ber06, Fav07] the SD-induced broadening of a QD emission line is described using a model including charge carrier dynamics outside the dot. The authors deduced a dependence of full width at half maximum (FWHM) of a single dot emission line on population fluctuations in the impurities around the dot. In [Abb08] particular attention was paid to the difference in measured linewidths of X, XX and X^+ of GaAs/AlGaAs QD. This difference is attributed to different polarizabilities of the excitonic complexes, which was shown in the same work in calculations of Stark shifts of the excitonic transition.

The division of SD into short- and long-timescale is arbitrary. If the experimental set-up does not allow to temporally resolve different spectral positions or intensity values of QD luminescence, then the measured emission peak appears broadened or has a small intensity (if the on/off blinking of the emission line is present). Therefore, it is important to be aware of the real timescale of processes influencing the SD.

SD is the main reason for the inhomogeneous broadening of the excitonic transitions in the QD. The contribution of homogeneous broadening to the width of QD emission lines can be evaluated from four-wave-mixing experiments, which reveal dephasing times. The dephasing time was measured to be of several hundred picoseconds in [Bor01, Bir01] for arsenide QDs and in [Pal03] for CdSe nanocrystals. Additionally, in [Pal03] the dependence of linewidth of the excitonic transition on the modulation frequency of the excitation signal was studied. Below 1 MHz SD induced a large broadening and the linewidth decreased rapidly down to 6 µeV for a frequency increase to a few MHz. This experiment pointed out the timescale of SD in colloidal QDs is in the order of microseconds.

Even shorter time constants were revealed in [Sal10a], obtained from auto-correlation measurements on CdSe/ZnSe QDs, embedded in nanowires. In this work the cross-correlation between the low- and high-energy sides of the emission line and the auto-correlation of signal from one side only were measured. These experiments showed, that the QD emission line stays homogeneously broadened during 4 ns. Both [Pal03] and [Sal10a] confirm that the characteristic SD times can be as short as nanoseconds.

However, other processes attributed to SD as well, can have rather long characteristic times. Often a QD luminescence line, already broadened, shows continuous or discrete spectral shifts: e.g. [Tür00a, Bes02, Rod05, Bar06]. Also, intensity variations or even quenching of the QD emission are sometimes observed both in colloidal [Neu00] and self-assembled [Rod05] QDs. Such intensity instability was reported under various names: e.g. telegraphic noise [Pis99, Pis01, Pan01, Pan02] and two-color blinking [Ber99]. In GaN/AlN QD material system blinking was also observed: [Bar06, Kin09]. The two types of SD, spectral jitter and intensity intermittence, prove themselves helpful for the identification of the lines from one and the same QD [Tür00a], as each QD exhibits its own sequence of Stark shifts or intensity variations.

QCSE, and of course SD, is particularly essential in nitride-based QD due to large built-in polarization fields (see section 1.1.4). A combined experimental and theoretical study of QCSE in single GaN/AlN QDs was described in [Nak06b, Nak06a]. The shift of the excitonic energy of a single QD was measured under constant longitudinal and in-plane electric fields applied to the sample. For the electric field in the growth direction the excitonic energy shift was shown to have a linear dependence on the field magnitude, resulting in $\mu_{built-in} = 1.15\,\mathrm{e}\cdot\mathrm{nm}$; for the electric field perpendicular to the growth direction - a quadratic dependence. The measured data correlate with self-consistent effective mass calculations ibid. The quadratic

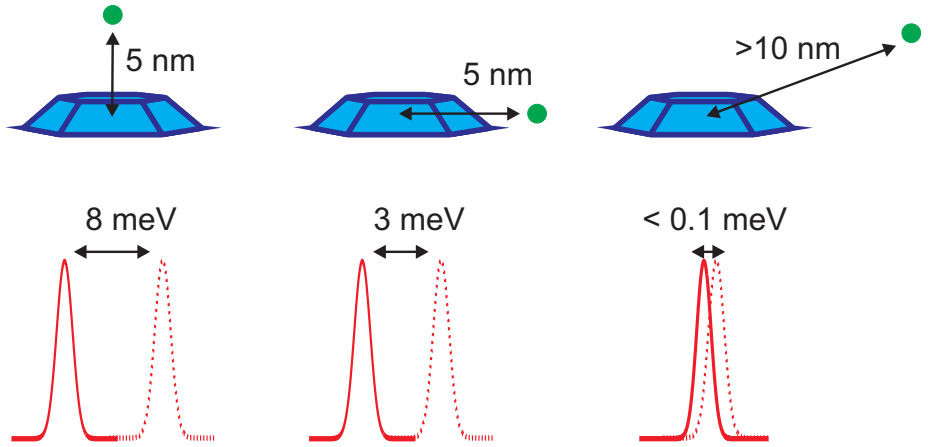

Figure 3.1: Spectral shift of a QD emission line, induced by a point charge placed at various positions close to the dot. The values are estimated from experimental data of the shift of an excitonic emission line in constant electric fields in [Nak06b, Nak06a].

relation together with the large obtained value of $\mu_{built-in}$ prove experimentally, that the direction of built-in dipole moment $\boldsymbol{\mu_{built-in}} = \boldsymbol{\mu_0} + 2\alpha \boldsymbol{F_{int}}$ can be considered as parallel to built-in field $\boldsymbol{F_{int}}$. Consequently, the intrinsic dipole moments of GaN/AlN dots can be considered parallel to the built-in filed direction: $\boldsymbol{\mu_0} \parallel \boldsymbol{F_{int}}$. Same way as for QDs of other material system, an intrinsic dipole moment an stem e.g. from a composition gradient [Fry00] or shape [Gru95, Sti99] of the dot.

Based on these experiments, a simple estimation can be made for the GaN/AlN QD material system to predict the influence of a point charge in the close vicinity of a dot on its excitonic luminescence. A point charge at a distance of 5 nm to the dot induces a field of ≈ 60 kV/cm at the dot center. Such an electric field in the growth direction and in the plane of the QD results in excitonic energy shifts of 8 meV and 3 meV respectively. Any point charge at a distance of 10 nm or more should induce a shift of only fractions of meV. These estimations are taken from [Bar06] and are displayed in figure 3.1.

Such point charges can be the reason for the random spectral jitter. Single QDs exhibited energetic shifts up to several meV in experiments on InGaN QDs [Ric04, Seg04] and GaN/AlN QDs [Bar06]. However, only speculations about the origin of the spectral jitter are given. To date no model or detailed calculations for the interaction of a QD and single charges have been proposed.

Nitrides are particularly defect-rich materials. QDs grown in this material system exhibit very broad lines in emission spectra, as compared to other QD material systems (e.g. arsenides). Linewidths from several meV down to the best values of 500 µeV are typically observed: e.g. [Bar06, Kak06, Sim08b, Dem09]. These large linewidths are attributed to the large built-in polarization fields.

As shown in section 1.3.3 for a variation of the local electric field $\triangle F \ll F_{int}$ the

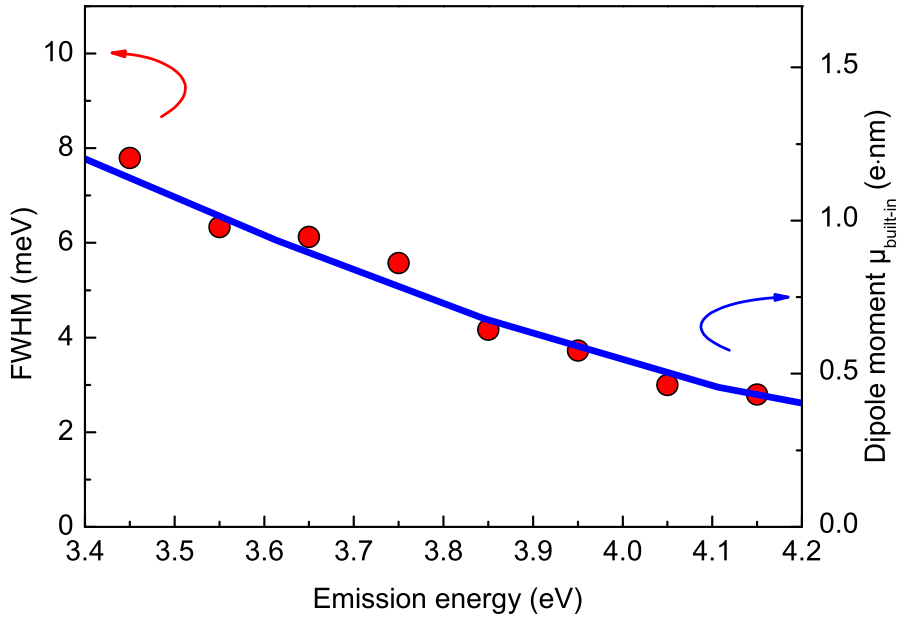

Figure 3.2: Dependence of the linewidth from µPL-experiments and calculated dipole moments of an exciton for the given emission energy.

change of the excitonic transition energy is

$$\Delta E(\triangle \boldsymbol{F}) = \boldsymbol{\mu_{built-in}} \cdot \triangle \boldsymbol{F} \tag{3.1}$$

Large $\mu_{built-in}$ makes the nitride QDs sensitive even to weak local electric field fluctuations. Inhomogeneous line broadening due to SD is a shift of the exciton energy, averaged for the measurement time in the experiment $\triangle t$:

$$\Gamma_{SD} = \overline{\Delta E}_{\triangle t} = \mu_{built-in}\overline{\Delta F}_{\triangle t} \tag{3.2}$$

Consequently, Γ_{SD} becomes significant for nitride QDs and scales with the permanent dipole moment $\mu_{built-in}$ of the exciton. Built-in dipole moment increases with the size of the QDs. The line broadening is expected to be larger for QDs with larger excitonic dipole moments, in other words with smaller emission energies.

Such a tendency was shown in µPL experiments on GaN/AlN QDs in [Kin10b]. The dependence of the linewidths of excitonic transition on the emission energy was investigated, as shown in figure 3.2. The FWHM of the emission lines increases as their emission energy decreases. In the figure circles depict the mean value of linewidths. The solid blue line shows the estimations of the dipole moment obtained from theoretical calculations for the model QDs with respective emission energies as observed in the experiments. Calculations are performed in a one-band effective-mass approximation in a self-consistent Hartree scheme for a series of model QDs with equal aspect ratio and increasing size [Kak05].

3.2 Short-timescale spectral diffusion (line broadening)

A large number of emission lines were measured in CL experiments on GaN/AlN QDs. Unless otherwise indicated, the experiments described below are performed on the sample T under the following excitation conditions, referred to hereafter as "normal": Electron acceleration voltage was set to 7 kV, allowing for a spatial resolution of 775 nm. The electron beam current was 1 nA. These excitation conditions were found to result in a sufficient signal-to-noise ratio (SNR) already at detection times of 50 ms per spectrum.

Change of the local electric field in the surrounding of the QD results, generally speaking, in a shift of the QD emission line. In particular, the dynamics of charge-trapping and -release in the defects result in line broadening. Therefore, the detection time is an important parameter of the measurements. The influence of detection time on the linewidth of the emission line was investigated first.

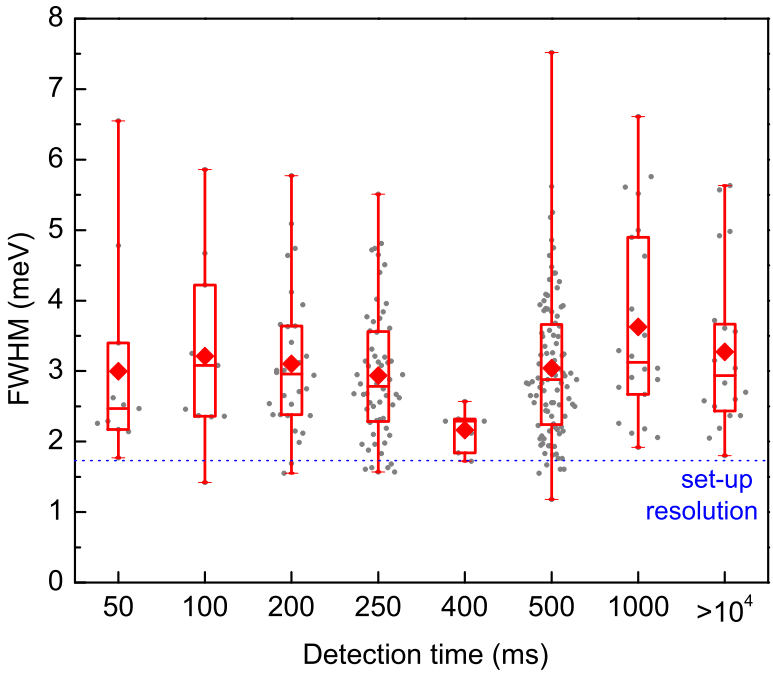

Figure 3.3: Statistics of measured linewidths for different detection times.

Figure 3.3 shows a box-plot of the statistics of the emission linewidths in dependence on detection time, measured under normal excitation conditions. The shortest time resulting in the SNR, sufficient to measure the FWHM of emission peaks, was 50 ms. It was not investigated, which excitonic complexes the lines stem from. Data are shown exclusively for lines, that could be clearly separated from adjacent lines. No line shape fitting procedure was applied. For each peak the energetic position E_0

of the maximum intensity was defined $I(E_0) = I_{max}$, then the difference between the closest data points calculated, for which $I(E_{left,right}) = I_{max}/2$: FWHM $= |E_{left} - E_{right}|$. The presence of some data points below the resolution limit is an artifact of the processing software in the case of peaks with a low SNR.

This so-called box chart is a convenient way to display large groups of data. The gray circles depict the extracted data. All the data for the box in fact have the same abscissa: only integration times 50 ms, 100 ms, 200 ms, etc. were used; the scatter of the respective gray circles for each box makes for a better illustrative representation. For each data set the ends of the whiskers show the minimum and maximum; the rhombus indicates the mean value and the horizontal lines in each box from bottom to top indicate the 25-, 50- and 75-percentiles.

Figure 3.3 shows the scatter of measured FWHMs up to 6-8 meV. The mean values of FWHM for different detection times are in the range of 2.3 meV-3.7 meV independent of detection time. Another important conclusion from figure 3.3: Even at the shortest detection time, the emission lines appear larger than the resolution limit of the set-up, indicated by a blue dashed line in figure 3.3: 1.65 meV at 4.0 eV. Thus, no deconvolution of the broadening induced by the measurement system is necessary to investigate the properties of GaN/AlN QDs under the prevailing experimental conditions.

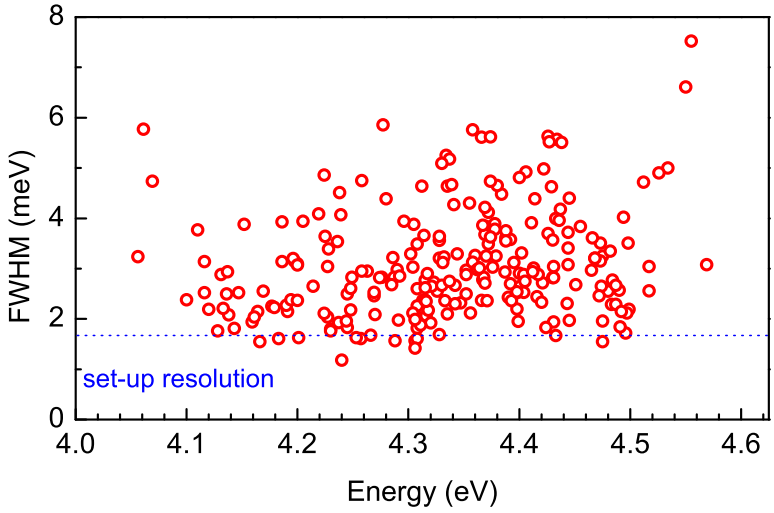

Figure 3.4: Dependence of the measured FWHM on the emission energy.

Figure 3.4 shows the statistics of the large number of investigated QDs. Here the FWHM of the emission peaks is depicted in dependence on the emission energy. For every detection energy emission lines with various FWHM were observed. In contrast to figure 3.2, no clear tendency can be seen. As shown in equation (3.2), the scatter of the FWHMs indicates strong variations from dot to dot either of the built-in dipole moments $\mu_{built-in}$ or the fluctuations of the local electric field $\overline{\Delta F}_{\triangle t}$, averaged during detection time $\triangle t$.

As can be concluded from integral CL spectrum for QD ensemble in section 2.4, the energy range in figure 3.4 corresponds to the QDs of two sub-ensembles with the same height: 5 ML and 4 ML of GaN. Theoretical calculations predict very similar $\mu_{built-in}$ for QDs of the same height. However, lateral charge carrier confinement influences the distribution of the wave functions and has an impact on the value of the built-in dipole moment. Therefore, built-in dipole moments of the dots with the same emission energy can vary and result in different Γ_{SD} (figure 3.4). Section 3.3.3 shows further, that different (multi)excitonic complexes of the same dot possess various built-in dipole moments, and this effect is enhanced for smaller QDs - i.e. the energy range shown in figure 3.4). A significantly different $\overline{\Delta F}_{\triangle t}$, experienced by each dot, is also possible, if in the crystal close to the dots the defect distribution is very inhomogeneous.

Various factors influence the SD and thus the linewidths of the emission lines: position of the QD relative to the sample surface, excitation density, temperature, type of excitation. The corresponding experiments and results are described below.

3.2.1 Influence of sample surface

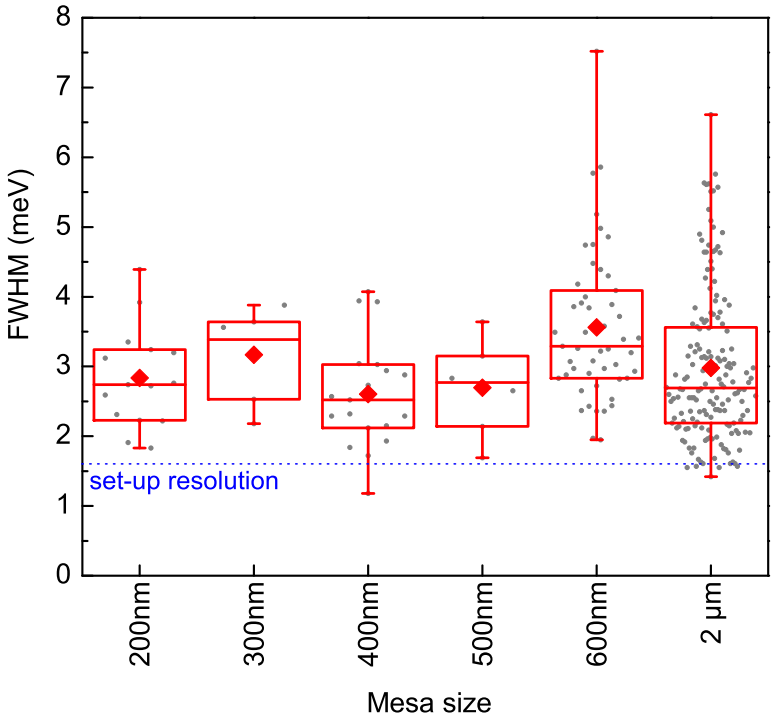

Figure 3.5: Measured linewidth for mesas of different sizes.

In this section the influence of sample surface and heterostructure interfaces on the SD of the QDs is discussed. QDs have a distance of 100 nm to the top-surface

(sample T, section 2.4), in this case a point charge trapped in the surface states would induce an electric field of ~160 V/cm in the vicinity of a dot (2 V/cm if the electrostatic screening via free charge carriers in the Debye approximation is taken into account). Such field does not have a significant influence on the GaN/AlN QD emission ([Nak06b, Nak06a]). In this case any fluctuations of the charges in the surface states cannot lead to the broadening of the order of meV, as normally observed for this QD material system. The same is valid for the AlN/SiC interface, which also has a distance of 100 nm to the QDs. Additionally, experiments with varying the thickness of the capping layer revealed similar linewidths [Kin10b]. Thus in the following discussion of the described CL experiments the influence of the top-surface and AlN/SiC interface is neglected.

The sample was processed into mesa structures of sizes from 200 nm up to 2 µm. In contrast to the top-surface, the surface of the sides of a mesa structure is very close to some QDs. Even for the mesas of 200 nm in diameter with the smallest possible excitation volume in CL experiments (225 nm in diameter for 3 kV) the whole plane of the mesa as well as a large area of the surface on the sides are excited. If the surface charges on the mesa side influence the SD, the widths of emission lines obtained from the QDs in the mesas of the smallest sizes should appear larger in comparison to mesas of larger sizes.

Figure 3.5 shows statistics of the linewidths measured for different mesa diameters. Again a box chart is used. The values range from the resolution limit up to 8 meV. No correlation between linewidth and mesa size can be detected. The mean values of the measured FWHMs for the mesa structures of different sizes are similar: 2.75 - 3.5 meV.

Unprocessed samples (without mesa structures and grown in the same run with T) were investigated too. No obvious difference to samples with mesa structures were found. Furthermore, measurements of a different GaN/AlN QDs sample L (GaN/AlN, MBE growth) showed linewidths of the same range, although no mesa structures existed in the samples. In both cases of samples without mesa structures the FWHMs scatter from 8 meV down to resolution limit, the mean FWHM was found to be 2.9 meV: the same as shown in figure 3.5.

To sum up, no clear impact of surface states on the sides of the mesa structures could be observed. The bulk defects in the GaN/AlN heterostructure are decisive for the linewidths of the QDs, independent of growth technique.

3.2.2 Influence of excitation density

One straightforward experiment for the investigation of the line broadening is variation of the excitation density. Change of the number of free charge carriers in the material influences the charge trapping dynamics in the defects in the QD surrounding. Resulting different energetic shifts of the excitonic transition should lead to different line broadening for different excitation densities. For higher excitation

densities more defects are activated or the process of charge trap and release is accelerated. The increase of the linewidths caused by increasing excitation density was indeed revealed in many experiments: [Tür00a, Blo00, Ber06, Fav07, Kur07].

In CL experiments the excitation density can be varied by three different methods: Varying the electron acceleration voltage or the electron beam current and moving the electron beam across the sample. The last way is the most reliable, since it is impossible to state unambiguously in which way change of the electron acceleration voltage or the electron beam current influences the excitation density [Tür01]. Excitation of a QD, when the SEM beam is placed directly over the dot, definitely corresponds to a higher excitation density compared to an excitation, when the beam is placed at some distance from the dot.

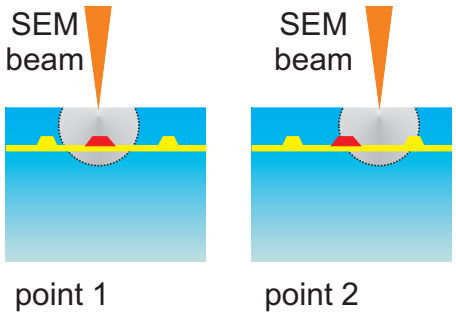

Figure 3.6: For the placement of the SEM beam onto point 1 and point 2, different excitation densities are created for the QD, indicated in red.

The effect of the change of the excitation density is dependent on the position of the electron beam, as shown in figure 3.6. When CL spectra are recorded while moving the electron beam across the sample, the change of the excitation condition of the QD can be seen clearly in the spectra as a change of the CL intensity of the QD emission line combined with the appearance/disappearance of the additional emission lines from the same dot or emission lines from a different dot.

The variation of the measured luminescence for different positions of excitation is displayed in figure 3.7. Four spectra are extracted from the data set, obtained from one of the experiments with the beam scanning over the sample. The acceleration voltage was 15 kV, the electron beam current was 0.3 nA and detection time was 1000 ms. The emission line L1 at 4.29 eV appears with different intensities in the spectra, when electron beam is placed on different sites. Some emission lines appear (L2 at 4.32 eV in panel 4, emission QD2 at 4.25 eV in 1-4) and some disappear (emission QD3 at 4.16 eV in 1-3) in the spectrum with changing the position of the electron beam. This assignment of the line groups to particular QDs can be done with the help of longtime-scale SD, as described below in section 3.3: from the SD-patterns for these emission lines (measured in a different experiment and not shown here) it was found that L1 and L2 stem from the same QD, emission QD2 - from a different one and QD3 - from a third one.

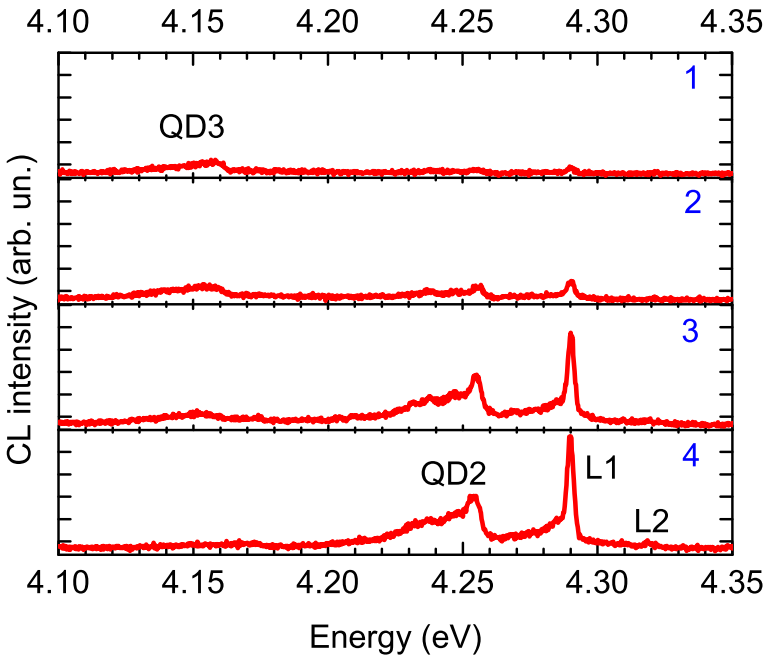

Figure 3.7: Spectra obtained by different position of the electron beam on the sample.

To investigate the influence of the excitation density on the excitonic emission linewidth, the widths for the selected lines were measured in different spectra corresponding to different positions of the electron beam. In this way several data sets, obtained by scanning the electron beam over the sample, were analyzed. For six dots the same excitonic line was carefully fitted with a Gaussian profile[1] in each spectra. No change in the linewidth, obtained from these fits, was found.

At different electron beam current and electron acceleration voltages the luminescence spectra from the same excitation point appeared significantly different, similar to the one shown in figure 3.7. This observation indicates unequal excitation density for the different excitation parameters. Although, the dependence of excitation density neither on electron beam current nor on acceleration voltage is known, the dependence of FWHM on these parameters was measured. For two QDs a variation of the electron beam current for various electron acceleration voltages was performed. In the available range of tuning of the electron beam current (0.01 nA-2 nA) and acceleration voltage (3 kV-19 kV) the FWHM of the same dot does not change within the experimental error of the measurements. As an example the result for one dot is depicted in figure 3.8. Here for every data point the FWHM was derived from a fit of the emission peak with a Gaussian profile. No clear dependence of FWHM on acceleration voltage or electron beam current could be observed.

To conclude, no clear dependence of linewidths on the excitation density could be

[1]Explanation, why the Gaussian profile was chosen, can be found on page 96.

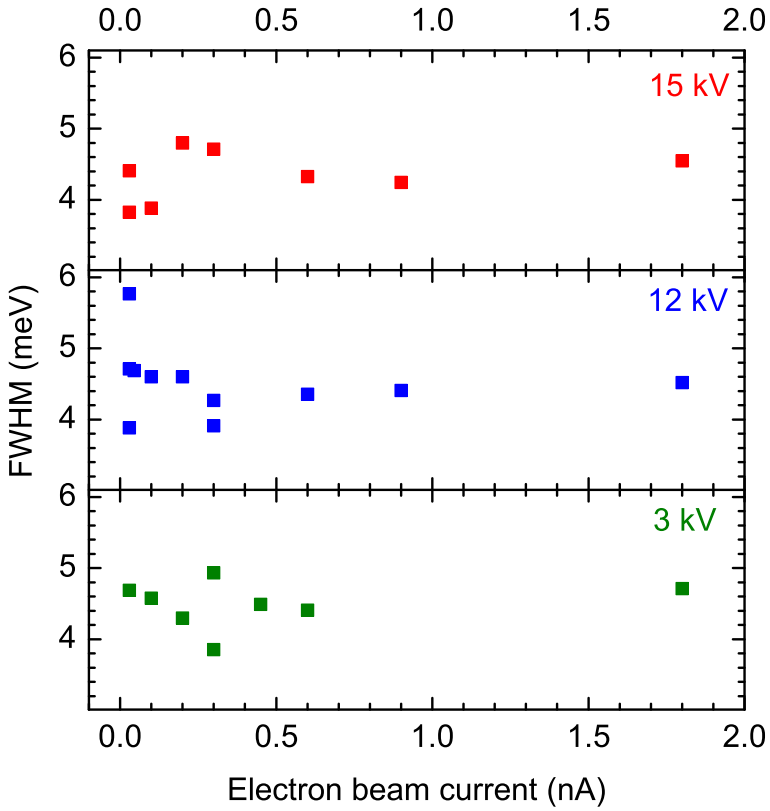

Figure 3.8: An example of the dependence of the linewidth on electron beam current for three electron acceleration voltages.

observed for GaN/AlN QDs. The most probable explanation: for this QD material system already at small excitation densities in CL experiments all defects in the vicinity of the QD are activated and affect QD emission lines.

3.2.3 Influence of temperature

With raising temperature the dynamics of charge trap and release in the defects can change and additional defects can become activated, leading to a change of the emission line broadening. The dependence of the linewidth on temperature was investigated for emission lines from five different QDs. Their FWHMs increase with raising temperature.

No dependence of the linewidth on detection time was found at 5 K. Consequently, faster recharging of defects responsible for short-timescale SD should not lead to the increase of of the FWHM. Faster spectral jitter (long-timescale SD) can become unresolvable at the same measurement times and therefore start contributing to the line broadening at higher temperatures. However, no significant acceleration of the spectral jitter rate was observed in the experiments at elevated temperature.

As shown in the previous section, no impact on the excitation densities was observed as well: all defects in the GaN/AlN QD material system are activated in CL excitation already at 5 K. Therefore, with raising temperatures no additional activation of defects, responsible for line broadening, should take place, since excitation energies in CL experiments are significantly larger than kT.

To sum up, the observed increase of FWHM with raising temperature is rather attributed to enhancement of interaction with lattice vibrations, than to temperature dependence of the SD. For more details see section 4.4, where the analysis in terms of interactions with phonons is given.

3.2.4 Influence of excitation mechanism

Sample T was studied previously in complementary µPL experiments [Kin10b]. The statistics of linewidths of the QD emission lines was analyzed. Matching these previous results to the above results from CL experiments the QD luminescence in experiments for two distinct types of excitation can be compared. The difference between the two techniques is schematically shown in figure 3.9. In µPL-experiments a laser with an emission energy of 4.66 eV was used and the carriers were excited resonantly in the QD ensemble. In CL primary electrons of the excitation beam of a SEM have an energy of several keV: the excitation takes place with much larger energy and charge carriers are excited in the barrier-material (AlN) also.

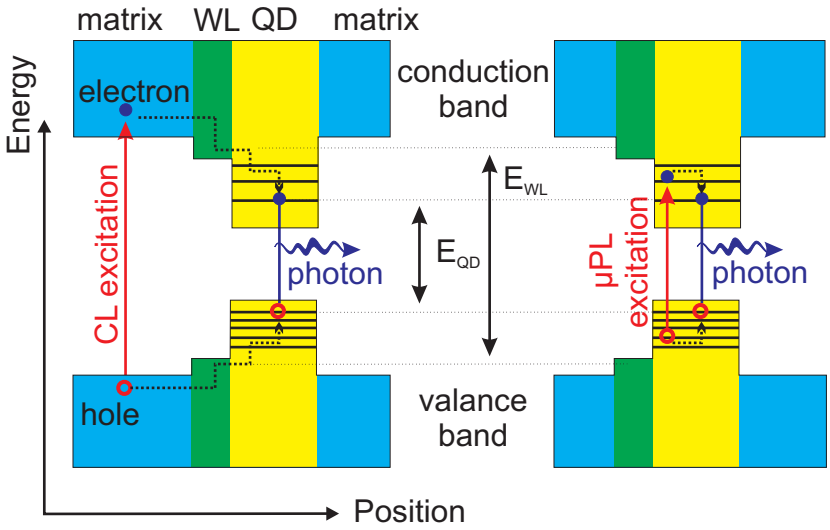

Figure 3.9: Excitation schema for CL (left) and PL (right). The effects of built-in fields are not included into the schema of the band diagram.

The spectral resolutions of the µPL and CL set-up are equal. In the µPL experiments the FWHM of the emission lines scatters from 10 meV down to the resolution limit of the set-up [Kin10b]. Exactly the same phenomenon was observed in the present

work (figure 3.5). Consequently, emission lines of GaN/AlN QDs appear broadened up to the same range already in resonant excitation.

Since the sample was processed into mesa structures, it allows the investigation of identical QDs with resonant and non-resonant excitation. Figure 3.10 shows luminescence spectra obtained in µPL and CL measurements from the same mesa structure.[2] Similar discrepancies between the spectra were typically found in comparison of CL and µPL data for around 10 different mesa structures.

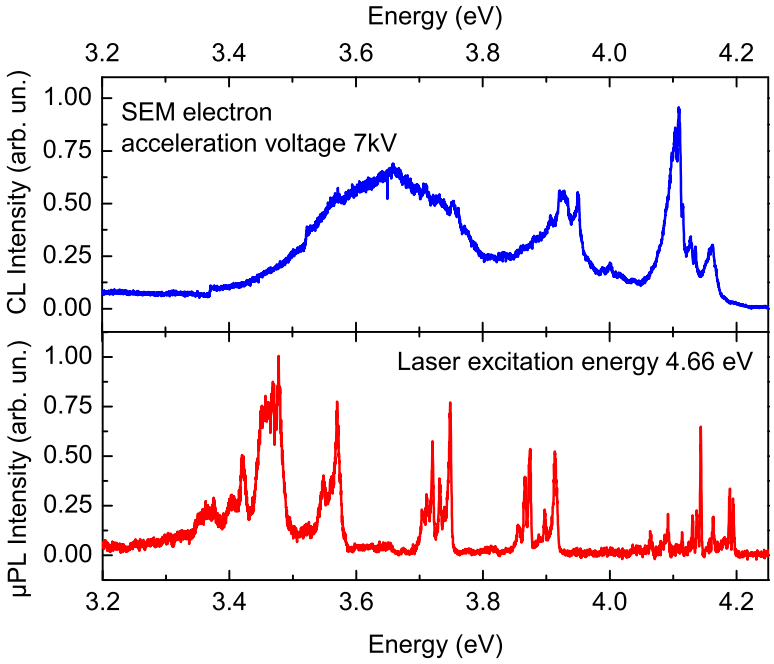

Figure 3.10: The same mesa was measured in CL(top) and µPL(bottom) experiments.

In CL individual lines of QD luminescence were observed only for emission energies above 4.0 eV. For smaller energies separate lines could not be found and a broad luminescence band was observed. In contrast, in µPL experiments it was possible to resolve single lines below 4.0 eV for the same [Kak04, Kin09, Kin10a] and similar samples [Bar06, Sim08b, Bar08]. The spectral resolution limit of those set-ups is equal to the one used in the present work. This difference is explained in terms of interaction between the excitons and acoustic phonons further down in section 4.3.3.

[2]The µPL experiments were performed in the Research Center for Advanced Science and Technology, University of Tokyo, Japan. The data were measured by Christian H. Kindel and kindly provided for the current work.

3.2.5 Discussion: defects

For a better understanding of the huge broadening of emission lines of GaN/AlN QDs and, possibly, of growth optimization in order to reduce FWHMs it is important to be aware of the kind of defects, responsible for the broadening.

There is a large variety of defects even in high-quality bulk material: native point defects, line and planar defects and impurities. Such defects introduce additional energy levels within the band gap and can also act as non-radiative recombination centers. Typical point defects include vacancies, interstitial (additional atom incorporated onto the site, where there is usually not an atom) and anti-sites (in compound materials, where an anion occupies place of a cation or vice versa). Another type of structural defects refers to defect complexes: line defects such as edge and screw dislocations, planar defects such as stacking faults and domain boundaries. Impurities are often introduced into the material as unintentional doping. GaN-based III–nitride heterostructures are well known for their high defect concentration and problematic doping [Jai00, Van04].

As soon as a charge is captured or released in some trap (defect or localization center in the wetting layer) in the close vicinity of the QD, the local electric field changes. If each of N charge traps around a QD can remain in either state (with or without a charge), there can be at least 2^N field configurations for the QD. The number of charge traps should be large enough and the change of the overall local field should occur fast enough, to result in the broadening of emission lines up to a few meV. The charges within a distance less than 10 nm to the QD contribute most significantly to the line broadening (see figure 3.1). Then at least one charge trap in such close vicinity to the dot will result in the density of the traps at least $2{\cdot}10^{17}$ cm^{-3}.

Typically in wurtzite nitride-based materials point defects have less densities: of the order of 10^{14}-10^{15} cm^{-3} [Göt95, Yi96] and rarely can be as high as 10^{17} cm^{-3} [Jai00]. The probability that such a point defect is situated at a distance of 10 nm to the QD is quite low. Only for concentrations of $\sim 10^{17}$ cm^{-3} the lateral distance between the defects can be as low as 20 nm, resulting in approximately one defect close to the QD. Concentrations of the line defects such as threading dislocations are of the order of 10^{8}-10^{12} cm^{-2}[Jai00, Sug98, Ros97, Les95, Pon02] result in spacings between the defect lines of 1 µm-10 nm respectively. Only in case of the highest densities there can be a defect line in a distance of 10 nm to the QD. Hence, neither point defects nor defect lines can affect the line broadening up to amount of a few meV.

The values of defect concentrations reported above relate to the bulk material. However, the crystal in the close vicinity of the dot differs significantly from the bulk. Due to a lattice mismatch between the QD and embedding materials, an increased number of dislocation lines can be induced in the matrix material at a low distance to the QD layer. Besides, growth of the capping layer is performed at lowered temperatures, which leads to increased defect densities in the close vicinity of the dots in the overgrown crystal. Additionally, charge localization centers in the wetting

layer (WL) can also act as charge traps (see the evidence in figure 3.14 in the next section).

Generally speaking, the defects in the capping layer together with dislocation lines are common for any material system of self-assembled QDs and cannot be avoided during growth. Compared to e.g. arsenides or selenides, nitride-based materials exhibit still higher defect densities (both point and line defects). Together with the significant built-in dipole moment, making the GaN/AlN dots sensitive to the fluctuation in the environment, the enhanced defect density close to the dots results in large linewidths.

3.3 Long-timescale spectral diffusion

The long-timescale SD manifests itself as a variation of the spectral position and/or intensity of the QD emission line. A proper graphic visualization for it are intensity-coded plots (hereafter SD-patterns), demonstrating the time evolution of a single luminescence spectrum. A typical example is shown in figure 3.11. Each single spectrum was measured under normal excitation conditions with a detection time as short as 250 ms. Three of the spectra are extracted from the data array and shown in the right panel.

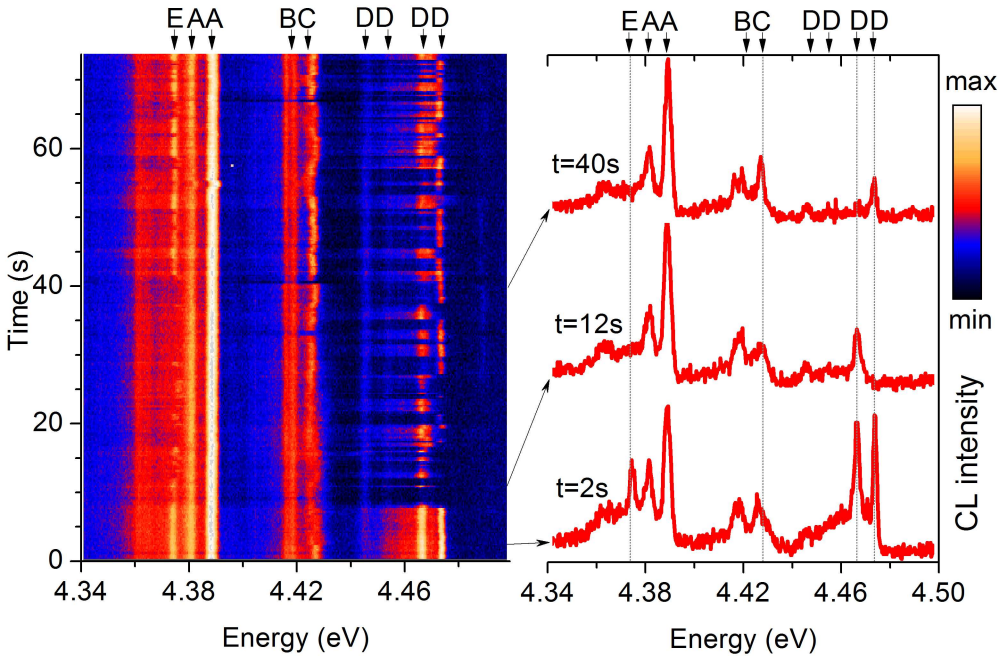

Figure 3.11: Left: Example of an SD-pattern of the emission lines from single QDs. Groups of the lines with similar SD-behavior are indicated with letters. Right: Single spectra at three times. The dashed lines help to see the variation of spectral position and the intensity of certain lines.

The two lines dubbed A are stable except for an abrupt shift at t=55 s that lasts for about 1 s. Line B does not show any variation either in spectral position or intensity. In contrast, line C continuously changes its spectral position within 2-3 meV around 4.425 eV. The four lines dubbed D are constantly blinking on and off from the moment t=7 s in synchronous tact, although no change of the excitation condition occurred. The change of spectral position and intensity for several lines can be seen in the single spectra, shown on the right panel.

For different groups of lines there is no correlation in the variation of the luminescence (called further on SD-behavior). Lines, indicated with an identical letter, show synchronous change of the spectral position or intensity. Each group exhibits its characteristic time-constants of SD-behavior: “A” shifts aside only for 1 second, and “D” turns off for a few seconds, “C” smoothly changes its spectral position.

Figure 3.11 is a good example for two types of long-timescale SD. The effect of spectral position change is usually called spectral jitter, it can be observed as continuous (like line C) or discontinuous jitter (like line A with an abrupt change of the spectral position at 55 s). Intensity intermittence or on/off blinking (see below in section 3.3.1) can be seen in the example of D, E. Detailed observations of these SD types and conclusions about the properties of the QDs are described in the following sections. A special case of spectral jitter, named χ-patterns, is treated separately in section 3.4.

3.3.1 On/off blinking

The lines dubbed D in figure 3.11 show an abrupt variation and even quenching of their intensity. Such on/off blinking was typically observed for most of the emission lines of sample T and the following observations were made for this phenomenon.

After some time of irradiation with SEM beam (usually 5-10 minutes) about 90 % of the emission lines started to disappear for a time on the order of 1-10 seconds. The “off-times” became longer with further irradiation and could be as long as several minutes, the “on-times” in contrast became shorter and could be as short as hundreds of milliseconds. This effect is reversible: after warming up the sample to room temperature and cooling it down again, the emission lines showed the same tendency: staying stable for the initial 5-10 minutes and starting to blink afterwards. Shortly after exposing the samples to light and air (when mounting the sample into the chamber), the emission lines showed enhanced on/off blinking as well. Only a small fraction (around 10 %) of the emission lines were found to be robust and did not start to blink after long irradiation.

It can be assumed that a blinking line only shows a large spectral shift of emission energy, induced by some trapped charge in the defect close to the QD. The utmost shift can be in the range of tens of meV (see figure 3.1). However, in the spectra with the emission lines in “off”-state no other “new” emission peaks were observed within 700 meV. Thus the emission line indeed shows the intensity intermittence.

In resonant µPL experiments the same sample showed on/off blinking too [Kin09]. However, blinking was reduced after annealing of the sample.[3] In contrast, such luminescence intermittence in the SD-patterns, obtained in CL experiments, was almost never observed for the GaN/AlN QDs, grown in MBE (sample L). Thus, the defect responsible for on/off blinking is most likely introduced by a certain growth procedure (it could be some hydrogen-related defect, as typical for MOCVD growth) and can be removed by means of post-processing.

Up to day there is no clear understanding what controls the luminescence intermittence of QD emission. The authors in [Pis99] ventured some defect with two metastable states, one of which acts as a non-radiative center. This defect is activated by phonons induced in a carrier recombination or a relaxation cascade in the dot (a so-called phonon-kick mechanism [Kre74]). In [Emp96, Nir96, Neu00] a mechanism based on Auger recombination is suggested. Here the energy electron-hole recombination is transferred to the rest of the charge carriers in the dot and ejects them from the dot. This appears as an "off"-state in the luminescence traces. If Auger recombination is responsible for the on/off blinking of QD emission, then in case of the self-assembled QDs this mechanism would lead to intermittence only of the emission line corresponding to a multiexcitonic complex. Here the recombination of one electron-hole pair will induce the ejection of the remaining electron-hole pairs, while in contrast the excitonic emission line (when initially only one electron-hole pair is captured in the dot) should always be present in the spectrum.

In CL experiments often several lines (up to 10) stemming from the same QD were observed. Usually all the lines would blink off at once and then reappear. In resonant µPL experiments [Kin09] several emission lines showed intermittence simultaneously. These observations exclude Auger recombination as an explanation for on/off blinking.

If, in contrast, the on/off blinking is related to the presence of a defect, then such a defect would have to have the following properties: It is introduced with larger densities during the MOCVD-growth process and can be removed by means of annealing. The defect can be in two different states, influencing the QD luminescence efficiency. In one of the states the defect either prevents capture of the charge carriers into the QD or it absorbs the photons emitted by the exciton recombination in the QD. When the defect is in this state, the QD luminescence is "off" and cannot be observed in the spectra. The defect can persist in the state for a long time (tens of seconds up to some minutes) and switch into the state after SEM beam irradiation or exposure of the sample to light or air. A large number of QDs showing on/off blinking indicates high densities of the respective defect (one defect in the close vicinity of 10 nm to every dot results in densities of the order of ~10^{17}cm^2).

DX center in AlN can be a possible defect of this kind. It was initially described in connection to AlGaAs [Cha89]. Oxygen and silicon, which are common impurities in AlN, become DX centers at high Al-concentrations (when exceeding 30 %)

[3]Not published, information kindly provided by Christian H. Kindel.

[Cha97, McC98, VdW98]. This defect configuration is found to be the reason of decrease in the conductivity of $Al_xGa_{1-x}N$ alloys for x>0.4. In GaN oxygen forms a DX center under hydrostatic pressure [Per95, Wet97]. DX center formation is accompanied by a strong relaxation of the oxygen atom off the substitutional site in [0001] direction, and the impurity acts as an acceptor. Additional Coulomb potentials in the interaction of metal atom and the impurity atom lead to a shallow level in the band gap. DX centers can be ionized by light or by thermal activation, and can be mobile within the crystal. The process of recapture to the DX state can be as slow as minutes.

The influence of the DX centers on QD luminescence intermittence is possible, although not yet fully understood. Indeed, oxygen is readily incorporated as a contaminant during nitride growth. To explain the different observations of blinking in two samples, it can be speculated that in the MOCVD sample AlN was grown with different Al-concentrations or a larger amount of oxygen was introduced during growth, or a different strain in QDs induced formation of DX centers in the GaN.

3.3.2 Spectral jitter

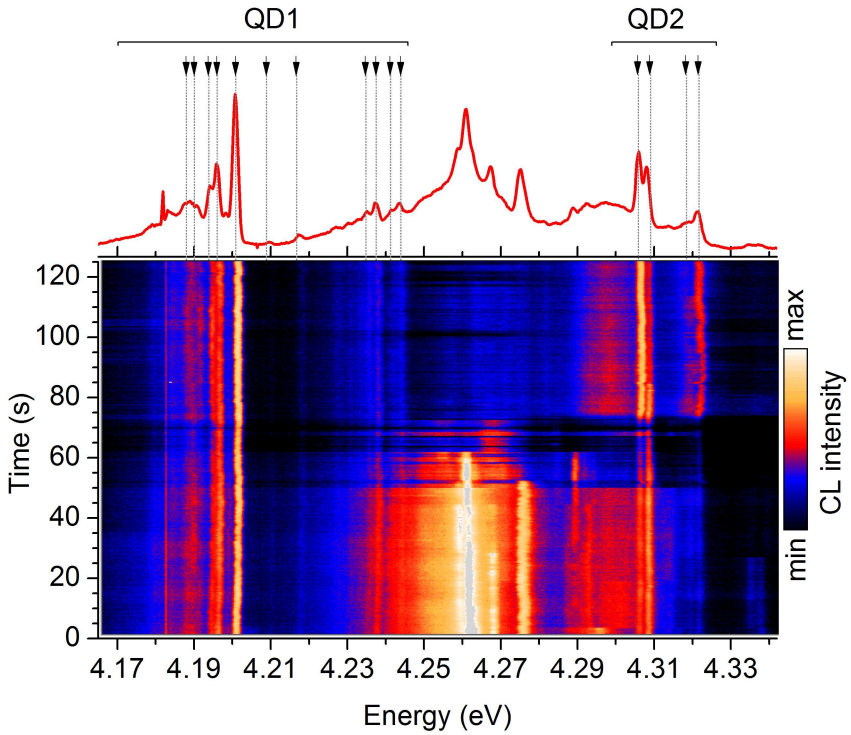

Figure 3.12: SD-pattern for a single luminescence spectra shown on the top. Two different groups of emission lines with synchronous spectral jitter within the same group can be identified.

Figure 3.12 shows an SD-pattern obtained for CL from QDs in a mesa structure with a diameter of 2 µm. Detection time for a single spectrum was 250 ms. A single spectrum is shown at the top of the figure. Ten lines, indicated with arrows under a marker QD1, show the same pattern of synchronous shifts. This pattern is different to the jitter of the four lines, indicated with arrows under a marker QD2. The rest of the lines in the spectra exhibit shifts, different to QD1 and QD2.

The identical SD-patterns of the particular emission lines in the SD-pattern can be explained as follows. Each dot is exposed to a different local electric field, caused by charges trapped in the defects in the close vicinity of the QDs. The excitonic and multi-excitonic complexes in one QD on the contrary are exposed to the same local electric field. Thus, all the emission lines originating from one and the same QD show a unique pattern of characteristic shifts of the transition energies due to QCSE. The spectral jitter is then a useful tool for the preliminary identification of emission lines, stemming from the same QD.

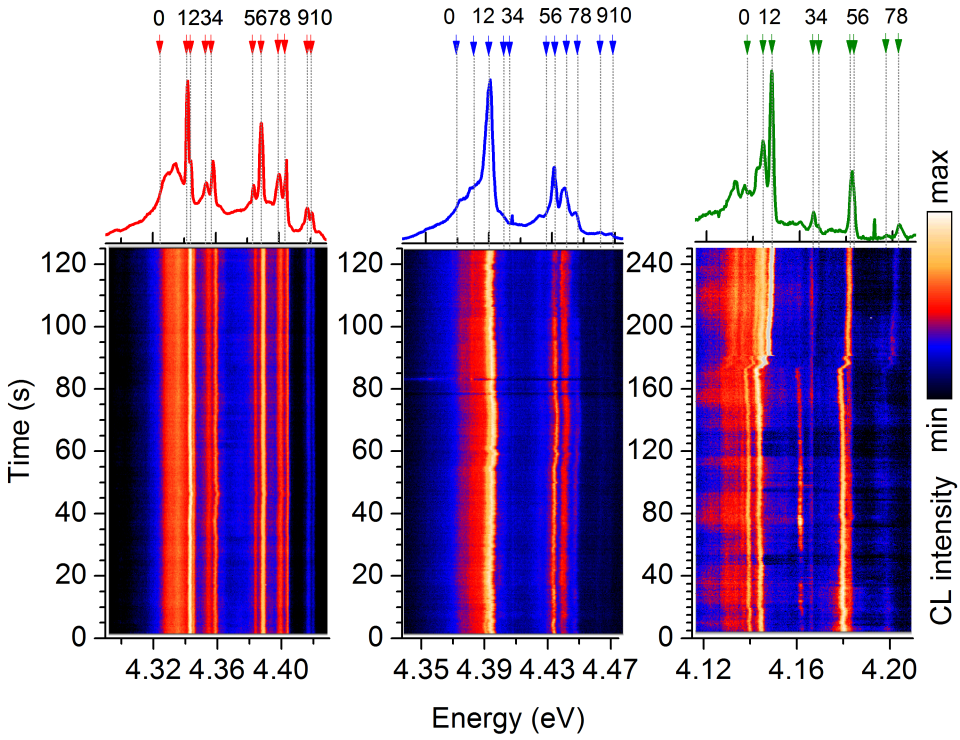

Figure 3.13: SD-patterns for three dots, showing the typical "fingerprint" of the luminescence of a single QD. The lines 0-10 within each group show similar intensity ratio to one another.

Typically up to 10 emission lines with the same jitter could be identified from the SD-patterns for single CL spectra. Comparison of these sets of the emission lines from different QDs revealed a characteristic "fingerprint" in luminescence of single GaN/AlN QD: there is a similar arrangement of emission lines appearing with a

similar ratio of the intensities of the lines. Such "fingerprint" in traces of emission lines of three different QDs is shown in figure 3.13.

Two emission lines dubbed 1 and 2 appear with an energetic separation of 1-2 meV and the highest intensity in comparison to the other emission lines. A broad band 0 always accompanies 1 and 2 on the low-energy side. On the high-energy side of peak 1 the following emission line pairs show up: 3 and 4 at 10 meV, 5 and 6 at 30 meV, 7 and 8 at 40 meV (approximate energy is given relative to the peak 1). The intensity of 5-8 is lower than of 1 or 2. Lines 3 and 4 are even weaker and not always observed (e.g. the middle panel in figure 3.13). Rarely another emission line pair 9 and 10 with the weakest intensity of all can be observed with a spectral separation of 50 meV to the peak 1.

These "fingerprints" are very helpful to verify theoretical calculations, which try to predict oscillator strengths and energies of excitonic transitions in QDs of different size, composition and geometry (see section 2.3.2). Together with excitation- and polarization-dependent measurements it is then possible to identify the excitonic complex the luminescence line stems from. This combined investigation allows deciphering the luminescence spectra, which is necessary for a proper analysis of the QD properties.

In figure 3.13 emission lines, already broadened up to a few meV, exhibit spectral shifts within 1-2 meV. SD-patterns with the shortest integration times reveal this long-timescale SD in both samples of GaN/AlN QDs (grown with MOCVD and MBE). In CL experiments spectral jitter was observed for ~ 90-95 % of the emission lines but never in resonant µPL experiments.[4] In contrast, short-timescale jitter, resulting in line broadening, was observed both in resonant and non-resonant excitation experiments in both samples. Consequently, different kinds of defects should be responsible for the two types of jitter. The long-timescale spectral, observed as (dis)continuous shifts of the broadened emission line, is present only in non-resonant excitation experiments[5] and is independent of growth approach.

CL spectra exhibited spectrally narrow lines also in the spectral range of the WL luminescence (see figure 3.14), indicating a possible 3D confinement of the charge carriers in tail states of the WL as well. Such localization centers can act as charge traps. These traps are very close to the QDs and are not activated in resonant µPL (see figure 3.9) and could be another reason for the spectral jitter of the QD emission under non-resonant excitation.

[4]The µPL experiments were performed in the University of Tokyo and kindly provided by Christian H. Kindel.

[5]For non-resonant µPL experiments on GaN/AlN QDs such spectral jitter was also reported [Bar06, Sim08b].

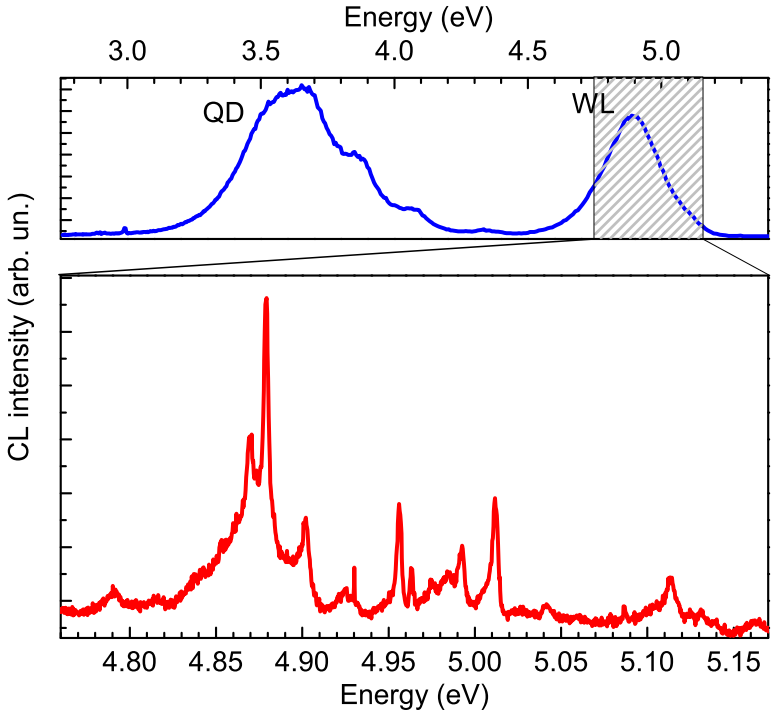

Figure 3.14: Top: Overview spectrum of the QD and WL luminescence. Bottom: Spectrally narrow emission lines, stemming from the WL.

3.3.3 Influence of the excitonic dipole moment

For GaN/AlN QDs the QCSE can be described as linear, when the local field variation is small $\triangle F \ll F_{int}$ (see section 1.3.3)

$$\Delta E(\Delta F) = E(\boldsymbol{F_{int}} + \triangle \boldsymbol{F}) - E(\boldsymbol{F_{int}})$$

$$= \boldsymbol{\mu_{built-in}} \cdot \triangle \boldsymbol{F} + \alpha \left(\triangle \boldsymbol{F}\right)^2 \approx \boldsymbol{\mu_{built-in}} \cdot \triangle \boldsymbol{F} \tag{3.3}$$

Here $\boldsymbol{\mu_{built-in}}$ is the so-called field-induced excitonic dipole moment

$$\boldsymbol{\mu_{built-in}} = \boldsymbol{\mu_0} + 2\alpha \boldsymbol{F_{int}}$$

Due to huge values of the built-in field F_{int} the intrinsic dipole moment of the dot $\boldsymbol{\mu_0} \ll 2\alpha \boldsymbol{F_{int}}$ and $\boldsymbol{\mu_{built-in}}$ indicates the spatial separation of the center of mass of the electron and the hole wave-functions, induced by $\boldsymbol{F_{int}}$. In analogy to electrostatics the built-in dipole moment is often described as $\boldsymbol{\mu_{built-in}} = e\boldsymbol{l}$, where $\boldsymbol{l}$ is a vector pointing from the electron to the hole.

The built-in dipole moment of an exciton in the dot depends not only on the polarization fields in the heterostructure $\boldsymbol{F_{int}}$, but also on the morphology of the dot. Shape, size and composition of the dot influence the spatial distribution of the electron and the hole wave-functions, resulting in characteristic values of built-in dipole

moments $\boldsymbol{\mu_{built-in}}$ for different dots. For the different excitonic complexes in the same dot the distributions of the electron and the hole wave-functions are not equal. Therefore, the electric dipole moments of various excitonic complexes in the same QD differ from each other.

For a multiexcitonic complex, consisting of n electrons and p holes, at recombination of one electron-hole pair a photon is emitted and $(n-1)$ electrons together with $(p-1)$ holes remain in the dot. When an electric field is applied to the dot, the transition energy $E^{n,p}$ changes according to the formula (1.8) derived in section 1.3.3, when neglecting the quadratic term of QCSE:

$$\Delta E^{n,p}(\Delta F) = E^{n,p}(\boldsymbol{F_{int}} + \triangle \boldsymbol{F}) - E^{n,p}(\boldsymbol{F_{int}})$$

$$\approx \left(\boldsymbol{D^{n,p}_{built-in}} - \boldsymbol{D^{n-1,p-1}_{built-in}}\right) \cdot \triangle \boldsymbol{F} = \boldsymbol{\mu^{n,p}_{built-in}} \cdot \triangle \boldsymbol{F} \tag{3.4}$$

Here $\boldsymbol{D^{n,p}_{built-in}}$ is the electric dipole moment of the charge distribution in a QD, filled with n electrons and p holes. In analogy to equation (3.3) an effective dipole moment $\boldsymbol{\mu^{n,p}_{built-in}} = \boldsymbol{D^{n,p}_{built-in}} - \boldsymbol{D^{n-1,p-1}_{built-in}}$ is introduced and, to simplify matters, is named below the built-in dipole moment of the multiexcitonic complex. In particular, for the exciton it is equal to the electric dipole moment of the exciton:

$$\boldsymbol{\mu^{1,1}_{built-in}} = \boldsymbol{D^{1,1}_{built-in}} - \boldsymbol{D^{0,0}_{built-in}} = \boldsymbol{D^{1,1}_{built-in}} = \boldsymbol{\mu_{built-in}}$$

If the temporal change of the energy of a particular excitonic transition is known for several excitonic complexes in the same QD, the ratio of the built-in dipole moments for these excitonic complexes can be calculated.

Let $E(t)$ be the emission energy of some excitonic transition X_i with effective dipole moment $\mu^{Xi}_{built-in}$ at moment t. $E(t)$ is measured in the luminescence spectra and is influenced by the local electric field at this moment $\triangle \boldsymbol{F}_t$. With regard for equation (3.4):

$$\triangle E(t) = E(t1) - E(t2) = E(\triangle \boldsymbol{F}_{t1}) - E(\triangle \boldsymbol{F}_{t2}) \pm E(\triangle \boldsymbol{F} = 0)$$

$$= \Delta E(\triangle \boldsymbol{F}_{t1}) - \Delta E(\triangle \boldsymbol{F}_{t2}) = \boldsymbol{\mu^{Xi}_{built-in}} \cdot (\triangle \boldsymbol{F}_{t1} - \triangle \boldsymbol{F}_{t2})$$

For the different excitonic complexes X_i and X_j (e.g. X, XX, X^- etc) from the same QD i.e. under the same local electric field

$$\frac{\triangle E^{Xi}(t)}{\triangle E^{Xj}(t)} = \frac{\boldsymbol{\mu^{Xi}_{built-in}} \cdot (\triangle \boldsymbol{F}_{t1} - \triangle \boldsymbol{F}_{t2})}{\boldsymbol{\mu^{Xj}_{built-in}} \cdot (\triangle \boldsymbol{F}_{t1} - \triangle \boldsymbol{F}_{t2})} = \mu^{Xi}_{built-in} : \mu^{Xj}_{built-in} \tag{3.5}$$

Therefore, the spectral jitter allows to determine the ratio of the built-in dipole moments of different excitonic complexes from the same dot. The ratio can be obtained from SD-patterns (e.g. figure 3.12), when equation (3.5) is applied to the emission lines, showing the same jitter pattern. One example is shown in figure 3.15.

The right panel of the figure shows the SD-pattern of a QD (which also displayed on the left panel in figure 3.13). For the emission lines, labeled as L1, L4, L6 the energetic positions are defined for a number of times t. For each line difference $\triangle E^{Li}(t) = E^{Li}(t) - E^{Li}(t = 0)$ is calculated. For the selected times the pairs $\left(\triangle E^{Li}(t), \triangle E^{Lj}(t)\right)$ are depicted for the pairs $i, j = (1, 2); (1, 3); (3, 2)$ in the left panel of figure 3.15. According to equation (3.5), the slope of the linear fit to the data points of a certain emission line pair gives the ratio of the built-in dipole moments of the respective excitonic complexes. The coefficients of the slopes, resulting from the linear fit of the data, are shown in the figure.

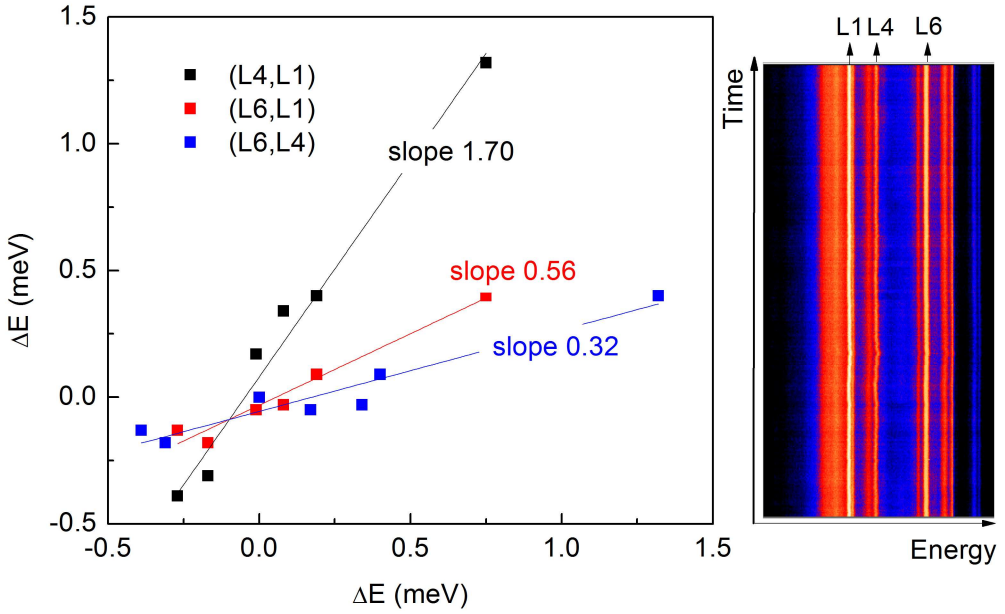

Figure 3.15: Left: Data points depict the relative energetic shifts for pairs of lines (L4, L1), (L6, L1) and (L6, L4). Solid lines show the linear fit of the data. The resulting slope is marked directly in the plot. The data are extracted from the SD-pattern (right), where the lines are indicated.

The same procedure was performed for four QDs for a number of emission lines with sufficient SNR. The energetic shifts of the emission lines in CL experiments $\triangle E^{Li}(t)$ were observed to be less than 2 meV, and rarely (in less than 5 % of the cases) larger - up to 2-6 meV (one example is displayed in the middle panel of figure 3.13). The ratios $\mu^{Xi}_{built-in} : \mu^{Xj}_{built-in}$, obtained from the linear fits of the data sets, are listed in table 3.1 as a slope and are printed in bold type. Errors are the standard errors of the linear fit to the data. The line numbering is in correspondence to the luminescence fingerprint, indicated in figure 3.13.

The values of $\mu^{Xi}_{built-in} : \mu^{Xj}_{built-in}$ range between 0.3 and 1.7, indicating a significant difference of the built-in dipole moments of the excitonic complexes. Moreover, the same line pairs from different QDs show similar ratio value.

Table 3.1: Values obtained from the linear fits of the data sets for four QDs. For line names see QD luminescence fingerprint in figure 3.13.

	QD1	QD1	QD1	QD2	QD3	QD3	QD3	QD4
Line pair	4,1	6,1	6,4	6,1	4,1	7,1	7,4	6,1
Emission energy of line 1	4.34 eV			4.31 eV	4.23 eV			4.14 eV
Slope	**1.7**	**0.56**	**0.32**	**1.0**	**1.2**	**0.7**	**1.7**	**0.60**
Error	0.1	0.05	0.04	0.4	0.7	0.3	0.6	0.08

The difference of the built-in dipole moments of the different excitonic complexes from the same QD influences in the same way both long- and short-timescale SD. Comparing formula (3.2) for Γ_{SD} with equation (3.5)

$$FWHM_{Xi} : FWHM_{Xj} = \mu^{Xi}_{built-in} : \mu^{Xj}_{built-in}$$

The emission lines from the same QD did exhibit different linewidths, which is another evidence for a significant variation of the built-in dipole moments of excitonic complexes of the same QD. The ratio $\mu^{Xi}_{built-in} : \mu^{Xj}_{built-in}$ was not obtained from the FWHMs in this work, since overlapping of some lines or low SNR prevented precise data processing.

The ratio $\mu^{Xi}_{built-in} : \mu^{Xj}_{built-in}$ was calculated for several excitonic complexes theoretically. 8-band $\mathbf{k} \cdot \mathbf{p}$ calculations in combination with the Hartree-Fock method (see section 2.3.2) were performed for a model QD in the shape of a truncated pyramid with a height of 1.2 nm, a base length of 6.0 nm, and an elongation of 20 %. The exciton emission energy is predicted to be 4.25 eV. For X, X^+, X^-, XX and XX^- the obtained values are listed in table 3.2.

Theoretical calculations also show difference of $\mu^{Xi}_{built-in}$ for different Xi from the same QD. Excitonic complexes with a fewer number of confined charge carriers have smaller dipole moments compared to the exciton. Consequently, multiexcitonic complexes are less sensitive to the changes of the local electric field, as additional charge carriers screen the external field more efficient.

Also, $\mu^{XX}_{built-in} : \mu^{X}_{built-in}$ was calculated for a series of model QDs with varying size and constant aspect ratio. The dependence of the ratio on the QD size (or, the same, on the emission energy), is shown in table 3.3. An increase of $\mu^{XX}_{built-in} : \mu^{X}_{built-in}$ can be noted with the increase of the $\mu^{X}_{built-in}$. For the largest dots $\mu^{XX}_{built-in} \approx \mu^{X}_{built-in}$ and the changes of the local electric field is not screened for the multiexcitonic complexes as effectively, as in small QDs.

The experimental values of $\mu^{Xi}_{built-in} : \mu^{Xj}_{built-in}$ (range between 0.3 and 1.7) show

Table 3.2: Calculated values of the built-in dipole moment ratios for different excitonic complexes in a model QD. Accuracy of the values is 0.01.

Xi, Xj	XX^- , X	XX, X	X^- , X	X^+ , X
$\mu^{Xi}_{built-in}$: $\mu^{Xj}_{built-in}$	0.84	0.90	0.93	0.93

Table 3.3: Calculated values of $\mu^{XX}_{built-in} : \mu^{X}_{built-in}$ for a series of model QDs with varied sizes. Accuracy of the values is 0.01.

Exciton emission energy	4.79 eV	4.25 eV	4.03 eV	3.90 eV	3.56 eV
$\mu^{XX}_{built-in}$: $\mu^{X}_{built-in}$	0.83	0.90	0.91	0.91	0.95

a larger difference between the built-in dipole moments of different excitonic complexes, than the calculated ones (0.84-1.1, here the largest value is $\mu^{X^+}_{built-in} : \mu^{XX^-}_{built-in}$). This discrepancy can be attributed to the form of the QDs. Real QD shape deviates significantly from a perfect hexagonal (see e.g. AFM investigations of uncapped samples in [Kin09]) assumed in the calculations, and can influence significantly the distribution of the electron-hole wave-functions.

Nevertheless, qualitative trends revealed in the calculations are helpful for interpretation of the experimental data. Comparison of the built-in dipole moments ratios for different emission lines, obtained either from spectral jitter or linewidths, can be helpful in identification of the line origin.

3.3.4 Influence of the excitation conditions

For the quantitative investigation of the dependence of the long-timescale SD on the excitation densities, SD-patterns consisting of the sequences with a large number of single spectra should be measured under various excitation conditions. Thus information on e.g. the dependence of the amplitude of the spectral jitter for the same emission line on e.g. the electron beam current could be obtained. However, such data collection demands long SEM beam irradiation times of the QD under investigation. In addition to this measurement duration some time is needed for readjusting the SEM after changing the electron beam parameters. As described in section 3.3.1, after 5-10 minutes most of the lines started to blink off for long periods, preventing further collection of data. The data obtained were not sufficient for a quantitative analysis.

Within the varied range of the excitation density (same as in section 3.2.2) no qualitative difference for one and the same dot could be observed. A more significant difference was observed in the SD-behavior of different QDs. The amplitudes of the spectral shifts or off-times during the blinking were found to be very specific for every particular dot. Hence, for the GaN/AlN QD material system local densities of defects or charge traps, which lead to a long-timescale SD, are inhomogeneous in the crystal close to the QD layer.

3.4 Dipole-moment-induced oscillations of emission energies

Figure 3.16 shows a SD-pattern for InGaN/GaN QDs (sample B). Integration time per single spectrum was 200 ms. The acceleration voltage was set to 7 kV and the electron beam current was 5 nA. White rectangles mark a number of oscillations of the QD emission lines, typically observed for this sample. This specific spectral jitter with amplitudes of the energy shift of up to 4 meV occurred repeatedly for almost each emission line. The oscillations are uncorrelated for most of the lines. However, some lines show the oscillations at the same moment, thus indicating that they originate from the same QD. This spectral jitter always appears in the same manner: the line bends to lower energies, then blinks off and reappears with a blue shift, returning to its previous position afterwards. In the following these oscillations will be called χ-pattern. Such a regular line trajectory has not been reported before.

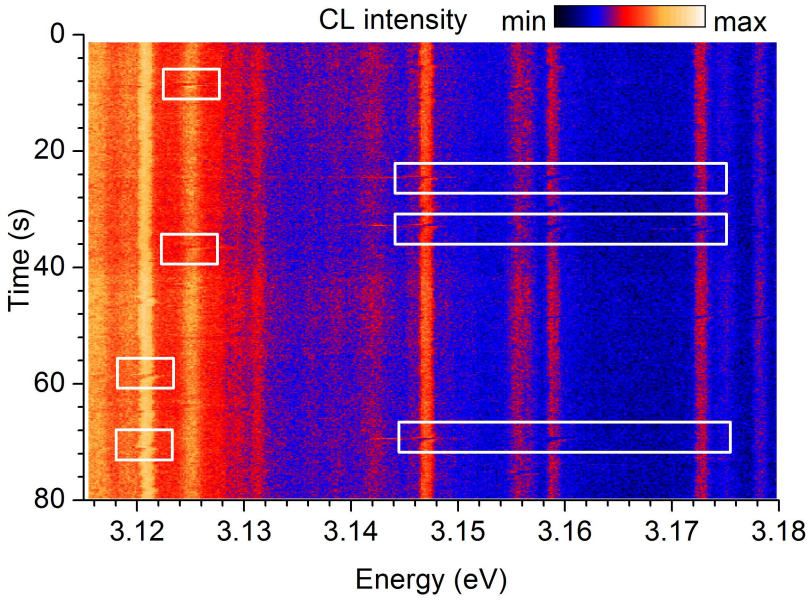

Figure 3.16: Experimental observation of χ-patterns in luminescence traces of InGaN/GaN QDs.

Any point charges on the sample surface or the GaN/AlGaN interface do not induce electric fields in the QD layer, sufficient for the observed energetic shifts. Also, variation of the capping layer thickness did not influence the SD in the sample [Rod06]. The surface states can be ruled out as the reason for the χ-patterns. Random charging and discharging of defects cannot explain the patterns either, since stochastic carrier trap and release processes cannot result in exactly the same geometry for emission lines of different dots.

3.4.1 Model of a moving charge

The charge carriers, confined in the dot, experience the influence of the overall electric field $\boldsymbol{F} = \boldsymbol{F_{int}} + \triangle\boldsymbol{F}$, where $\triangle\boldsymbol{F}$ is a variation of the local field in addition to the built-in field $\boldsymbol{F_{int}}$. For the occurrence of the χ-pattern the following conditions must be fulfilled for $\triangle\boldsymbol{F}$.

(i) The peak position changes continuously and smoothly: the $\triangle\boldsymbol{F}$ changes gradually.

(ii) The change of the $\triangle\boldsymbol{F}$ accounts for both positive and negative energy shifts of equal magnitude around the mean emission energy. This cannot be explained by a quadratic response of the system to the changes of a local electric field $\triangle\boldsymbol{F}$ and consequently $\boldsymbol{\mu}_{built-in} \cdot \triangle\boldsymbol{F} \gg \alpha \cdot (\triangle\boldsymbol{F})^2$ in QCSE. Hence, the observed patterns constitute direct experimental evidence of the large dipole moment in InGaN/GaN QDs.

(iii) The shift of the line changes its sign abruptly relative to the mean position of the line: the projection $\triangle\boldsymbol{F}$ on the direction of the built-in dipole moment changes its sign exactly once.

The following model is proposed to describe the χ-pattern. A charge q that moves through the material approximately on a straight line with a speed $\mathbf{v}$ is assumed. More complex charge trajectories are considered in section 3.4.5. The central symmetry of the χ-pattern with the same amplitude in positive and negative shift directions is only achieved when the propagation direction has a component (anti-)parallel to $\boldsymbol{\mu_{built-in}}$. The field created by a moving charge fulfills all three conditions described above.

The electric field induced at the position of the QD and the resulting time-dependent line shift can be easily estimated. A point charge q creates a field $\boldsymbol{F^q}$ at the position $\boldsymbol{r(t)}$ relative to the charge (Coulomb's law):

$$\boldsymbol{F^q}(t) = \frac{1}{4\pi\varepsilon_0\varepsilon_r}\frac{q}{r^2}\frac{\boldsymbol{r(t)}}{r} \tag{3.6}$$

If the charge trajectory is located at the lateral distance $d_\perp$ to the center of the QD and the charge passes the center at time $t = 0$ (see schema on figure 3.17),

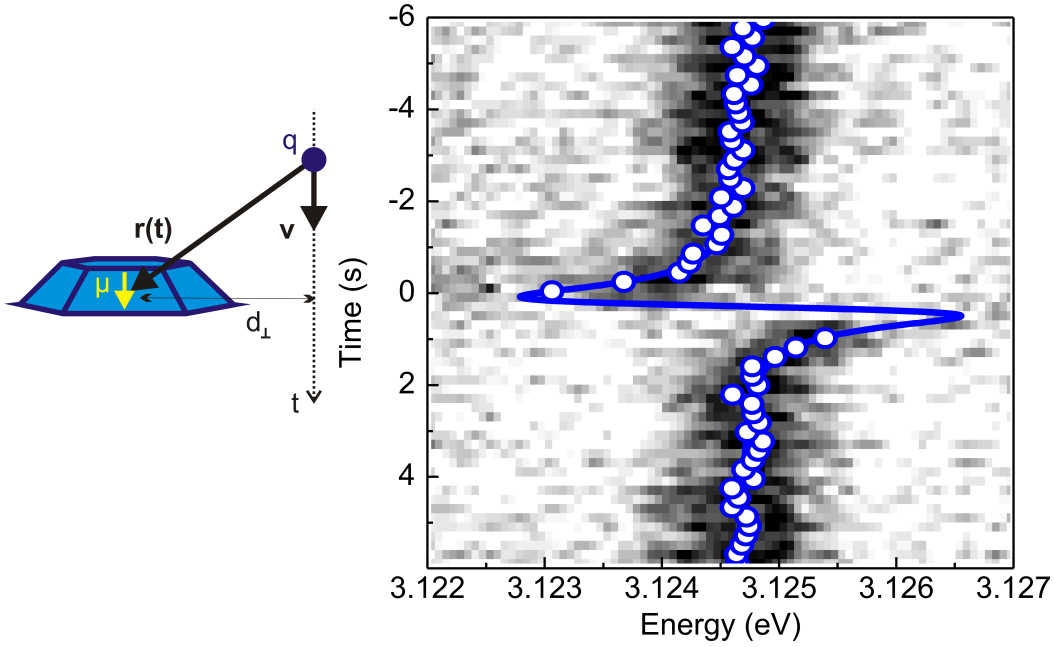

Figure 3.17: Fit of the experimental data with equation (3.7). Left: Schema of the charge q, moving with velocity **v** on a straight line parallel to the growth direction in the distance $d_\perp$ to the center of the QD.

the induced oscillation of the emission energy around its average energetic position, when taking into account QCSE - equation (3.1):

$$\triangle E(\triangle \boldsymbol{F} = \boldsymbol{F^q(t)}) \approx \boldsymbol{\mu}_{built-in} \cdot \boldsymbol{F^q(t)} = \mu_{built-in} \frac{qtv}{(d_\perp^2 + t^2 v^2)^{3/2}} \tag{3.7}$$

Figure 3.17 shows an SD-pattern of a single emission line from an InGaN/GaN QD as an intensity-coded plot in the gray scale. The integration time for each spectrum was 100 ms. Circles result from Gaussian fits for the peak center energy; the solid curve from a fit of the peak centers with equation (3.7).

The identical geometry of all χ-patterns allows to conclude that the originator is only one type of charge carrier, or that the motion of positive and negative charges occurs in exactly opposite directions. The slow time scale of the emission line shifts is remarkable: fits of experimental data with equation (3.7) (see figure 3.17) result in a charge carrier velocity in the order of ~ 20 nm/s. Such values do not comply with carrier diffusion velocities of hot carriers. Moreover, a free charge carrier in the crystal is unlikely to have a regular trajectory of a straight line.

Possible explanations can be proposed for the origin of the charge motion: (i) a weakly bound charge, propagating slowly along a defect line, e.g. a threading dislocation line; (ii) a charged mobile defect or impurity traveling along a close-to-straight

line (similar to the DX center, mentioned in section 3.3.1) under SEM irradiation. Indeed, p-type conduction of Mg-doped GaN was first achieved by low-energy electron beam irradiation [Ama89]. In a similar way the movement of some impurity atoms can be promoted via SEM beam irradiation in an InGaN/GaN heterostructure. Frequent occurrence of χ-patterns for a majority of the emission lines indicates either a high density of the defect lines or a high number of possible trajectories for the movement of an impurity/mobile defect close to the QD layer.

3.4.2 Modeling of the energetic shift

Self-consistent Hartree calculations, based on 8-band $\mathbf{k} \cdot \mathbf{p}$ theory states ([Win06], section 2.3.2), for an exciton trapped in a lens-shaped QD were performed. The lateral diameter of the model QD presented here is 5.2 nm and its height is 2 nm. The QD is placed in a 2 nm thick $In_{0.1}Ga_{0.9}N$ layer, with the In-content inside the QD linearly raising up to a maximum of $In_{0.49}Ga_{0.51}N$ at the center of the QD. This model system is embedded in a matrix of pure GaN. The lens shape and the changing In-content were chosen to better represent of the structural investigations of the sample (section 2.4), showing the inhomogeneous fluctuations of In in the InGaN layer. The size of the model dot matches the spatial dimensions of the In-content fluctuations. The predicted exciton emission energy is approximately 2.92 eV.

Similar calculations for InGaN/GaN QDs result in the strengths of the built-in field in the dot center of up to 1.6 MV/cm [Sai02, Wil04] and a significant permanent dipole moment [Win06]. The dipole moment, calculated in the present work from the electron and hole wave-functions distribution, is $\mu_z = 1.9 \cdot 10^{-28}\,\mathrm{C} \cdot \mathrm{m} = 1.2\,\mathrm{e} \cdot \mathrm{nm}$ and $\mu_{x,y} = 0$. Here the z-direction is parallel to the direction of the built-in field $\boldsymbol{F_{int}}$, x and y - are the in-plane directions of a QD. Now the influence of additional electric fields and nearby charges on the exciton emission energy can be investigated in detail.

The fields with a magnitude of $\triangle F \sim 10$ kV/cm would result in energy shifts of the same order, as observed in the experiment (see figure 3.17) and $\triangle F \ll F_{int}$. To verify, whether such fields change the distribution of the charge carrier wave-functions, a homogeneous capacitor-like field in x, y and z direction with a magnitude of $\sim$ 10 kV/cm was applied to the QD structure. This did not result in significant changes of μ.

Generally speaking, it is not obvious to what extent the QCSE is applicable to electric fields that are spatially inhomogeneous across the QD, e.g to the electric fields of a point charge. To verify the model of a traveling charge, the exciton energy shifts were obtained as follows: A negative elementary point charge was placed at different positions close to the model QDs. For each site of the charge the energy of the exciton in the model QD in the additional external electrostatic

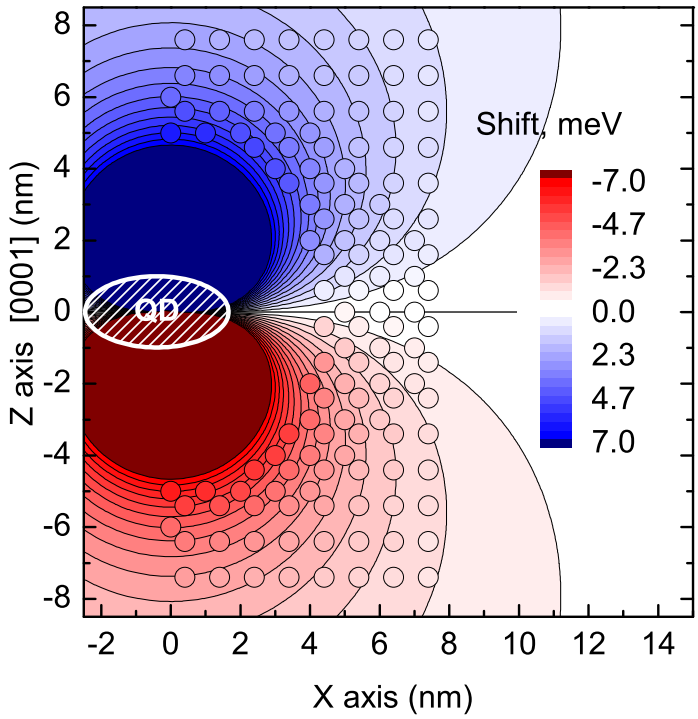

Figure 3.18: Numerical results for the excitonic shifts of the model QD, when a point charge is placed at different positions in the vicinity of the QD.

field of the charge was derived in 8-band $\mathbf{k} \cdot \mathbf{p}$ calculations in combination with the Hartree approach.

The resulting shift of the exciton transition energy with respect to the situation without any point charge is showed in figure 3.18. The shifts were calculated for the positions of the point charge, depicted with circles. The contour plot shows a fit with the QCSE formula $\Delta E(\triangle \boldsymbol{F}) = \boldsymbol{\mu} \cdot \triangle \boldsymbol{F} + \alpha(\triangle \boldsymbol{F})^2$ resulting in the same values of μ as without any charges ($\mu_z = 1.2\,\mathrm{e} \cdot \mathrm{nm}$ and $\mu_{x,y} = 0$) and $\alpha \approx 0$. Figure 3.19 shows line traces for different constant lateral distances of the point charge to the QD. The similarity to the experimental data (figure 3.17) is obvious. For the positions of the charge, very close to the dot, no numerical data were obtained due to convergence problems.

To sum up, the theoretical calculation showed that a point charge in the vicinity of the QD induces electric fields, more than 2 orders of magnitude smaller than the built-in fields in the QDs and does not change the values of the μ and α. For these fields the energy shift can indeed be described by $\Delta E(\triangle \boldsymbol{F}) = \boldsymbol{\mu} \cdot \triangle \boldsymbol{F}$: The quadratic term in the expression of the QCSE is much smaller than the one caused by the linear term, and it is justified to set the quadratic term to zero in the analysis of the experimental results.

In CL excitation a large number of free charge carriers are created in the crystal already at 5 K. The electrostatic screening effects, which were not included into

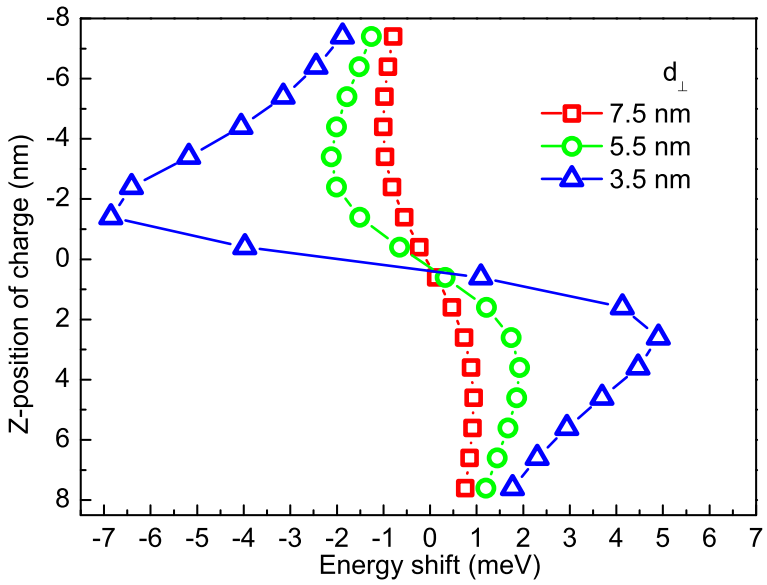

Figure 3.19: Calculation of the energetic shift of an exciton emission line in dependence on point charge position.

the calculations, can become significant. For the free charge carrier concentrations, generated under normal excitation conditions, are $n \approx 10^{15} - 10^{16}\,\mathrm{cm}^{-3}$ and the Debye length in GaN is respectively:

$$\lambda_D = \sqrt{\frac{\varepsilon_0 \varepsilon_r kT}{e^2 n}} \approx 15 - 5\,\mathrm{nm}$$

Considering the electrostatic screening in the Debye approximation, the magnitude of the field of a point charge should be estimated from the following expression instead of equation (3.6):

$$F^q_{scr} = F^q \left(1 + \frac{r}{\lambda_D}\right) \exp\left(-\frac{r}{\lambda_D}\right)$$

Figure 3.20 shows the energetic shifts with respective corrections for screening. The results do not change qualitatively. For higher concentrations of free charge carriers ($\lambda_D = 5\,\mathrm{nm}$) the χ-pattern shrinks in the amplitudes of the shifts, and for lower n ($\lambda_D = 15\,\mathrm{nm}$) the screening can be neglected.

3.4.3 Estimation of the dipole moment from experiment

Very often oscillations of the same emission lines were observed with different overall shift amplitudes. In correspondence to the model, describing the pattern: see equation (3.7), different variations of $\triangle E$ can result from different charge velocity v, different charge value q or different distances between the charge trajectory and

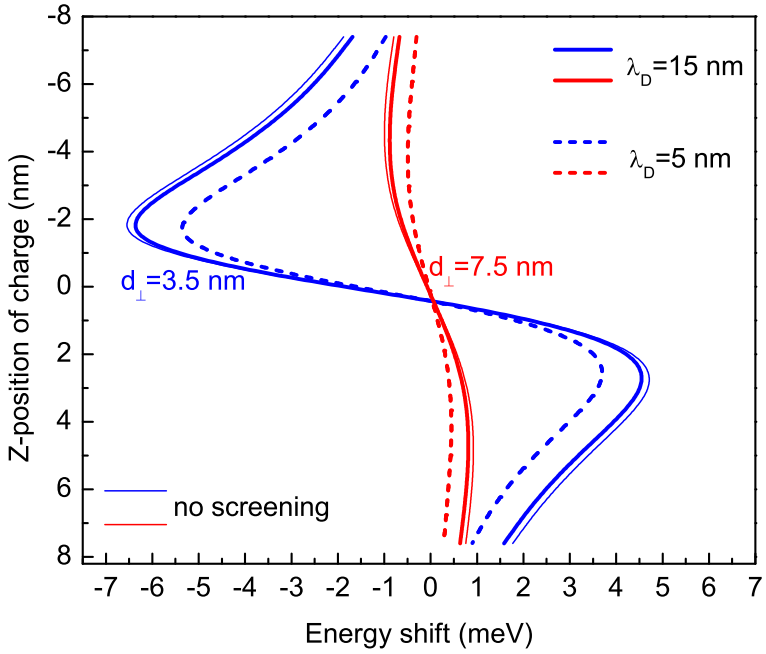

Figure 3.20: Energetic shift of an exciton emission line in dependence on point charge position with account for electrostatic screening. Results for two charge trajectories are shown. Solid thick lines correspond to $\lambda_D = 15\,\mathrm{nm}$ and dashed lines to $\lambda_D = 5\,\mathrm{nm}$. Thin solid lines show the data without Debye screening (figure 3.19).

the QD center $d_\perp$. Different q is unlikely with regard to proposed origins of the charge movement (see section 3.4.1): (i) the same charge should always travel along the same defect line or (ii) propagation of the same type of impurity, hence, same q, should be promoted by electron beam. It is therefore correct to assume the existence of several charge trajectories with various $d_\perp$ in the vicinity of a dot, resulting in different amplitudes of the oscillations of the emission line.

Now the value of the excitonic dipole moment can be directly deduced from the amplitude of the χ-pattern. The structural investigations of the sample (see section 2.4) show the average QD radius, and the average distance between the QDs is 2.5 and 10 nm respectively. Then with $d_\perp$ in the range of 2.5 to 8 nm and a maximum observed shift amplitude of 4 meV, dipole moment values between $\mu_{built-in} = 0.7 \cdot 10^{-28}\,\mathrm{C \cdot m} = 0.3\,\mathrm{e \cdot nm}$ and $\mu_{built-in} = 7.0 \cdot 10^{-28}\,\mathrm{C \cdot m} = 3.0\,\mathrm{e \cdot nm}$ respectively are obtained from equation (3.7). Theoretical predictions [Win06] and these numerical results agree quantitatively very well. Observations of χ-patterns allow to estimate the magnitude of the excitonic dipole moment of the investigated InGaN/GaN QDs in growth direction.

Figure 3.17 illustrates very well, how the intensity of the emission line decreases when the emission line bends from its average position and even blinks off in the center of the χ-pattern. The electric field of the traveling charge does not only lead

to the energy shift, but also to the reduced overlap of the electron and the hole wave-functions. The resulting reduction of the oscillator strength is observed in the experiment as a drop in the luminescence intensity.

The decrease of the emission line intensity limits the estimation of $\mu_{built-in}$: the emission line with the maximum shift can appear with a too low SNR. Then the amplitudes of the emission line oscillation, and consequently $\mu_{built-in}$, would be underestimated. Thus, the measurement time is very important for the estimation of $\mu_{built-in}$. Very long detection times do not allow for observation of the emission line oscillations. Very short integration times can result in underestimated $\mu_{built-in}$.

The emission lines stemming from the same QD show the χ-patterns simultaneously. Then the values of $\mu_{built-in}$, obtained for different emission lines from these patterns, can become a tool for the identification of the respective excitonic complex. On the other hand, if the origin of the lines is defined by additional experiments (e.g. excitation- or polarization-dependent measurements), the values of $\mu_{built-in}$ are useful to verify the theoretical calculations of the built-in dipole moments of various excitonic complexes for the QDs.

3.4.4 Observation in other samples

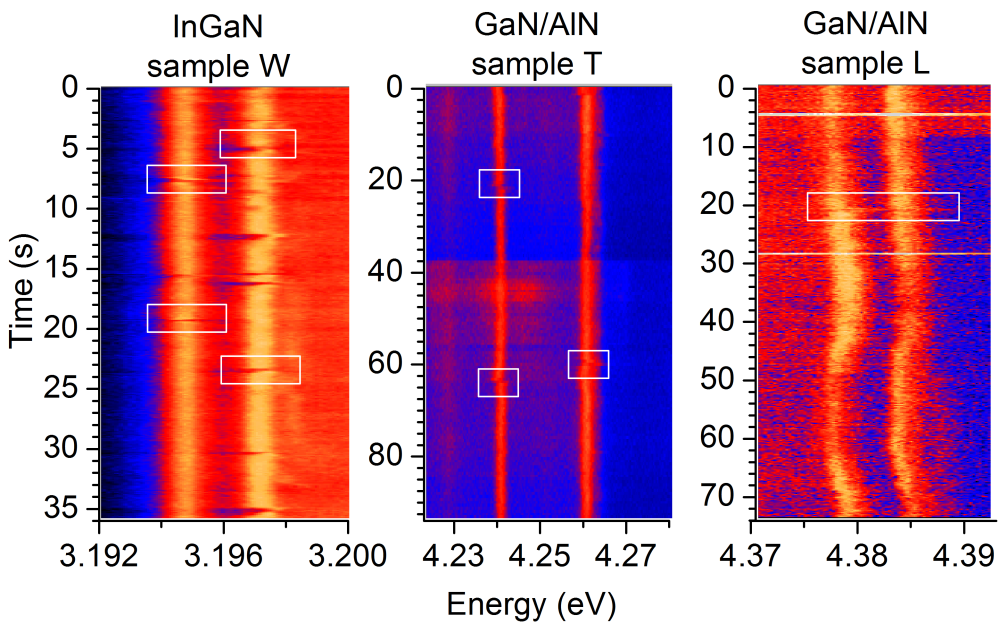

Figure 3.21: Experimental observation of χ-patterns in luminescence traces of QDs in other nitride-based samples. Some of the occurrences of the χ-patterns are marked with white rectangles.

The χ-pattern was originally observed in the emission line traces of InGaN/GaN QDs in sample B (MOCVD growth, In-concentration fluctuations in InGaN layer). Such

phenomena should also take place in other QD samples, as long as two conditions are fulfilled: (i) QDs possess large built-in dipole moments and (ii) there are similar defects in the sample, which allow for "slowly traveling charges" along the direction of the built-in polarization field.

Figure 3.21 shows the appearance of such χ-pattern in three other nitride-based samples: InGaN QDs (W, MBE growth on miscut substrates), GaN/AlN QDs (L and T: Stranski-Krastanow QDs grown in MBE and MOCVD respectively). Two emission lines of the sample L show oscillations simultaneously. For both samples with InGaN QDs the oscillations of the emission lines were observed at comparable rates. In contrast, very few χ-patterns were found for GaN/AlN QDs: χ-patterns could be identified only for three QDs in sample L and three QDs in sample T. Further statistics on χ-pattern geometries and their features for GaN/AlN are not available. Even for luminescence spectra of such QDs, measured with 50 ms integration time and acceptable SNR, the χ-patterns in GaN/AlN QDs were not observed as often as in InGaN/GaN.

A smaller number of possible trajectories of the charge movement, or in other words smaller densities of the responsible defects, can explain fewer χ-occurrences in GaN/AlN samples. If in addition, the velocity of the moving charge is too fast for this material system, the χ-patterns do appear, but cannot be measured, as the integration times are too long.

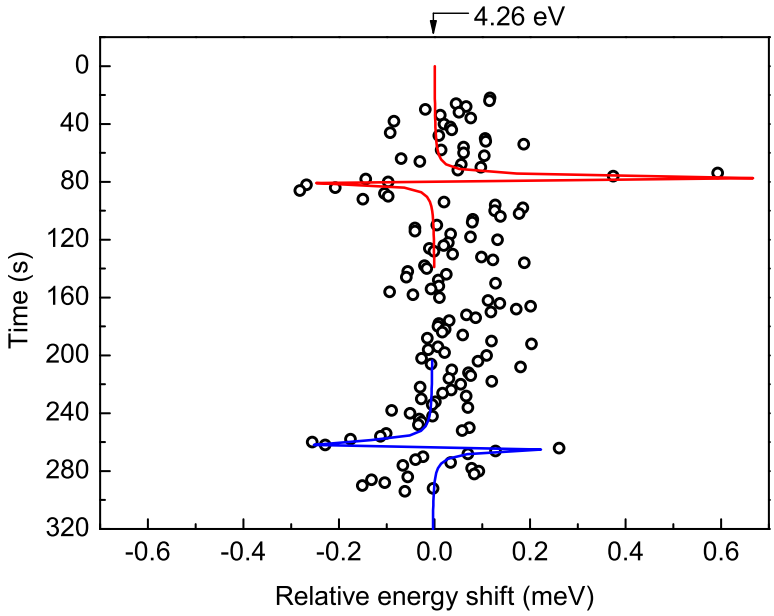

Figure 3.22: Two χ-patterns of inverse geometry as observed for GaN/AlN sample (T).

Figure 3.22 shows two χ-patterns, observed for an emission line of GaN/AlN dot in sample T. Remarkably, their geometries differ: in the first pattern the emission

Table 3.4: Parameters, obtained from the fit of the χ-patterns for various samples.

	sample B	**sample W**	**sample T**	**sample L**
	InGaN QDs		GaN/AlN QDs	
μ_z, e · nm	$0.3-3$	$0.1-1.0$	$0.2-2.7$	too low SNR
v_μ, $^{nm}/_{\mathrm{s}}$	$20-40$	$30-70$	$1-5$	
$max\Delta E$, meV	$1-4$	$0.2-0.7$	$0.2-1.2$	
Occurrence	for 90 % of emission lines		for 3 QDs	for 3 QDs

line bends to the higher energies first, and in the second one - to the lower energies (the same geometry as was constantly observed in InGaN/GaN in sample B: figure 3.17). Since both oscillations are observed for the same emission line, these χ-pattern results either from the motion of the charge in two opposite directions or from the motion of the charges of different signs in the same direction. Thus, there are at least two types of defects, resulting in χ-pattern in GaN/AlN QDs in the sample T (for example positively and negatively charged impurities moving in the same direction close to the dot).

The fitting procedure, described above for the InGaN/GaN QDs, was also applied to the χ-patterns, observed in the other samples. The results are summarized in table 3.4. For the sample L the SNR for the emission lines, which exhibited χ-patterns, was not sufficient for estimations. For the sample W neither mesa fabrication nor a metal mask were applied to allow single QD investigation. For the large number of luminescence lines the maximum of $\triangle E$ was hard to identify precisely and the built-in dipole moment in these samples can be underestimated (indeed, range of μ_z for sample B is larger than for T).

Calculations by 8-band $\mathbf{k}\cdot\mathbf{p}$ theory in combination with Hartree-Fock method for the GaN/AlN QDs result in values of the built-in dipole moment along the growth direction, which are in good agreement with the ones, obtained from experiment. The values of μ_z for the InGaN QDs in sample W can indeed be smaller, than in sample B. Both smaller height and size of the dot in the base result in smaller spatial separation of the electron and the hole wave-functions in the QD. The built-in polarization field can be smaller in W as well.

Velocity values of the charge carrier in GaN/AlN samples are smaller compared to InGaN QDs: see table 3.4. Thus less occurrence of the χ-pattern in GaN/AlN is due to a smaller density of the defects responsible for the oscillation of the emission line.

3.4.5 Discussion: defects

A charge, slowly moving in the growth direction, was proposed to explain the χ-patterns. In this model the trace of the QD emission energy has the shape of an S. At short distances to the charge trajectory the induced electric field can become quite large and results both in a significantly decreased intensity of the emission line. This drop in intensity is observed as the disappearance of the emission line in the very center of the χ-pattern. At smaller distances the intensity of the line is still strong enough to be observed in the experiment, and the line trace should appear as an S-shape jitter-pattern.

For different directions of charge trajectories relative to the growth direction the time-dependence of the QD emission energy can be estimated in the same way, as shown in equation (3.7). Figure 3.23 shows schematically the traces of emission energy of the QD for different charge trajectories without accounting for the emission intensity change. The right panel displays the simulation of three charge trajectories at various distances to the dot, while charges of different types (color-coded) cross the plane of the dot at different moments. In this case the emission energy exhibits a complex sequence of positions.

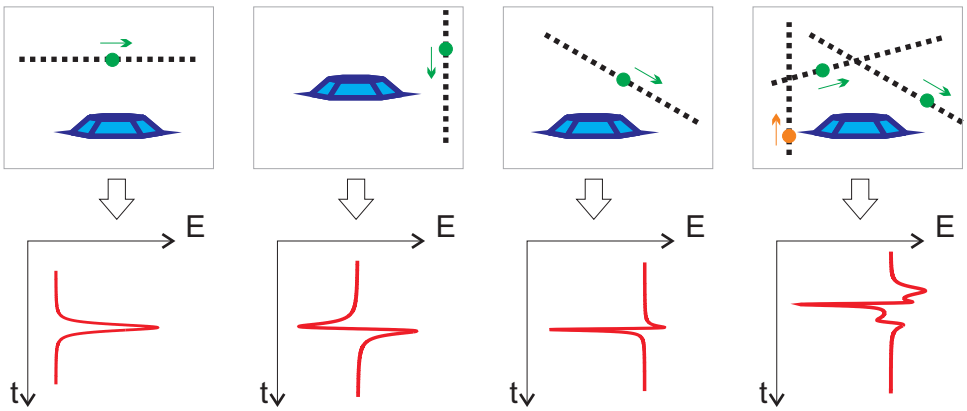

Figure 3.23: Schema of the shifts of the QD emission energy under the influence of the electric field of a charge, moving along the line, inclined at different angles to growth directions.

As can be concluded from figure 3.23, the model of a moving charge can describe any particular χ-patterns, and can also be applied to the spectral jitter in general. Both regular χ-patterns and irregular spectral jitter were observed in all the investigated samples: grown as Stranski-Krastanow QDs or as phase fluctuations in the ternary material. Therefore, mechanism underlying this type of slow SD is specific for the nitride-based QDs in general and is attributed to large built-in dipole moment, induced by pyro- and piezoelectric fields in the wurtzite-type heterostructure. Two possible explanations for the origin of the slowly moving charge (section 3.4.1) can also result in long-timescale spectral jitter. The average velocity of the charge should be very slow: in the range between a few and tens of nm/s.

SEM beam irradiation can induce propagation of some charged impurities or mobile defects in the direction close to the growth, such defects can easily change their trajectories slightly during movement. The concentrations of such impurities/defects should be significant - in the order of 10^{17} cm^{-3}.

Some structural defect lines, e.g. threading dislocations, can indeed be inclined to the growth direction. Nitride-based materials are well-known for enhanced dislocation densities in comparison to e.g. arsenides. The existence of even 3-5 of such dislocation lines within a distance of 10 nm to the dot center can result in random patterns of spectral jitter, similar to those observed in the experiment. Then the densities of the dislocations are at least $3\text{-}5 \cdot 10^{12}$ cm^{-2}. For bulk wurtzite nitride materials reported concentrations of the line defects are of the order of 10^{8}-10^{12} cm^{-2}[Jai00, Sug98, Ros97, Les95, Pon02]. However, in the material close to a QD layer the dislocation density can be higher than in the bulk crystal, resulting in enhanced spectral jitter.

Conclusion

The results presented in this chapter describe the interaction of excitons in a QD with electric fields in its environment, which leads to SD. A statistics of emission linewidths was obtained for different excitation conditions. The observation of long-time SD was performed for several samples, grown with different techniques. The analysis of the results, backed up with theoretical calculations, allows to draw a conclusion about defects responsible for certain types of SD and to estimate the dipole moments of excitonic complexes.

The FWHM of the excitonic emission lines from GaN/AlN QDs ranges from the resolution limit of the set-up (1.65 µeV) up to 8 meV independent of excitation densities, measurement time in CL experiments and fabrication method (MOCVD and MBE). The same scatter of linewidths was found in complementary µPL experiments. Large FWHMs appear to be a specific property of the GaN/AlN QD material system and are attributed to the large built-in electric dipole moments of excitons in a QD. The dipole moments are a consequence of the large piezo- and pyroelectric fields present in these structures. Any influence of the charges located on sample surface on the linewidths of the emission lines could not be observed. The defects induced in the capping layer at low growth temperature, together with enhanced dislocation concentrations in the material close to the QD layer are likely to host the charges that lead to short-timescale SD. Even if a QD is resonantly excited, these defects are activated and cause large line broadening.

Luminescence intermittence of most of the measured emission lines was observed only for the MOCVD-grown GaN/AlN QD sample. As an explanation, a specific defect is proposed, which can stay for a time in the order of seconds/minutes in a particular configuration and then acts as a non-radiative center and modulates the luminescence of the QD. The defect can be mobile. Most probably it is introduced by some impurity, specific for MOCVD-growth, and its influence can be reduced by means of annealing. One possible defect of this kind can be oxygen in the configuration of a DX-center in AlN or GaN.

Characteristic patterns of long-timescale SD were used as a tool for the identification of emission lines stemming from the same QD. These observations represent an important step towards deciphering the QD emission spectra. Comparing the emission spectra of a large number of QDs, a typical arrangement of emission lines from a single QD can be obtained. Such specific fingerprints of luminescence of the single QD is a helpful information for theoretical modeling and further spectroscopic investigations of optical properties of individual QDs. In the present work a fingerprint consisting of 10 emission lines with a range of 60 meV was identified for GaN/AlN QDs grown with MOCVD.

A particular case of spectral jitter in the traces of the emission lines from single InGaN/GaN QDs and GaN/AlN QDs, reported for the first time, allowed to deduce a model for long-timescale spectral jitter in nitride-based QDs, in which a slowly

(~nm/s) moving charge propagates through the material along a straight trajectory close to a QD with a large built-in dipole moment. The field of the point charge induces an energy shift of the excitonic transition. A number of charge trajectories, inclined to the growth direction at different angles, can result in a random sequence of shifts of the emission energy. Possible origins of the moving charge can be the movement of charged impurities or mobile defects, induced via SEM beam irradiation, or weakly bound charges traveling along structural defect lines, like e.g. threading dislocations.

The slow spectral jitter and χ-patterns are specific for the nitride-based QDs and the suggested mechanism can be generally applied to this material system. The influence of the inhomogeneous electric field of a point charge in close vicinity to a QD on the excitonic emission energy was simulated using 8-band $\mathbf{k} \cdot \mathbf{p}$ theory and the Hartree model for InGaN QDs for the first time. The agreement of these numerical results with experimental observations of the χ-patterns verifies the proposed model of propagating charge.

Long spectral jitter of the emission lines of nitride-based QDs allows to estimate the properties of built-in dipole moment of the excitonic complexes. The value of the built-in dipole moment can be directly deduced from the measured regular χ-patterns. From the experiments for InGaN and GaN/AlN QDs values of $\mu_{built-in} = (0.3-3)\mathrm{e} \cdot \mathrm{nm}$ were estimated for the investigated samples. Also, the ratios $\mu_{built-in}^{Xi} : \mu_{built-in}^{Xj}$ can be obtained from irregular energetic shifts of different lines, stemming from the same QD. CL experiments revealed a noticeable difference of the built-in dipole moments of different (multi)excitonic complexes of the same dot, which is predicted in the theory as well.

4 Interaction with acoustic phonons

This chapter describes the interaction of charge carriers confined in a quantum dot (QD) and lattice vibrations. Nitride-based QDs which are strongly polar material systems should exhibit a significant difference in the coupling of the excitonic complexes to the acoustic phonons (X-aP) as compared to non-polar QD material systems, e.g. arsenides.

The chapter begins with a brief overview of the results, reported on phonon coupling to excitons in QDs, in section 4.1. Observations of acoustic-phonon side-bands of single GaN/AlN QD emission lines and their dependence on temperature in cathodoluminescence (CL) experiments follows in section 4.2. X-aP coupling is modeled with the independent Boson model. For the GaN/AlN QD material system realistic wave-functions were used as input parameters of X-aP interaction for the first time. A detailed analysis of the impact of the different phonon coupling mechanisms on the luminescence of GaN/AlN QDs is presented. The impact of spectral diffusion (SD) is also discussed. Section 4.3 analyzes the influence of dot size and aspect ratio on X-aP coupling. The interplay between vertical and lateral confinement of the charge carriers and phonon coupling mechanisms is elucidated. The dependence of line-shapes of emission lines on QD emission energies is considered. The results of numerical calculations are verified by experimental observations. Section 4.4 shows the temperature dependence of the emission linewidth in terms of phonon interactions.

Earlier micro-photoluminescence (µPL) experiments on a GaN/AlN QD sample have investigated the luminescence properties with a resonant excitation. In the present work the same QDs were also investigated using CL spectroscopy. Comparing the results obtained with the different excitation mechanisms makes it possible for the first time to investigate fundamental phonon interaction mechanisms.

©The calculations of the X-aP without account for SD were performed by *Matthias-René Dachner*, while the wave-functions of the QDs of the investigated series were modeled by *Gerald Hönig*.

4.1 State of the art

Elastic and inelastic scattering of acoustic phonons and charge carriers in QDs influences the line-shape of excitonic single-dot luminescence. The former contributes to the Lorentzian width of the zero-phonon line (ZPL), whereas the latter predominantly determines the shape of the phonon side-bands, but may lead to ZPL-broadening, too. An overview of experimental and theoretical studies of both effects is given below.

Understanding the exciton-phonon interaction in QDs is of particular interest for the use of single QDs in quantum information schemes [Loc06, Sal10b]. Interaction with phonons is known to be a major reason for dephasing and the loss of coherence of excitonic states [Hoh07, Car10]. Furthermore, in the presence of spin-orbit coupling spin-flip processes between the excitonic states can be phonon-mediated [Woo02, Tsi05].

One of the first major reports on the interaction of acoustic phonons with charge carriers confined in semiconductor nanocrystals was a theoretical study in [Tak93]. It was followed by time-resolved experiments on GaAs dot-like islands in [Fan98] and resulted in the formulation of a theory of exciton dephasing in semiconductor QDs in [Tak99].

Combined theoretical and experimental research of X-aP coupling was done in [Bes01] on CdTe/ZnSe QDs. A model for the complex line-shape was developed. The discrete excitonic states are coupled to a continuum of acoustic phonons; the X-aP coupling is considered in a non-perturbative regime. At low temperatures the spectra can be approximated with a Lorentzian profile, at higher temperatures acoustic side-bands appear. A number of studies, using the same formalism, were done on different QD material systems to investigate exciton-phonon interaction experimentally: e.g. CdTe/ZnMgTe in [Moe04], InAs/GaAs QDs in [Fav03] and GaAs/AlGaAs QDs in [Pet04].

The dephasing time of excitonic states in QDs was first measured in an exemplary research on InGaAs/GaAs QDs in [Bor01]. Four-wave-mixing spectroscopy was applied, since it intrinsically overcomes the problem of SD. A dephasing time of several hundred picoseconds was measured, corresponding to a homogeneous broadening of an emission line of only a few µeV. The non-exponential dynamics of polarization decay was shown to have a fast and a slow component resulting in a line-shape, consisting of a sharp Lorentzian line and a weak broadband. This broadband is the result of elastic coupling of acoustic phonons to excitons: when the exciton is optically created, a local shift in the equilibrium position of the lattice is induced. The Lorentzian shape results from inelastic processes such as radiative recombination and phonon-assisted activation into higher energy exciton states.

Similar to [Bor01] long dephasing times were measured on In(Al)GaAs/Ga(Al)As QDs in [Bir01] and in spectral hole burning experiments on CdSe nanocrystals [Pal03]. In the latter work the ZPL linewidth was detected to become as narrow as

6 µeV, when the effect of SD is eliminated by means of high modulation frequency of the excitation signal.

Interaction of excitons and phonons influences the pure dephasing of the excitonic states and results in homogeneously broadened ZPL. However, the experimentally measured linewidths of the emission lines of excitonic transitions also include inhomogeneous broadening due to spectral diffusion (SD). In order to simulate the experimentally observed ZPL, line broadening related to polarization decay can be introduced either by hand [Bes01, Kru02, Kru05b] or phenomenologically by means of the Grüneisen effect [Zim02] in numerical methods. Alternatively, the pure dephasing and the resulting ZPL broadening were calculated including second-order interactions with optical phonons [Usk00], quadratic interaction with acoustic phonons [Mul04], and real and virtual phonon-assisted transitions between exciton levels [Mul05, Gra09].

Exciton dephasing and absorption-line shape were investigated in substantial theoretical studies on a GaAs QD as a prototype [Kru02]. Particular attention was paid to the influence of static external electric fields, essential for the development of QD applications. For a description of the interaction of the exciton both with optical and acoustic phonons the independent Boson model is used; this model is exactly solvable. It was shown that electric fields increase polar part of the interaction, whereas the contributions of piezoelectric and deformation potential coupling are less affected.

The influence of electric fields is especially important for wurtzite-type nitride QDs, since huge built-in piezo- and pyroelectric fields are present in nitride-based heterostructures. One of the key papers on this subject is a theoretical survey of the influence of material parameters and dot geometries [Kru05b] for zinc blende (GaAs/AlGaAs) and wurtzite (GaN/AlN) QDs. It showed that deformation-potential coupling is sensitive to the overall spatial extent of the wave-functions of confined charge carriers. The spatial separation between electrons and holes is decisive for piezoelectric coupling, which becomes much enhanced in the presence of external electric fields. However, very few experimental studies on the interaction of phonons and excitons in nitride-based QDs exist.

Additionally to the QD geometry, the wave-functions of confined charge-carriers play an important role in the interaction between phonons and excitons. In the above-mentioned papers (e.g. [Kru02, Kru05b]) a simple analytical approximation for electron-hole wave-functions was used: The quasi two-dimensional wave-functions have a Gaussian distribution for the center of mass, and in-plane electron-hole correlation is described by an exponential function. In [Sto11] realistic wave-functions, calculated in the frame of 8-band $\mathbf{k} \cdot \mathbf{p}$ theory, were used to model the interaction of the exciton with both acoustic and optical phonons in InGaAs/GaAs QDs. Comparison of the experimental results demonstrated the advantage of these functions: they reproduce the experimental results very well, while the conventional Gaussian wave-functions fail.

4.2 Experiment and modeling

The experiments presented below were performed on GaN/AlN QDs (sample T, MOCVD growth) by means of CL experiments. The acceleration voltage was 7 kV and the electron beam current was 1.0 nA. The integration time of the detector was 20 s per spectrum for single spectra of temperature-dependent measurements. For all other single spectra, shown here, an integration time of 1 s was used.

4.2.1 Low-energy side-band and its temperature dependence

Most emission lines from single QDs show pronounced asymmetric side-bands on the low-energy side even at temperatures as low as 5 K. Figure 4.1 depicts the temperature dependence of a typical emission line resulting from exciton recombination in an individual QD. All spectra are normalized with respect to their integrated intensity and are shown on a relative energy scale. The change of the energetic position of the peak maximum is shown at the top of the right panel of figure 4.1. Emission was observed from 5 K up to RT, however starting around 120 K the peak maximum can no longer be separated from the side-bands.

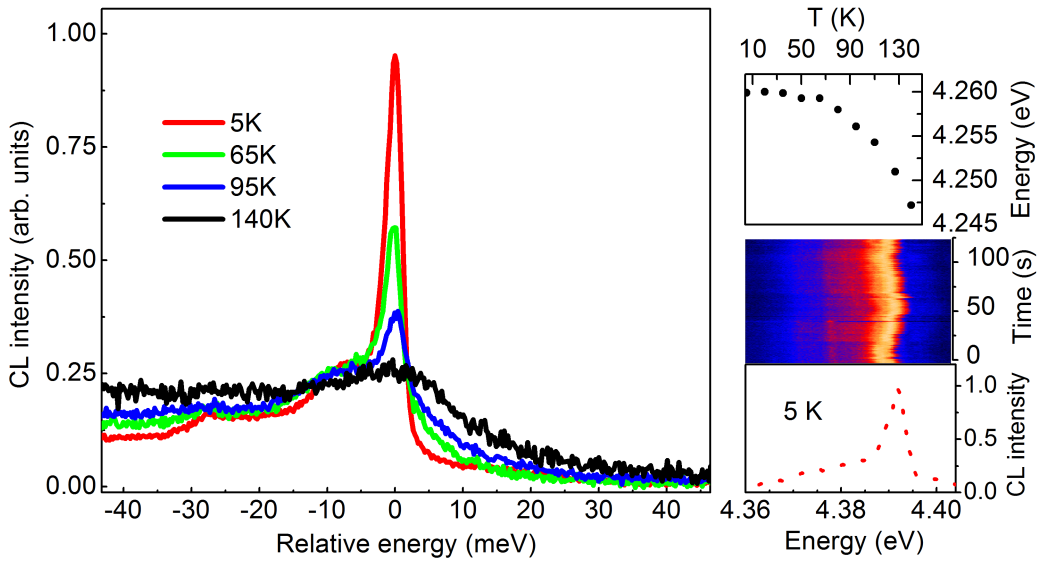

Figure 4.1: Temperature dependence of a single emission line on a relative scale. Right panel (top): Temperature dependence of the energetic position of the peak maximum; (bottom): A single emission line and its phonon side-band for a different QD at 5 K; (middle): Intensity-color-coded time evolution of the spectrum shown at the bottom.

An example of another emission line from a different QD is shown in the right panel of figure 4.1. The plot above displays the time evolution of the spectrum (SD-pattern). The same SD-behavior of the side-band and the peak maximum was

typically observed for various emission lines and confirms that the side-band and the peak maximum have the same local origin. The side-bands can neither be assigned to background luminescence, often observed for nitride-based QDs [Bar06, Sim08b], nor can they be ascribed to luminescence features from another QD.

With increasing temperature the intensity of the low-energy side-band grows with respect to the peak maximum, and a high-energy side-band emerges. The overall line-shape of the peak deviates strongly from either Lorentzian or Gaussian. Such line-shapes are typical for inelastic scattering of acoustic phonons with charge carriers in QDs. The observed side-bands are large in comparison to the ones observed in different QD material systems: CdTe/ZnTe [Bes01, Moe04] or In(Ga)As/GaAs [Fav03, Sto11].

The central emission line, which is hereafter referred to as ZPL, results from a radiative recombination process in the QD without energy loss/gain due to phonon emission or absorption. This ZPL is surrounded by a continuum of phonon-assisted radiative transitions. Phonon emission- and absorption-rates for a given phonon mode are proportional to $(n(\omega, T) + 1)$ and $n(\omega, T)$ respectively, where $n(\omega, T)$ is the phonon occupation number as given by the Bose-Einstein distribution for temperature T and phonon frequency ω. Both processes contribute to the low- and high-energy side-bands of the ZPL, resulting from phonon emission and absorption respectively. Since $n(\omega, T)$ is small for low temperatures, only phonon emission occurs resulting in highly asymmetric line-shapes. At higher temperatures, as $n(\omega, T)$ increases, the probability for phonon emission and absorption converges, resulting in more symmetrical side-bands with increasing T.

4.2.2 Exciton acoustic-phonon coupling modeling

A careful modeling was performed to quantitatively investigate the X-aP coupling in GaN/AlN QDs. The X-aP coupling is calculated in the framework of the exactly solvable independent Boson model (see section 2.3.3). The QDs are assumed to be a two level system which couples to a phonon bath through band diagonal coupling [Zim02, För03, Kru05b, Vag11]. The model includes both longitudinal acoustic (LA) and transverse acoustic (TA) phonons. The only input parameters are the QD wave-functions and the material parameters. Since the interaction between phonons and confined charge carriers occurs within the dot, the deformation-potential and piezoelectric constants of GaN are used to obtain realistic results (see also [Kru05b]). The phonon dispersion by contrast is described by AlN bulk phonon modes. The intrinsic homogeneous width of the calculated ZPL was chosen to correspond to the radiative decay time of approximately 1 ns, according to time-resolved measurements for the same samples [Kak03]. Additional contributions to homogeneous broadening such as non-diagonal coupling to higher states [Mul05, Mul07, Gra09] or a finite phonon lifetime [Ort04, Kru05a, Mac05] are not considered.

For an adequate description of the confined carriers realistic wave-functions from

8-band $\mathbf{k} \cdot \mathbf{p}$ theory are used as a starting point for calculating the X-aP coupling. Direct Coulomb and exchange effects are considered by self-consistent Hartree-Fock method (see section 2.3.2). The benefit of using 8-band $\mathbf{k} \cdot \mathbf{p}$ wave-functions was already reported in [Sto11]. These wave-functions were shown to agree better with the experimental results: the side-band shapes match the experimental data better than the wave-function of the Gaussian type as e.g. in [Kru02, Kru05b].

4.2.3 Calculated spectra

For wave-functions calculation a QD was modeled as a truncated pyramid of pure GaN with a height of 1.4 nm and a base length of 7 nm. The dot form is 20 % elongated in the base. Exciton emission energy of the dot is 4.03 eV. A numerically calculated spectrum for a temperature of 0 K is shown in figure 4.2 on a logarithmic intensity scale. As noted before, the calculated ZPL is solely represented by a Lorentzian function having a width of 5 µeV, which corresponds to the carrier-lifetime from time-resolved experiments [Kak03].

The ratio of the amplitudes of the phonon side-bands and the ZPL is smaller than those found in the experiment. The calculated spectra match the experimental data if the inhomogeneous broadening of the ZPL is included, as described in the next section. When SD is not taken into account, the numerical results are shown on a linear intensity scale with the focus on the side-bands for illustrative purposes.

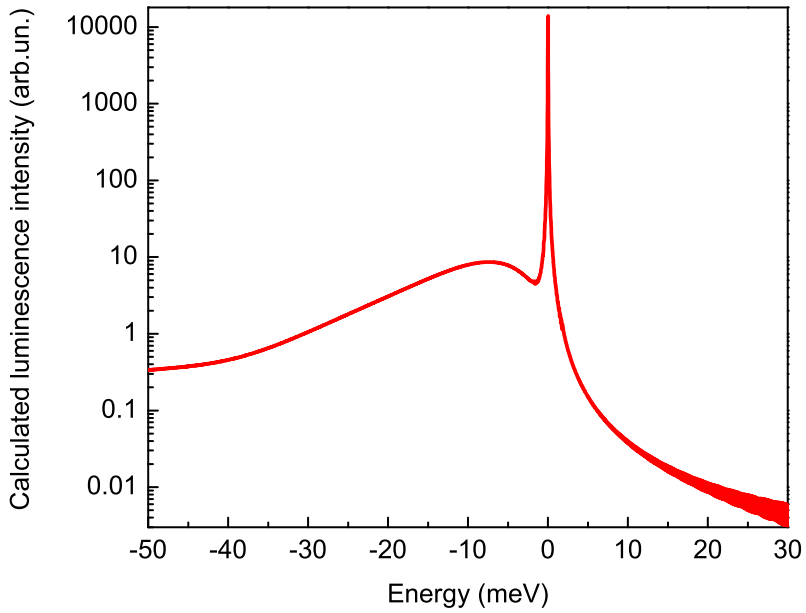

Figure 4.2: Calculated luminescence spectrum for a model QD.

Numerical results for the temperature dependence of the single spectrum from figure 4.2 are shown in figure 4.3. All spectra are normalized with respect to their

integrated intensity and are shown on a relative energy scale. The evolution of the phonon side-bands as observed in the experiment (figure 4.1) is very well reproduced by the calculated spectra.

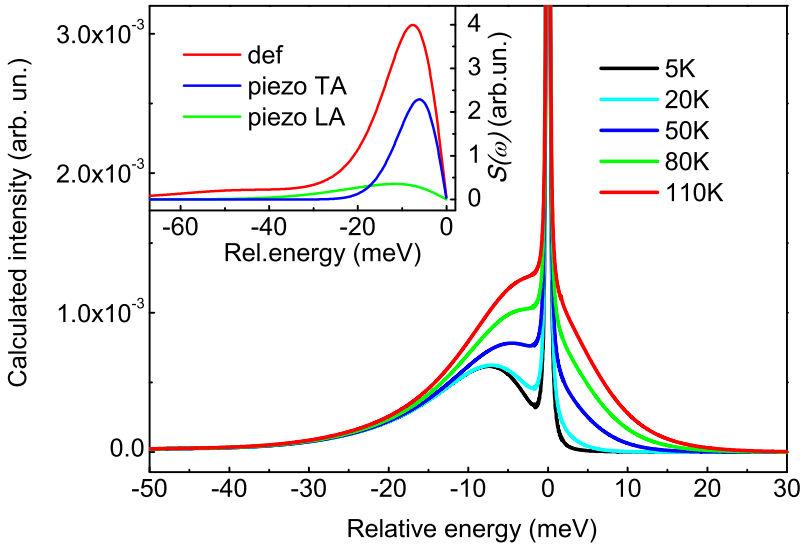

Figure 4.3: Calculated temperature dependence of a single emission line for the same model QD as in figure 4.2. The ZPL peak intensity for the 5 K curve is 1, not shown completely in the figure. The inset shows spectral densities $S(\omega)$. $S(\omega)$ for deformation-potential coupling is denoted as *def*, and for piezoelectric coupling to TA (LA) phonons as *piezo TA* (*piezo LA*).

For better understanding of the X-aP interaction the impact of deformation-potential coupling and piezoelectric coupling is investigated separately. For this purpose spectral densities $S(\omega)$ of these phonon coupling mechanisms are calculated as

$$S(\omega) = \sum_{\boldsymbol{q}} \frac{|g^{\boldsymbol{q}\kappa}|^2}{\hbar^2\omega^2}\delta(\omega - \omega_\kappa(\boldsymbol{q})) \tag{4.1}$$

Here $g^{\boldsymbol{q}\kappa}$ is the coupling element of the exciton to a phonon in mode κ with wave-vector $\boldsymbol{q}$, calculated from the carrier wave-functions, and $\omega_\kappa(\boldsymbol{q})$ is the phonon frequency. $g^{\boldsymbol{q}\kappa}$ is specific for the coupling mechanism. The deformation-potential coupling is effective for LA phonons only, whereas the piezoelectric coupling includes both LA and TA phonons. $S(\omega)$ gives the number of phonons of energy $\hbar\omega$ for each frequency ω, which are available in the system.

The inset of figure 4.3 shows the spectral densities $S(\omega)$ of different phonon coupling mechanisms for the model QD, corresponding to the low energy side-band at 0 K. At small energies (wave-vectors), the contribution of piezoelectric coupling to TA phonons is larger than piezoelectric coupling to LA phonons. Moreover, the overall piezoelectric coupling is of the same order of magnitude as the deformation-potential coupling for small energies.

The piezoelectric coupling plays an important role in nitride-based materials [Kru05b]. The calculations of the phonon spectral densities for different coupling mechanisms above confirm that the piezoelectric coupling cannot be neglected for GaN/AlN QDs, as it is done for arsenides. Further investigation of the influence of the piezoelectric effects on X-aP coupling in dependence on the structural parameters of the QDs is given below in section 4.3.

4.2.4 Including spectral diffusion

The ratio of the amplitudes of the phonon side-bands and ZPL in the numerical spectra (figure 4.2) is significantly smaller than those found in the experiment (see figure 4.1). However, the numerical results for the temperature dependence of the phonon side-band agree qualitatively very well with the experimental results.

Nitride-based QDs show large emission linewidths (see results in chapter 3) as compared to e.g. arsenides [Bay02a]. In the modeling of the X-aP coupling presented here (see section 3.4.1), inhomogeneous broadening is not included. This inhomogeneous broadening is attributed to SD (see section 1.3.2). SD results in smearing the spectral features within the detection time, as can be seen in the right panel of figure 4.1.

Figure 4.4 shows a comparison of a measured QD emission line and a modeled curve, taking into account X-aP coupling and SD. A typical experimentally observed emission peak, depicted as a dotted line in the figure, was fitted with a Gauss-profile to get the energetic distribution function resulting from SD. This fit resulted in a Gaussian function with the width of 1.7 meV. In the next step a spectrum, taking into account X-aP coupling as in the section above (see figure 4.2), was convoluted with a Gauss-profile with a width of 1.7 meV. The resulting curve is depicted in figure 4.4 as a solid line. Comparison of this spectrum with the one experimentally obtained shows that ZPL and phonon side-band amplitudes in the calculated data agree very well (see figure 4.4).

The fact that calculated and experimentally obtained amplitudes match very well when SD is superimposed, indicates that SD plays a significant role in ZPL broadening. A possible method to identify the real value of homogeneous broadening is to measure the dephasing time by four-wave mixing [Bor01], which may reveal the intrinsic emission linewidth for the GaN/AlN QDs.

Generally speaking, a Voigt profile should be used. The homogeneously broadened QD emission line has a Lorentz profile with the width w_L, which is then inhomogeneously broadened by SD, induced by the QD environment. Additionally the measured emission lines are broadened by the measuring apparatus: monochromator and detector. SD results in Gaussian line broadening with the width $w_{G,SD}$, as the trap and release of the charges in the defects is a stochastic process, described as a normal distribution. The instrumental broadening is described by a Gaussian profile with the width $w_{G,Inst}$. As was shown in chapter 3, $w_{G,SD} \geq w_{G,Inst} \backsim 1.5\,\mathrm{meV}$.

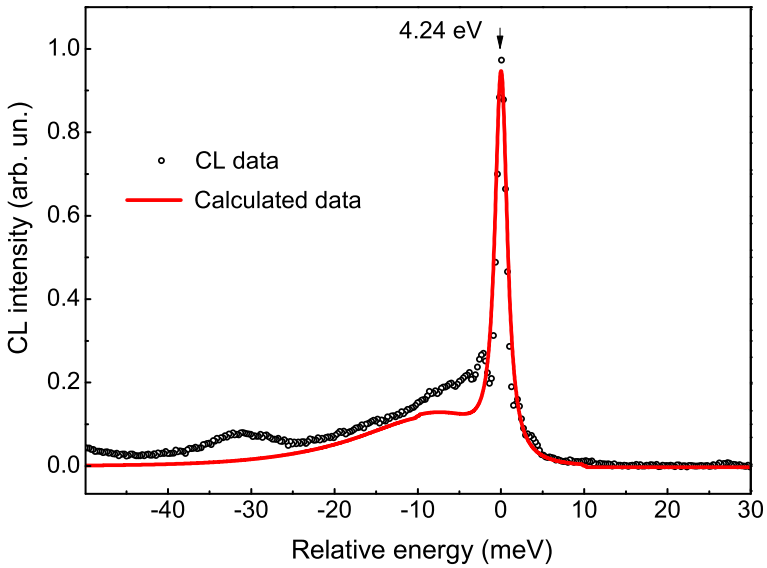

Figure 4.4: Comparison of experimental data (dotted line, ZPL at 4.24 eV at 5 K) and calculated spectrum (solid line), including the effect of SD.

$w_L \backsim 5\,\mu eV$ (see relation (1.9) in section 1.4). Thus, $w_L \ll w_{G,Inst} \leq w_{G,SD}$ and the width of the Voigt profile, as a convolution of Lorentzian and Gaussian profiles, can be approximated by a Gaussian profile.

4.3 Influence of charge carrier confinement

4.3.1 Investigated dot series and calculated luminescence spectra

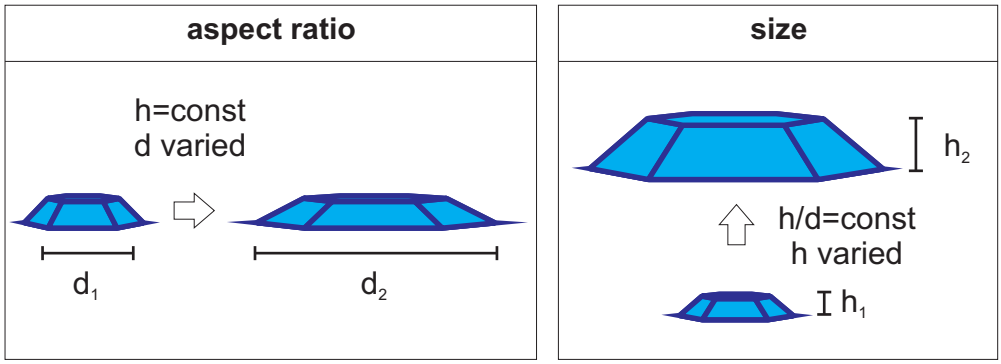

Figure 4.5: Investigated series of model QD.

The dependence of X-aP coupling on the morphology of the QDs is analyzed in this section. Two series of QD structures were modeled and investigated. Both are shown

schematically in figure 4.5: variation of the QD size and variation of the QD aspect ratio (ratio of height to base length) at constant size. Each series contains five dots. Dots have the shape of a truncated pyramid with a 20 %-elongated hexagonal at the base. Luminescence spectra shown in this section are calculated without including the SD effects.

In the series with varied sizes (hereafter size-series - see right panel in figure 4.5) model QDs have a constant aspect ratio of 0.2. The height increases from 0.8 nm to 2.0 nm, resulting in respective base length variations from 4 nm to 10 nm. This size variation refers to experimental observations of the size evolution of self-organized GaN/AlN QDs [Hos04, Kak06, Kin10a]. This series is used to analyze the impact of the confinement of the charge carriers in the vertical direction[1] and the influence of the built-in excitonic dipole-moment, since for GaN/AlN QDs $\mu_{built-in}$ scales with the dot size.

Figure4.6 shows the numerical results for the luminescence spectra of the QDs of

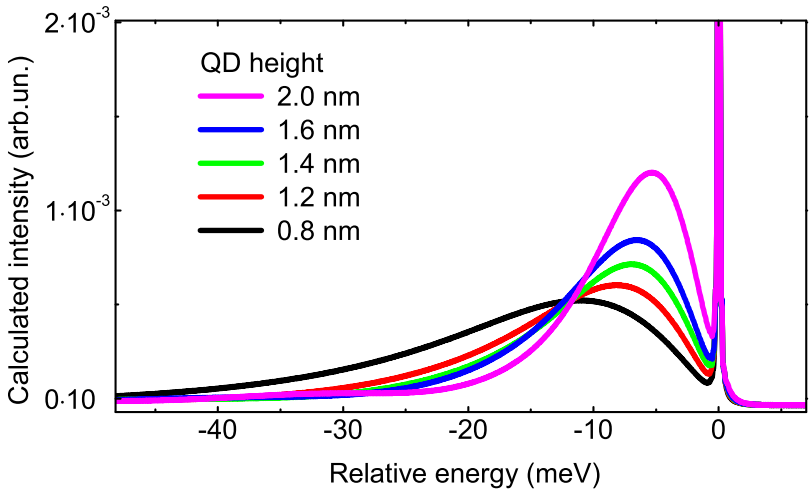

Figure 4.6: Calculated spectra of model QDs of size-series. At a constant aspect ratio the dot height is varied from 0.8 nm up to 2.0 nm. The QD emission energy decreases respectively from 4.8 to 3.6 eV. The ZPL intensity is normalized to 1 and not shown completely.

the size-series. Intensity of the low-energy phonon side-band increases monotonously with QD size. This tendency is associated with a strong influence of the built-in piezo- and pyroelectric fields. The taller the dot becomes, the larger is the drop of the built-in potential within the QD, resulting in an increase of the excitonic electron-hole dipole-moment. Consequently, the larger the dipole-moment is, the larger is the coupling to acoustic phonons via piezoelectric coupling.

[1]Here "vertical" means parallel to growth direction. Lateral - parallel to the base plane of the QD.

In the series with varied aspect-ratio (hereafter: aspect-ratio series, see left panel

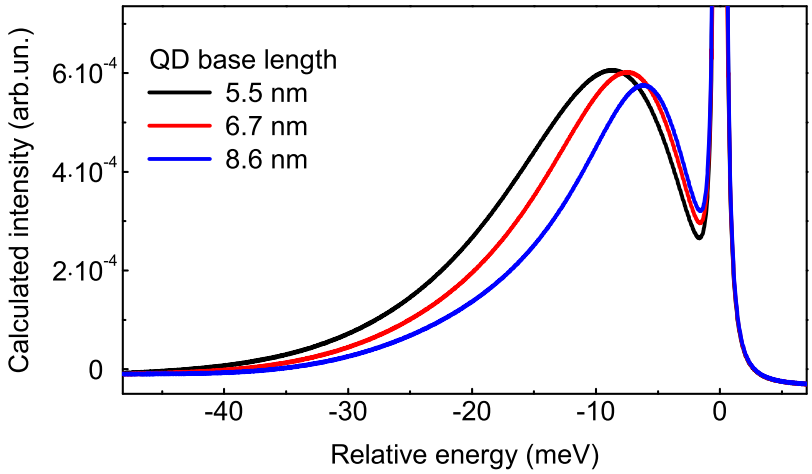

Figure 4.7: Calculated spectra of model QDs of aspect-ratio series. At constant height of 1.2 nm, aspect ratio is varied from 0.22 down to 0.14 (base length respectively from 5.5 nm to 8.6 nm). The QD emission energy respectively decreases from 4.3 to 4.1 eV. The ZPL intensity is normalized to 1 and not shown completely.

in figure 4.5) model QDs have a constant height of 1.2 nm and the aspect ratio was increased from 0.14 to 0.22, resulting in respective base length variations from 8.6 nm to 5.5 nm. The impact of the lateral extension of the wave-function on X-aP coupling can be analyzed with the help of this series.

The resulting luminescence spectra for the QDs of aspect-ratio series are shown in figure 4.7. Here and further on the results for the QDs with the aspect ratio 0.16 and 0.20 are omitted, and only the results for the remaining three QDs of the series are displayed for illustrative purposes. Almost no influence of the QD base length on the intensity of the side-band is found. The position of the maximum of the side-band shifts towards the ZPL with increasing base length.

4.3.2 Influence of dot geometry on coupling mechanisms

For a detailed analysis, the spectral densities for different coupling mechanisms were obtained from the numerical results for the QDs described above. Figure 4.8 shows the spectral densities for deformation-potential coupling ($S(\omega)_{\mathrm{def}}$), and figure 4.9 for piezoelectric coupling to both TA and LA $S(\omega)_{\mathrm{piezo}} = S(\omega)_{\mathrm{piezo\ TA}} + S(\omega)_{\mathrm{piezo\ LA}}$.

Figure 4.8 (top panel) shows how the amplitude of $S(\omega)_{\mathrm{piezo}}$ increases monotonously with the increasing size of the QD. When the QD height increases, the separation of the center of the mass for electron and hole wave-function increases too. Thus, figure 4.8 shows the direct impact of the excitonic dipole moment on the piezoelectric coupling mechanism.

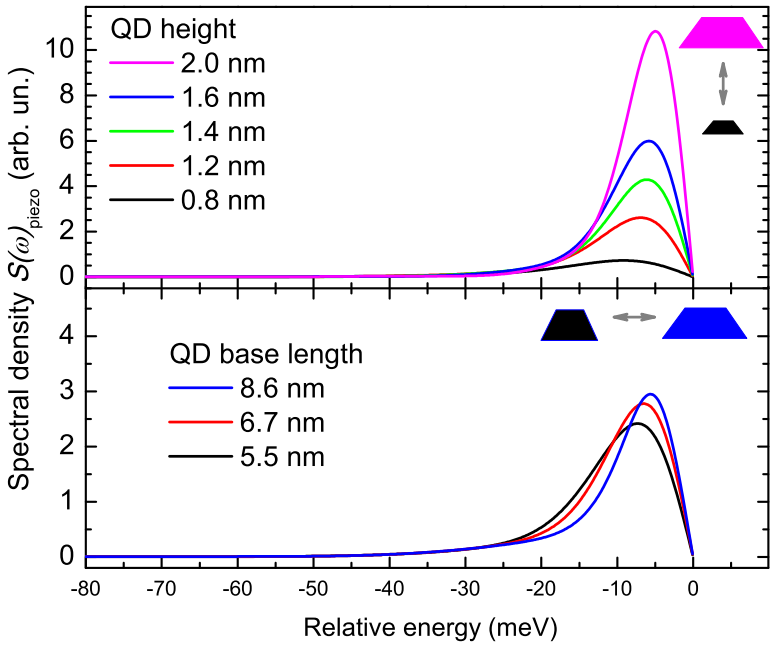

Figure 4.8: Calculated spectral densities $S(\omega)_{piezo}$ for model QDs. Top: Size-series. Bottom: Aspect-ratio series.

The lateral confinement of the charge carriers, in contrast, has no influence on the piezoelectric coupling, as illustrated in figure 4.8 (bottom panel). Here the slight change of the amplitude of the $S(\omega)_{\text{piezo}}$ with change of the QD base lengths is attributed to the difference of the dipole moments of the model QDs. Although the height remains constant for the aspect-ratio series of the model QD, the 8-band $\mathbf{k} \cdot \mathbf{p}$ calculations revealed different values for the spatial separation between the electron and the hole wave-functions.

Figure 4.9 (bottom panel) reveals a strong dependence of the deformation potential coupling on the lateral extension of the wave-functions. The amplitude of $S(\omega)_{\text{def}}$ decreases and the maximum shifts to smaller phonon energies when the QD base length increases: For the stronger lateral confinement of the charge carriers the deformation potential coupling of X-aP is more effective and it is significant for large wave-vectors. The same tendency is shown in figure 4.9 (top panel). Both the amplitude $S(\omega)_{\text{def}}$ and the wave-vector of the $S(\omega)_{\text{def}}$ maximum decrease with the increase of the QD size, which fact is rather attributed to the impact of the wave-function extension than to the excitonic dipole-moment.

4.3.3 Line-shapes in dependence on emission energy

As described in chapter 3, due to large electron-hole separation in GaN/AlN QDs the excitonic emission energy is sensitive to changes of the local electric fields. QDs of this material system exhibit pronounced SD, including large linewidths. The

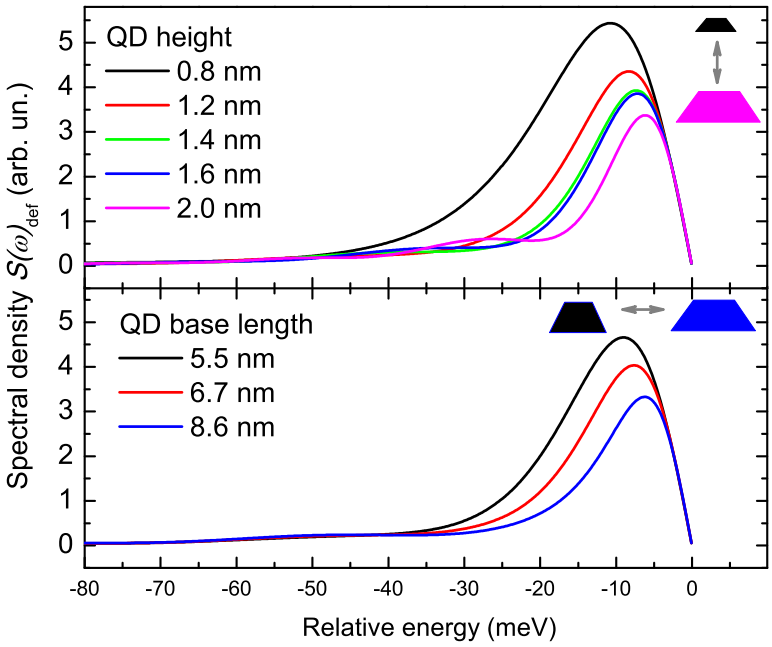

Figure 4.9: Calculated spectral densities $S(\omega)_{def}$ for model QDs. Top: Size-series. Bottom: Aspect-ratio series.

average full width at half maximum (FWHM) of the emission lines scales with the QD size (i.e. the built-in dipole-moment), as was shown in µPL experiments in [Kin10b].

Figure 4.10 shows calculated emission spectra for model QDs of varied height and constant aspect ratio, including the effect of SD. For this purpose the same procedure as for figure 4.4 is applied to the calculated spectra for QDs of the size-series. Each spectrum was convoluted with a Gaussian profile of the width d. The width arrived at from the dependence of the FWHM of the emission lines on the QD emission energy, measured for GaN/AlN QDs in complementary µPL experiments ([Kin10b]). Based on 8-band $\mathbf{k} \cdot \mathbf{p}$ calculations, the model QDs with the heights 0.8, 1.2, 1.4, 1.6 and 2.0 nm have an emission energy of 4.80, 4.25, 4.03, 3.90, and 3.56 eV respectively. The widths d then are 1.5, 2.4, 3.4, 4.1 and 6.4 meV respectively (see figure 3.2, adopted from [Kin10b]).

Figure 4.10 reveals that the phonon side-bands appear significantly larger in luminescence spectra for smaller recombination energies of the single GaN/AlN QDs. For larger dots their larger phonon side-bands can become as intense as the broadened ZPL.

The dependence of the line-shapes on the emission energy helps to explain the striking discrepancy of the µPL and CL measurements, performed on the same QDs and shown previously in section 3.2.4 (see figure 3.10 on page 62). In CL experiments for small emission energies hardly any distinct emission line could be

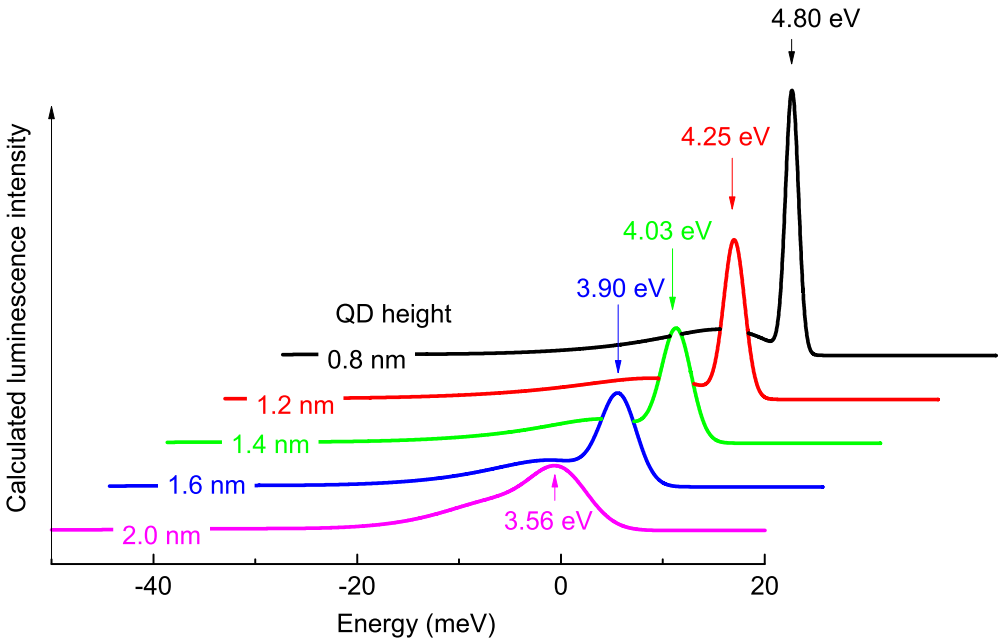

Figure 4.10: Convolution of the calculated emission spectra for model QDs of the size-series with Gaussian profiles of different widths expected for the emission energy (see text for description). The height and the emission energy of the model QD is marked for each curve.

resolved, although the spectral resolution of the set-up is better in this spectral range. Two features specific for CL excitation provide an explanation:

(i) Due to large excitation energies a large number of excited charge carriers can be excited in a QD already at low currents, creating multiexcitonic complexes. In contrast, for small laser powers the excitation densities, created in resonant µPL excitation, can be insufficient to generate multiexcitonic complexes in the dot. Consequently, it is possible that for certain excitation conditions in µPL experiments fewer excitonic emission lines appear in a luminescence spectrum of the dot, than for CL experiments.

(ii) The excess energy of the hot carriers dissipates by means of enhanced coupling to phonons in CL excitation, hence the coupling to phonons is more effective in CL experiments than in µPL experiments.

For GaN/AlN QDs under the CL excitation overlapping of the larger number of emission lines with large phonon side-bands results in broad band luminescence in the spectra for detection energies below 4.0 eV. Consequently, individual features of the QD emission are obscured in the CL spectra. In PL spectra the resolved lines at small emission energies show the line-shapes, as predicted in figure 4.10.

4.3.4 Discussion

The results obtained from numerical calculations correspond very well to the experimental finding. In addition to the sample described above, similar asymmetric line-shapes with significantly large low-energy side-bands were observed for another investigated sample of GaN/AlN QDs (sample L).

Figure 4.11 shows various spectra of single QDs, emitting in the energy range between 4.20 eV and 4.55 eV. The side-bands are clearly visible on the low-energy side of the individual peaks. Here the energy difference of the maximum of the side-band relative to ZPL varies between 4 meV and 6.4 meV. The form of the side-bands varies too: the side-bands are convex in panels b and d, and sloping in a and c. The diversity agrees well with figure 4.7, where the model QDs of similar energies exhibit various forms of side-bands. For QDs with a larger base length calculations arrive at a smaller energetic distance of the side-band maximum relative to the ZPL.

In the numerical model only coupling to the neutral exciton (one electron and

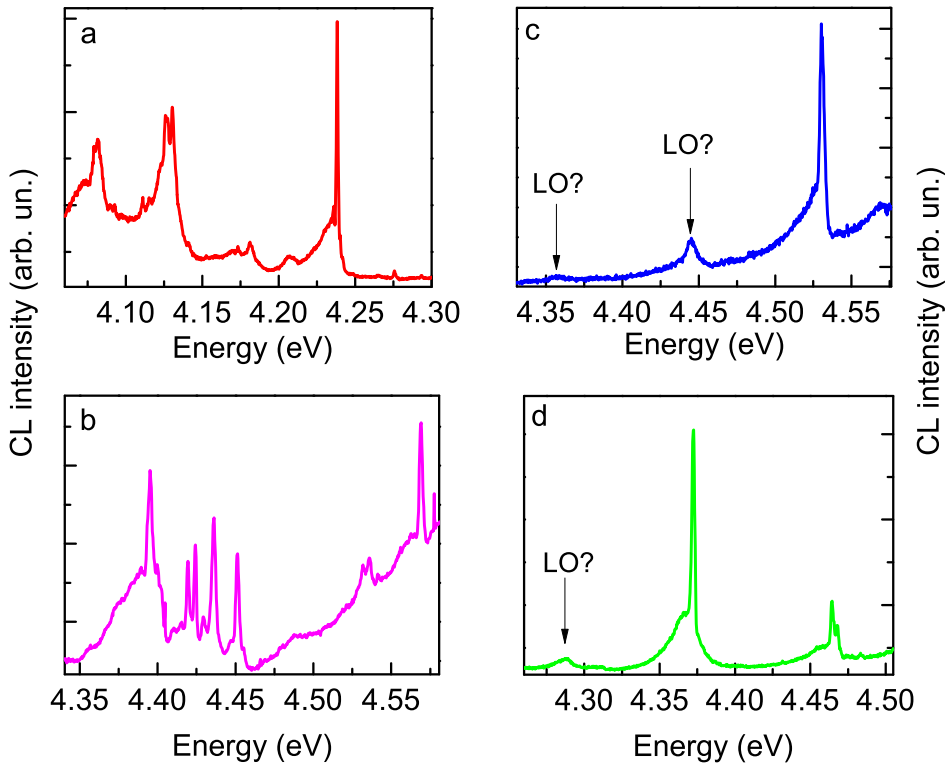

Figure 4.11: CL spectra of emission from single QDs, measured on different mesa structures at 5 K.

one hole) was considered. Generally speaking, comparison of these results with all emission lines in a CL spectrum is controversial. No identification of the line origin in the experiment was yet possible, emission lines might stem e.g. from more complex excitonic configurations. Acoustic phonons couple to different excitonic complexes in a different way. Thus, investigating GaAs/AlGaAs QDs in [Pet04] it was found that the biexciton couples about three times stronger to phonons than the exciton. Moreover, as shown in the previous chapter excitonic complexes from the same QD have different built-in dipole-moments and hence the piezoelectric contribution of X-aP coupling differs, too.

Both $S(\omega)_{\text{def}}$ and $S(\omega)_{\text{piezo}}$ exhibit a maximum for a relative energy of 5-10 meV (see figures 4.8 and 4.9). These values are in the range of fine-structure splitting of excitonic bright states measured for these QDs [Kin10a]. Consequently, for these QDs spin-flip processes between the bright-exciton states or from bright into dark states may occur, since in the presence of spin-orbit-coupling such spin-flip processes may also be promoted by the interaction with acoustic phonons [Woo02, Tsi05].

The careful modeling presented above showed enhanced piezoelectric coupling of acoustic phonons to excitons of GaN/AlN QDs, which scales with the QD size. In [Kru05b] it was shown that choosing the material system with increased piezoelectric coupling as well as reducing the QD size enhances the dephasing. Therefore a trade-off for the QD size is necessary to achieve the least dephasing for use of the GaN/AlN QDs in applications demanding long coherence times.

4.4 Influence of temperature

The dependence of the QD emission lines on temperature was investigated for five individual QDs. An increase of the linewidth with increasing temperature was observed. The temperature dependence of the FWHM for one of the lines is shown in figure 4.12. The luminescence spectra for the respective QD are shown in figure 4.1.

For each spectrum the ZPL was fitted with a Gaussian profile. The resulting widths are depicted as blue circles. For high temperatures (T>120 K) the ZPL could no longer be separated from the phonon side-bands, therefore these data were not considered. The red lines show two fits of the ZPL widths with a following function:

$$\Gamma^2(T) = \Gamma^2_{min} + \left(\Gamma_0 + \gamma_{ac} T + \frac{\gamma_{LO}}{\exp(\frac{\hbar\omega}{kT}) - 1} \right)^2 \tag{4.2}$$

This function is derived from equation (1.11) in section 1.4 under the following assumptions:

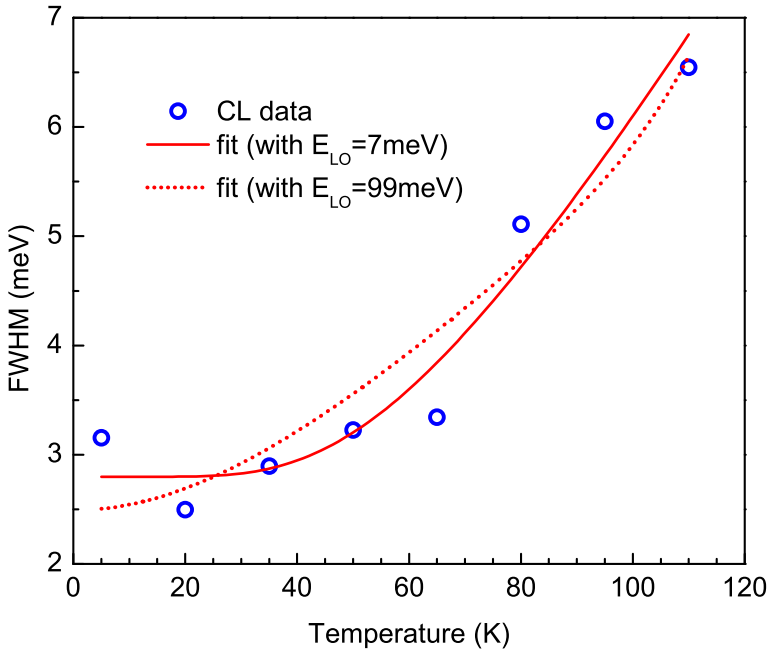

Figure 4.12: Temperature dependence of the linewidth of a single QD emission line. Circles depict the FWHM of the experimental emission lines, measured in CL and fitted with a Gaussian profile. Solid and dashed lines depict fits with various parameters, as described in the text.

(i) Inhomogeneous broadening of the line is attributed to SD. In the previous chapter it was shown, that the excitation density in CL experiments does not change FWHMs of GaN/AlN QDs at 5 K, because all defects, which influence the emission of the QD, are activated under CL excitation. Therefore with increasing temperature, SD should not raise, and the inhomogeneous broadening can be approximated to be constant: $\Gamma^2_{inhom}(T) \approx const = \Gamma^2_{SD}$. This constant term can be taken into account together with the broadening induced by the set-up, which can be assumed to be constant as well, and $\Gamma^2_{min} = \Gamma^2_{app} + \Gamma^2_{SD}$ in equation (4.2).

(ii) There are no reports on dephasing times for GaN/AlN QDs that would determine Γ_0. Therefore the homogeneous line width is assumed to be of similar size as in the other QD material systems, where it was arrived at by measuring the dephasing times in four-wave-mixing experiments [Bor01, Bir01, Pal03] and found to be amounting to $\Gamma_0 \approx 5\,\mu eV$ (see also relation (1.9) in section 1.4).

(iii) The Bose-Einstein function is used to describe the occupation density of optical phonons $N_{LO}(T) = \left(\exp(\frac{\overline{\hbar\omega}}{kT}) - 1\right)^{-1}$, where $\overline{\hbar\omega}$ is the average optical phonon energy.

The solid red line in figure 4.12 shows a fit with none of the fitting parameters

fixed. The resulting values for the fitting parameters are shown in table 4.1 as fit A. Coupling to optical phonons γ_{LO} has a rather small value, compared to the reported parameters for other material systems [Rud90]:
e.g. 50 meV in InAs/GaAs QDs [Fav03] and 125 meV in non-polar GaN/AlN QDs [Rol06]
However, the average optical phonon energy is much smaller than the values of LO phonons GaN (87.3 meV) and AlN (99 meV). Coupling to acoustic phonons γ_{ac} is in contrast very small, which contradicts the enhanced X-aP interaction, described earlier in the chapter.

Table 4.1: Parameters resulting from the fit of the experimentally measured dependence of QD emission linewidth on temperature with formula (4.2).

	fit A	fit O (AlN)	fit O (GaN)
Γ_{min}, meV	2.8	2.5	2.5
γ_{ac}, µeV/K	$4.9{\cdot}10^{-22}$	50	50
γ_{LO}, meV	7.6	$3.5{\cdot}10^{5}$	$1.0{\cdot}10^{5}$
$E_{LO} = \overline{\hbar\omega}$, meV	7.2	99 (fixed)	87.3 (fixed)

For another fit the parameter $E_{LO} = \overline{\hbar\omega}$ was fixed for the energy of LO-phonons in GaN and AlN respectively: 87.3 meV and 99 meV. The red dotted line in figure 4.12 shows the fitting curve for $E_{LO} = 99\,\text{meV}$, which is not significantly different from the one for $E_{LO} = 87.3\,\text{meV}$. The values of the remaining fit parameters are shown in table 4.1 as fit O. The resulting γ_{LO} appears unreasonably large. Smaller values of γ_{ac} were usually reported:
5-8 µeV/K in polar GaN/AlN QDs [Dem09], 12 µeV/K in non-polar GaN/AlN QDs [Rol06] and 0.1-0.5 µeV/K in In(Ga)As/GaAs QDs [Bay02a, Kam02].

Remarkably, the value for $\overline{\hbar\omega} = 7\,\text{meV}$ from the fit A is in the range of the maximum of the calculated acoustic-phonon spectral-density. The results of the fit of experimental data suggest that it is justified to neglect the contribution of optical phonons to the emission line broadening. In this case equation (4.2) can be be transformed into:

$$\Gamma^2(T) = \Gamma_0 + \gamma N(T) \tag{4.3}$$

Here $\gamma \approx 7\,\text{meV}$ and $N(T) = \left(\exp(\frac{\overline{\hbar\omega}_{ac}}{kT}) - 1\right)^{-1}$, $\overline{\hbar\omega}_{ac}$ - average acoustic phonon energy, which can be obtained from the spectral density of the acoustic phonons: see relation (4.1). The term $\gamma N(T)$, describing coupling to acoustical phonons becomes important for $\Gamma(T)$ at elevated T, when $kT \gg \overline{\hbar\omega}_{ac}$.

All the processes of phonon scattering contribute to the homogeneous linewidth of excitonic transition $\Gamma(T)$. Knowing the spectral density of the acoustic phonons from modeling (relation (4.1)) and accounting for the X-aP coupling parameters, a more accurate expression for $\Gamma(T)$ can be obtained by the same method as used for semiconductors e.g. in [Rud90].

However, interaction of the excitons in GaN/AlN QDs with optical phonons was observed in the CL experiments. Several weak emission lines at a distance of 83 meV-100 meV on the low-energy side of the emission lines were often observed for the investigated QDs. The value is comparable to the LO-phonon energy of GaN and AlN. Some examples are shown in figure 4.11 b, d. Here the energetic spacing between the luminescence peaks, indicated by arrows, and the ZPL is 83 meV-87 meV. The variation of the energy is commonly explained by different distribution of the strain in the surrounding material, due to differences in QD size and Ga-incorporation [Hei96]. The replicas appear broadened up to tens of meV, which can be attributed to SD, same as the ZPL broadening. A detailed investigation of the interaction of the LO-phonons and further evaluation of the coupling strength in terms of the Huang-Rhys factor [Hua50] is beyond the scope of the present work.

Conclusion

In this chapter the influence of lattice vibrations on the excitonic emission from single GaN/AlN QDs was investigated. Enhanced acoustic-phonon coupling in single GaN/AlN QDs was evidenced in temperature dependent CL experiments. X-aP interaction was modeled and analyzed with respect to QD size and geometry and the role played by coupling mechanisms.

The carrier-phonon interaction is calculated in the framework of the independent Boson-model using realistic electron and hole wave-functions obtained from 8-band $\mathbf{k} \cdot \mathbf{p}$ theory in combination with the Hartree-Fock method. This model accounts very well for the experimental observations of the shape and position of the phonon side-bands. The intensity ratio of the ZPL to the phonon side-bands obtained by numerical calculations matches the experimentally measured one only when SD is superimposed. The importance of taking SD into account is again emphasized and the major impact of SD on the inhomogeneous line broadening is proven.

The influence of the excitonic built-in dipole moment and the lateral extension of charge-carrier wave-functions was analyzed with respect to X-aP coupling. QDs of different sizes and aspect ratios were considered in the model. The spectral phonon densities for the X-aP interaction mechanisms were considered. Piezoelectric coupling is found to be of the same order of magnitude as deformation-potential coupling for this QD material system. The interaction with TA phonons is found to be of greater importance as compared to coupling to LA phonons. Numerical simulation reveals enhanced phonon side-bands for larger QDs, in other words for larger dipole-moments. The lateral extension of the wave-functions is responsible for the energetic position of the side-band relative to the ZPL. The important role of the aspect ratio on the acoustic-phonon side-band was also confirmed in CL experiments by variation of the line-shapes of the QD emission peaks of the same energy.

Strength of SD and phonon coupling increase with the QD size. The numerical calculation showed, that the combination of both effects leads to relative increase of the side-band with respect to the ZPL. The acoustic-phonon side-bands can grow almost as large as the ZPL with decreasing QD emission energy. This tendency explains the discrepancy in measurements by means of µPL and CL on the same mesa structure. No discrete emission lines could be observed in CL spectra of single QDs for detection energies smaller than 4.0 eV. Overlapping of different lines, significantly broadened by SD and with intense acoustic-phonon side-bands obscure the individual features of single QDs in CL experiments. Side-bands of emission lines observed in µPL experiments verify the dependence of the line-shapes on the QD size, found in numerical calculations.

The temperature dependence of emission linewidth was analyzed. For low temperatures it is mainly due to SD. At higher temperatures acoustic phonon scattering plays a major role in the increase of the homogeneous linewidth, while the contribution of optical phonons can be neglected.

Results: site-controlled arsenide-based quantum dots

5 Strain-induced growth and luminescence properties

This chapter presents the investigations of the first test-structures with site-controlled quantum dots (QDs) by means of cathodoluminescence (CL) spectroscopy. The structures are grown with a new approach. The novel "bottom-up" technique for the lateral positioning of semiconductor QDs is based on the strain modulation by means of a buried stressor. This stressor controls the local self-organization of QDs. The results illustrate the fundamental principle of strain-mediated growth and its influence on the luminescence properties.

The chapter begins with a short overview of the state of the art in section 5.1. A brief introduction of the new concept, backed up with calculations of the strain distribution, follows in section 5.2. This section also includes the experimental findings of the influence of the buried stressor on the optical properties of an overgrown heterostructure, demonstrated in CL experiments with the help of quantum well (QW) test-structures. A description of the fabrication of the first site-controlled QD structures follows in section 5.3. Section 5.4, constituting the main part of the chapter, describes the CL experiments on the resulting InGaAs/GaAs QD structures. These experiments elucidate, how the stressor triggers the formation of the QDs and influences their luminescence. The influence of size and position of the buried stressor on luminescence properties of the QDs is investigated. The following optical properties were investigated: spatial and spectral distribution of QD luminescence, spectral diffusion (SD), and emission polarization.

©The method of site-controlled growth of QDs was originally developed by *the team of D. Bimberg* at Technische Universität Berlin in cooperation with *V. Haisler*. The calculation of the strain distribution were performed by *Andrei Schliwa*.

5.1 State of the art

The wide range of possible applications for QDs requires further development of growth techniques. Up to now the self-assembly growth approaches (e.g. for the Stranski-Krastanow mode [Gol85, Ape95, Dau97, Shc98]) produce large amounts of QDs with large areal density and a finite size distribution, which leads to a distinct inhomogeneous broadening of the QD ensemble luminescence. Small inhomogeneous broadening (< 10 meV) is crucial to efficient QD lasers [Led08] and infrared detectors [Kri05]. Many applications such as solid-state cavity quantum electrodynamics [Hen07, Gal08], single- and entangled-photon emitters [Loc06, Shi07, Joh08, Sal10b], single-QD lasers [Rei08], single photon detectors [Kom00] demand a precise control of the emission energy and the position of the single QD.

The principles of self-assembled QD growth can impede the controlled positioning of the QDs. Minimization of the total energy of the coherently strained islands, growing upon a strained layer, is in the base of formation of QDs [Shc95, Shc98]. These islands - the QDs - are formed if the reduction of strain energy due to island formation exceeds the energy expenses associated with newly formed surfaces and edges. QDs grow on the sites of increased strain energy or lower facet formation energy [Shc04]. On natural surfaces only surface steps act as nucleation sites of the QDs [Nöt98].

Different attempts are being made to avoid the process of spontaneous nucleation of QDs and to achieve controlled positioning of QDs. Physical or chemical templates pre-define the nucleation site, where the QD will then grow epitaxially. Various successful techniques were reported for the site-controlled growth of QDs: patterning of the substrate material [Atk08], use of strain fields [Lee01], and surface relief features [Sch09c]. For the substrate pre-patterning electron beam lithography [Sch07b, Sch08b, Atk08, Mer09, Dal10, SS11], focused ion beam lithography [Lee11], local oxidation [MS05] or nano-imprinting [Hak10] are used.

These methods are per se sophisticated. The challenge is to achieve at a good optical quality of the resulting QDs. The positioned QDs should potentially possess a narrow spectral distribution, a pre-defined emission range and narrow linewidths of emission lines of single QDs. Successful integration of the positioned QDs into nanophotonic devices was demonstrated e.g. by the teams of O. G. Schmidt [Sch07b, Atk08] and A. Forchel [Sün08, Sch09c, Hug11]. Here the best value for the linewidth of the emission line of an excitonic transition of a site-controlled QD is reported to be 43 µeV [Hug11]. Excellent results were achieved by the team of E. Kapon in ÉPFL with QD growth in inverted pyramidal recesses [Har97, Har99, Wat04, Gal08, Fel09, Moh10b]. Generation of entangled photons was demonstrated for these highly symmetrical dots [Moh10a].

Several difficulties are characteristic for substrate pre-patterning techniques:

(i) Controlled QD-nucleation is possible in close vertical vicinity to the structural patterning. Missing QDs at shallow holes, patterned on a

growth surface, is often reported [Lee11, SS11]. Etching of the surface during pre-patterning results in numerous defect sites around the QDs. This reduces structural and optical properties of the QDs. Although sophisticated cleaning procedures are performed prior to growth, these pre-patterning techniques produce QDs with lower radiation efficiency and broader linewidths, compared to QDs grown on planar substrate surfaces [SS11, Lee11]. The linewidth of QD emission lines is sensitively dependent on imperfections of the material [Bay02a].

(ii) These technologies involve precise nm-scale fabrication steps and are not easily scalable to large wafer sizes.

(iii) There is no self-alignment of an electrical current path relative to the QD. This is important for the efficient injection of the charge carriers into single QDs in future devices.

5.2 Strain engineering by buried stressor

5.2.1 Concept

The novel method of site-controlled growth of QDs was originally developed by the team of D. Bimberg at Technische Universität Berlin in cooperation with V. Haisler. A buried stressor layer induces strain fields in the matrix material. A spatial modulation of the strain due to the structure of the stressor layer results in a local modification of the surface free energy. Thus the subsequent growth of the QDs on such a surface will preferentially take place at its local minima of strain. The stressor is created by volume change of an outer part of the buried layer while leaving the volume of the inner part of the layer unchanged. This can be performed e.g. in a chemical reaction by substituting one of its atomic components by a different type.

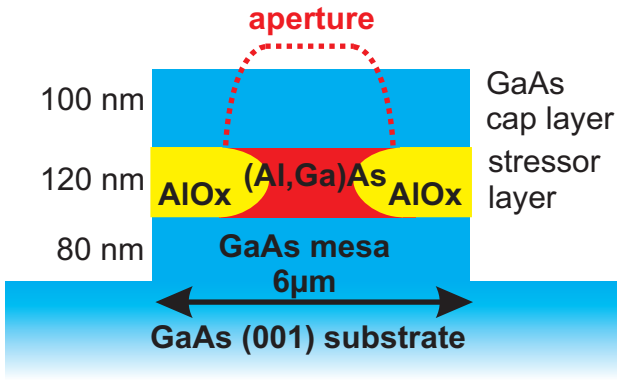

Figure 5.1: Schema of the mesa structure, used in the calculations.

The method is applied to the technologically important InGaAs/GaAs QD material system in the present work. The stressor layer is formed by an $Al_xGa_{1-x}As$ layer. If it is embedded into mesa structures, then As-atoms are substituted by oxygen during the oxidation process. Additionally, the volume of $Al_xGa_{1-x}As$ decreases due to oxidation [Cho97]. Thus a controlled oxidation of mesa structures would result in a strain layer with an outer region of aluminum oxide AlO_x and an inner (Al,Ga)As region (see figure 5.1). The volume contraction of the (Al,Ga)As region induces strain in the neighboring material.

InAs has a larger lattice constant than GaAs, and in the $In_xGa_{1-x}As$/GaAs system the QD formation occurs due to the interfacial lattice mismatch ~ 3-7 % for x > 0.30. The points of maximum tensile strain at the GaAs surface correspond to the points of lowest strain for the $In_xGa_{1-x}As$ layer, growing on top of the GaAs. During growth, the atoms will move to the minima of their respective surface strain energy if the surface diffusion length is sufficiently large.

5.2.2 Strain distribution calculations

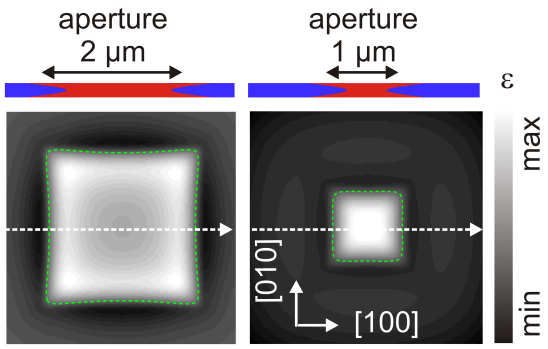

Figure 5.2: Calculated sum of the in-plane strain components $\varepsilon(x, y) = \varepsilon_{xx} + \varepsilon_{yy}$ at the surface of a GaAs(001) substrate for a buried (Al,Ga)As/AlO_x stressor structure covered by 100 nm GaAs for aperture diameters of 2 µm (left) and 1 µm (right). The green dashed line indicates the aperture border, here $\varepsilon(x, y) = 0$. The white dashed arrows show the positions of the cross sections shown in the next figure (5.3).

To analyze the strain in the material, calculations with a continuum mechanical model were performed. The structure used for the calculations is a rectangular mesa with 6 µm sides as schematically shown in figure 5.1. The interface between the outer AlO_x and inner (Al,Ga)As regions of the stressor layer is approximated as an inward-pointing parabola. The inner region is hereafter called aperture. Transformation from (Al,Ga)As to AlO_x was assumed to contract the unit cell volume by 7 % isotropically. This value is regarded as the lower limit of the experimentally observed AlGaAs volume contraction during oxidation [Kel04]. Here the plastic relaxation

effects play a major role, as the bond lengths difference is expected to result in a volume contraction of 20 %. The difference in the thermal expansion is neglected, since the temperatures of the oxidation process and the QD growth are more or less the same (see section 5.3.1).

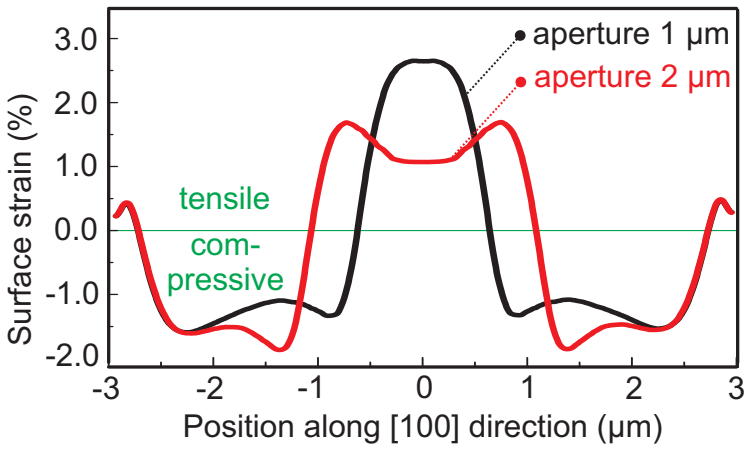

Figure 5.3: Cross-sectional line-scans of the strain distribution $\varepsilon(x, y) = \varepsilon_{xx} + \varepsilon_{yy}$ at the surface of GaAs(001), indicated with arrows in figure 5.2, for structures with aperture side lengths of 2 µm (red line) and 1 µm (black line). The green line indicates the border between tensile and compressive strain.

A GaAs layer follows the aperture. The InGaAs QDs nucleate on the GaAs surface. The strain distribution $\varepsilon(x, y)$ at the surface of GaAs was calculated. The distribution of the sum $\varepsilon(x, y) = \varepsilon_{xx} + \varepsilon_{yy}$ is depicted in figure 5.2 for two different sizes of the aperture. Then negative values of $\varepsilon(x, y)$ correspond to the compressive strain, while positive $\varepsilon(x, y)$ - to tensile. The rectangular form and crystallographic orientation of the aperture is due to the observed anisotropic oxidation of the (Al,Ga)As layer. The contracted volume of AlO_x leads to a region of compressive strain above and a tensile force onto the region at the boundaries between the oxide and the (Al,Ga)As. For the aperture of 2 µm side length (right panel of figure 5.2) the maximum in-plane strain is surrounding the inner part of the aperture. For an aperture side length of 1 µm (left pane of figure 5.2) the maximum strain is found at the center of the aperture.

Depending on the GaAs layer thickness on top of the stressor layer, the magnitude of the interfacial strain varies. Here a GaAs layer with a thickness of 100 nm was assumed, resulting in $\varepsilon(x, y)$ in the order of 1-1.5 %. This magnitude of the surface strain is sufficient for the QD growth. Figure 5.3 shows the quantitative profile of $\varepsilon(x, y)$ for the line scans in [100]-direction across the center of the apertures (indicated by the white dashed arrows in figure 5.2). For the larger aperture (side length of 2 µm) two separate maxima of the tensile in-plane strain are located above the aperture boundary. For the smaller one (side length of 1 µm) - the maxima merge to a single centered strain maximum. The strain maximum remains nearly

constant for about 200 nm, afterwards a transition to compressive strain occurs within the following 200 nm.

The growth rates of $In_xGa_{1-x}As$ will be highest at the minima of surface strain-energy distribution: as can be seen in figure 5.2 preferentially above the aperture boundaries and corners. For the small enough aperture sizes (here side length of 1 µm) the area of $In_xGa_{1-x}As$ growth then merges into a region in the middle of the aperture. Outside the aperture the strain energy for $In_xGa_{1-x}As$ increases abruptly. Consequently, in certain areas of the aperture the amount of $In_xGa_{1-x}As$ will increase. Increased concentration of In-atoms triggers the QD nucleation [Toy93]. Selective growth of QDs at the aperture boundaries is expected.

5.2.3 Quantum well test-structures

To test the influence of the buried stressor, a structure with a QW was grown first. The mesa structures were fabricated as briefly described above (see figure 5.1). A 60 nm-thick GaAs buffer layer followed the stressor layer and then a 5-nm thick $In_{0.15}Ga_{0.85}As$ QW was grown, capped with a GaAs cap-layer. In this section the results for the mesa structure with a diameter of 40 µm are shown. Oxidation of the stressor layer resulted in the aperture size of ~ 20 µm for this mesa diameter.

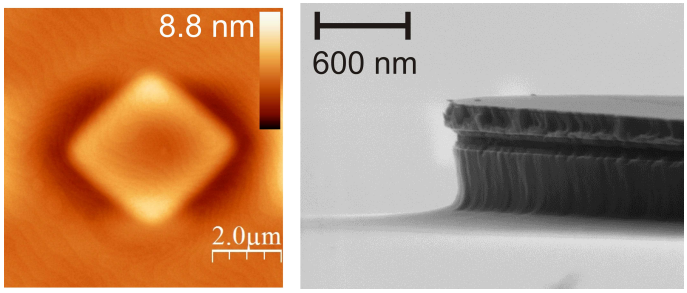

Figure 5.4: Left: Surface image at the center of a mesa surface taken by AFM after oxidation of the buried aperture layer. The surface height modulation is due to the volume reduction of the buried layer during oxidation. Right: SEM image of the mesa structure before QD overgrowth seen from the side.

Oxidation leads to a surface height modulation across the aperture, which is revealed by atomic-force microscopy measurements (AFM) of the mesa structure after the oxidation process (left panel in figure 5.4).[1] This surface modulation is a consequence of the volume reduction due to oxidation and can therefore be assigned to the aperture boundaries. The volume reduction of the buried stressor layer is clearly visible on the SEM image of the mesa structure (right panel in figure 5.4).

The overview CL spectrum of the sample is shown at the bottom of figure 5.5. The luminescence of the QW is observed here as a peak at 1.42 eV with FWHM

[1] All the AFM data were kindly provided by André Strittmatter.

of 17 meV. The bulk GaAs excitonic luminescence is seen as a weak band around 1.50 eV. The top of figure 5.5 shows the spatial distribution of CL intensity, so-called cathodoluminescence spectral images (CLSIs). To obtain a CLSI a CL spectrum is taken for each excitation spot of the beam on the sample: see section 2.1. The two CLSIs in the figure are shown for two energy ranges: at the low- and the high-energy side of the QW-peak, as indicated in the figure.

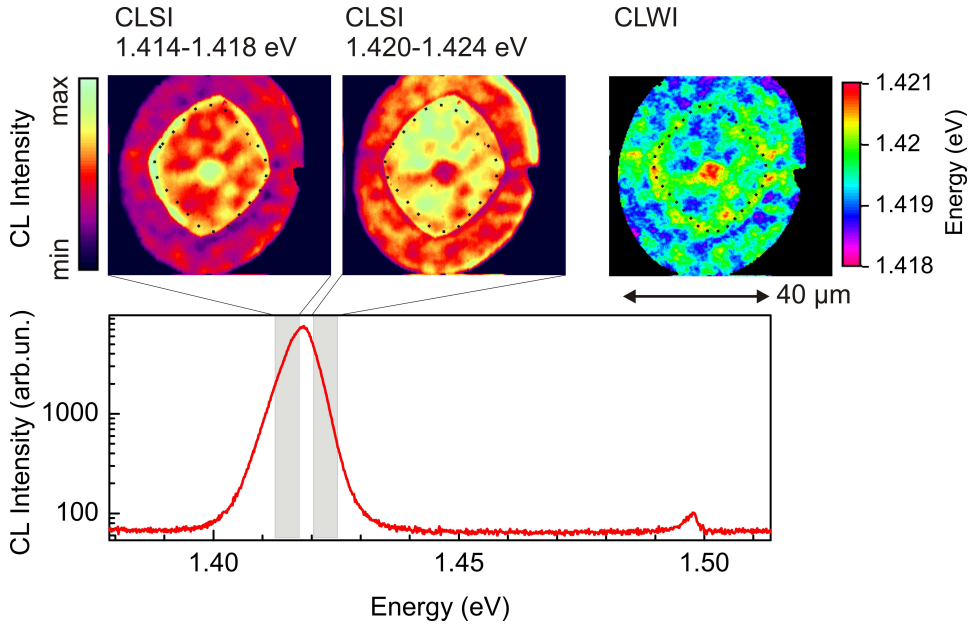

Figure 5.5: Bottom: integral CL spectra with luminescence of the QW and GaAs bulk measured on the mesa structure with a diameter of 40 µm. Top left: CLSI for the low-energy and the high-energy side of InGaAs-QW peak. Top right: CLWI for the emission energies of 1.418-1.421 eV. Both CLSI and CLWI have the spatial dimensions of 36 µm x 44 µm. Black dotted line indicates aperture boundary. The areas with the luminescence of low SNR are blacked out.

These two CLSIs appear to be close to their complementary counterparts. The sites of low CL intensity for a detection energy of 1.414-1.418 eV are the sites of high CL intensity for a detection energy of 1.420-1.424 eV and vice versa. This cannot be an experimental artifact, as these patterns vary depending on the size of the mesa structure. The cathodoluminescence wavelength image (CLWI - distribution of the wavelength of maximum intensity: see section 2.1), displayed in the top panel of figure 5.5 shows a site-dependence of the energy of the QW excitonic transition.

A buried stressor induces anisotropic strain in the overgrown structure. The individual variation of the components ε_{xx} and ε_{yy} differs from the distribution of the $\varepsilon_{xx} + \varepsilon_{yy}$, shown for the model structure in the previous section (see e.g. figure 5.16). Also, change of ε_{xx} and ε_{yy} influence ε_{zz}. Certain relations between ε_{xx}, ε_{yy} and ε_{zz} govern the energetic positions of the conduction and valence bands in the QW, and consequently the transition energy of the heterostructure (see e.g. [Sin03]).

Both CLSIs and CLWI reveal, how strain anisotropy results in a spatial variation of the transition energy and the intensity of the QW structure in correlation with the buried stressor.

To sum it up, the QW test-structures showed the possibility to significantly influence the luminescence of a heterostructure by means of a buried stressor. Fabricating stressors with different shapes and at various distances to the overgrown active layers (QW, QDs, etc) makes it possible to design structures with site-controlled optical properties.

5.3 Site-controlled quantum dot growth

5.3.1 Sample fabrication

The samples with controlled QD positioning were grown by metal-organic chemical vapor deposition (MOCVD) at Technische Universität Berlin, Germany. Figure 5.6 shows sample structure and growth steps, which are listed below in detail.

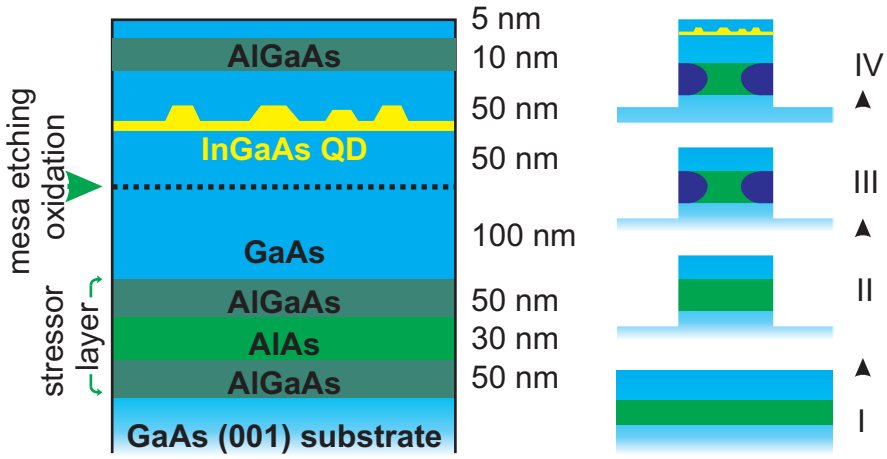

Figure 5.6: Schema of the sample structure (left) and growth steps (right).

(i) The layers for creating the stressor were grown at a temperature of 700 °C. First, a GaAs buffer layer was grown on GaAs(001) substrates. It was followed by a sandwich structure which consists of a graded 10 nm thick $Al_{0\text{-}0.9}Ga_{1\text{-}0.1}As$ layer, a 40 nm $Al_{0.9}Ga_{0.1}As$ layer, a 30 nm AlAs layer, another 40 nm $Al_{0.9}Ga_{0.1}As$ layer, and an oppositely graded $Al_{0.9\text{-}0}Ga_{0.1\text{-}1}As$ layer. Finally, a GaAs 100 nm thick layer was grown on top of the sequence.

(ii) Circular mesa structures of a height of 300 nm were fabricated ex-situ by conventional photolithography and reactive ion etching in order to

expose the side facets of the (Al,Ga)As layers. The mask layout provides different mesa sizes, varying from 25 to 10 µm in steps of nominal 0.07 µm on the same wafer. Thus, similar oxidation times result in different aperture sizes depending on the mesa diameter.

(iii) Oxidation of (Al,Ga)As into AlO_x was done in a special reaction chamber using a mixture of 3 slpm nitrogen and 50 sccm[2] water vapor as the oxidizing agent. The reactor chamber was held at a total pressure of 50 mbar while the sample was heated to 450 °C. In a hot water steam environment the As-atoms are substituted by oxygen in a chemical reaction during the oxidation process. The oxidation rate at a given temperature and pressure decreases exponentially with the Al content for AlGaAs and is zero for GaAs. For an Al-content of $0.92 < x_{Al} < 1.0$ the volume of $Al_xGa_{1-x}As$ decreases by ~ 6.7 % to 13 % during the oxidation process [Cho97]. The anisotropic oxidation rates of the (Al,Ga)As layer along the [010] and [100] crystallographic directions result in rectangular aperture shapes. For an oxidation depth of 7-8 µm, square-like apertures were obtained for mesa diameters larger than 14 µm. Mesas of diameters smaller than 13 µm are fully oxidized.

(iv) For subsequent overgrowth with QDs, the substrates were loaded back into the MOCVD reactor. The QD growth sequence started with a bake out of 5 min at 715° C under arsenic atmosphere followed by a 50 nm thin GaAs buffer layer grown at 685° C before lowering the temperature to 515° C for QD growth. After initial deposition of 2 ML of $In_{0.5}Ga_{0.5}As$ (~ critical thickness for the 2D/3D growth mode transition), QDs are formed during a growth interruption. Under such conditions, the QD densities on planar wafers (without buried stressor layer) are reproducible in the range of mid 10^7 - low 10^8 cm^{-2}. To avoid the negative impact of surface states on the luminescence intensity, the QDs were consequently covered by 50 nm GaAs, 10 nm $Al_{0.4}Ga_{0.6}As$ and 5 nm GaAs.

5.3.2 AFM investigations

The samples with uncapped QDs were investigated with AFM. It was found that the QDs aligned in a square-like pattern, tracing the boundaries of the aperture. Figure 5.7 shows AFM images for mesa structures of different sizes. The corresponding nominal mesa diameters and aperture sizes are indicated. The QDs appear as hillocks and show clear lateral ordering in a square-like pattern for the larger mesa diameters (20 and 16 µm). Here the QDs align along the sides of the square stressor boundary at an areal density of $1.25 \cdot 10^{10}$ cm^{-2}. With decreasing the aperture size

[2]slpm - standard litres per minute (unit of gas flow rate); sccm - standard cubic centimeters per minute (unit of gas flow rate)

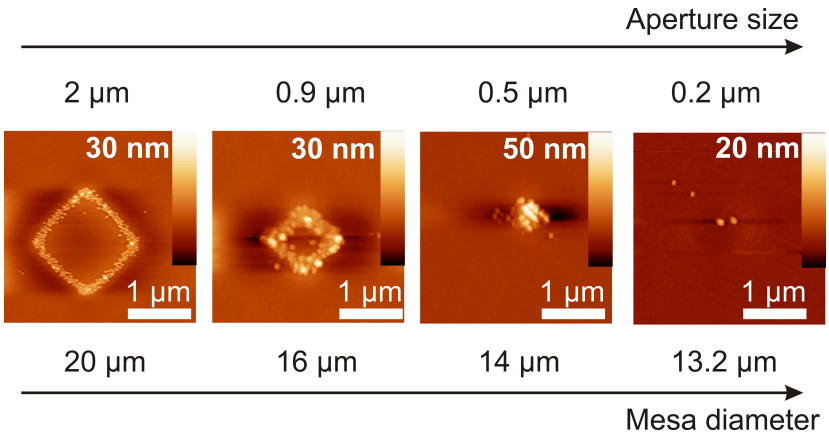

Figure 5.7: AFM images of the centers of mesa structures overgrown with quantum dots. Mesa diameters and corresponding aperture sizes are indicated.

the square-like QD arrangement transforms into a single cluster of about 50 QDs for aperture sizes of less than 700 nm (14 µm mesa size). For an aperture size of less than 500 nm only 2 QDs are left at the center of the aperture. Here, the slight circular elevation of the mesa center indicates the remaining stressor size.

These results agree very well with predictions, presented in section5.2: QDs align at the inner aperture boundaries with the lowest strain energy of InAs. Also, the width of the QD alignment region is very close to the numerical results. For an aperture size below 600 nm the QD ensemble merges to one centered cluster, as predicted.

5.4 Site-dependent luminescence properties

5.4.1 Spatial distribution of luminescence

The basic optical properties of the samples were analyzed by spatially resolved CL at a temperature of 5 K. For this purpose, CLSIs were recorded and CLWIs analyzed. For the experimental data shown below the acceleration voltage was 3 kV, yielding a lateral resolution of ~ 300 nm. Most of the single spectra and CLSI were taken with integration times of 10 ms - 30 ms and with a spectral resolution of the set-up of 140 µeV in the spectral range of 1.20 eV-1.40 eV (30 µm slit, grating 1200 lines per mm), unless otherwise indicated.

The integral CL spectra of the mesa of a diameter of 20 µm is shown in the bottom panel of figure 5.8. It reveals the luminescence of the wetting layer (WL), centered at 1.38 eV, and a broad luminescence ranging from 1.19 eV up to 1.37 eV. This broad luminescence stems from QDs, which can be seen in the highly-resolved spectra shown in the section below and which will be called QD hereafter. The top panel of

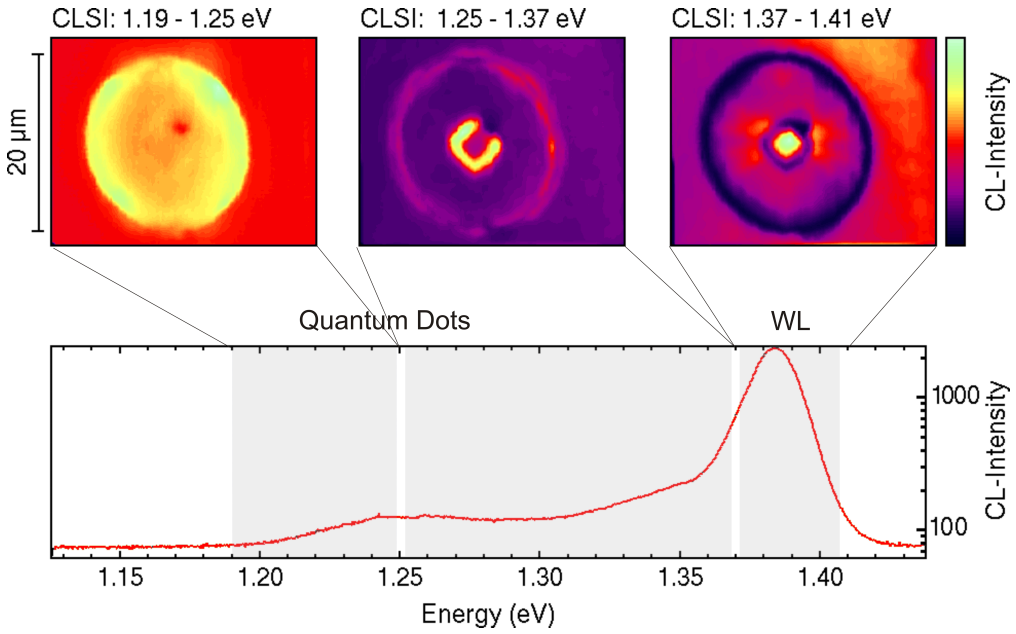

Figure 5.8: Bottom: Integral CL spectrum, showing luminescence of the QDs and WL for a mesa structure with a diameter of 20 µm. Top: CLSI for different detection energies: low- and high-energy QD luminescence (1.19-1.25 eV and 1.25-1.37 eV) and WL luminescence (1.37-1.41 eV). CL spectra were measured with a spectral resolution of 560 µeV (30 µm slit, grating 300 lines per mm).

figure 5.8 shows the CLSI for three detection energy ranges: 1.37 - 1.41 eV (WL), 1.25 - 1.37 eV (called "high-energy QD" hereafter) and 1.19 - 1.25 eV ("low-energy QD" hereafter). The bulk GaAs excitonic luminescence was also observed but is not shown here.

The analysis of the CLSI for different energies provides information about the site-dependent distribution of the WL- and QD-luminescence. Figure 5.8 shows that the intensity of WL luminescence decreases to a minimum on those sites, where intense luminescence of QDs is found. The intensity of the WL-peak decreases, when the recombination of the charge carriers is effective in the QD structure.

The luminescence of low-energy QDs is distributed over the mesa and becomes intensive on its edges, where it shows a four-fold symmetry. The same distribution of luminescence of low-energy QDs was found for mesa structures with a fully-oxidized stressor layer. The luminescence of high-energy QDs is strong on the edge of the mesa and is intense along the square-shaped boundary in the middle. This boundary coincides with the border of the aperture, an effect which could be observed in the SEM image of the sample surface during measurement. For the mesa structure of 20 µm in diameter, the aperture was observed to be a rectangle with 2 µm sides. Hence, the intense luminescence of high-energy QDs in the CLSI in figure 5.8 occurs over the aperture boundary.

To investigate the QD luminescence, single spectra were measured for distinct sites

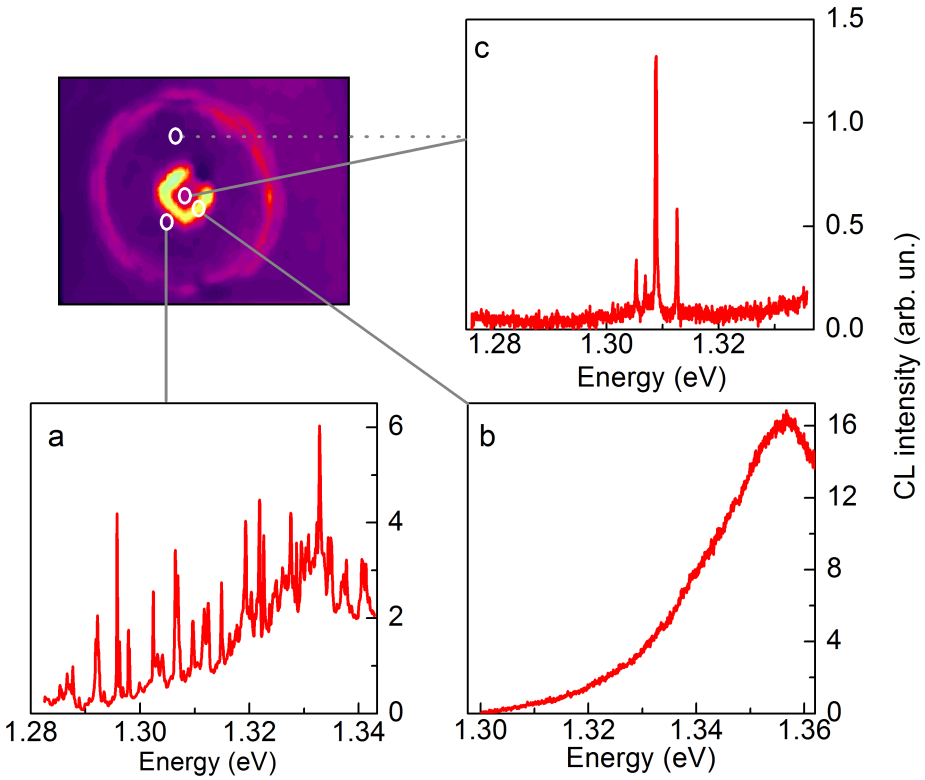

Figure 5.9: Single spectra, showing luminescence of high-energy QDs for a mesa structure with a diameter of 20 µm. The schema shows the positions on the mesa, where the spectra were taken. Spectra from the region outside the aperture are similar to the spectra c and are not shown here.

on the mesa structure with the best spectral resolution of the set-up. Here the range of high-energy QDs was analyzed, as it correlates distinctly with the aperture boundary, in contrast to low-energy QDs. These measurements exhibited spectrally separated peaks, varying for different excitation points: the emission lines of different emission energies and intensities appear in the spectra on different sites. The typical spectra are shown on figure 5.9. Such behavior is typical for QD emission: The sharp emission peaks indicate 3D localization of the charge carriers. Since the excitation conditions used assure a spatial resolution of 300 nm, the site-dependent variation of the CL spectra reveals the formation of individual QDs.

The spectra in figure 5.9 also indicate the dependence of the density of the QDs on the position on the mesa structure. Indeed, all over the mesa except for the aperture boundary, widely spaced spectrally sharp luminescence lines are observed (similar to figure 5.9 c). For the excitation points close to the aperture boundary and the mesa edges, the number of the lines in the spectra increases (see figure 5.9 b): the QD density increases. This turns into a broad luminescence band on the sites over the

aperture boundary (figure 5.9 a): In these areas the QDs with the highest densities are grown.

The samples with QDs grown on planar substrates without a stressor layer underneath with low QD density ($< 10^8$ cm^{-2}) exhibit spectra similar to figure 5.9 c: see, for example, [Seg06]. Samples with QDs of a higher density ($\sim 1...5 \cdot 10^{10}$ cm^{-2}) exhibit spectra as shown in figure 5.9, a and b: see e.g. [Rod05]. These findings agree very well with the results of the AFM investigations of uncapped samples, described in the previous section.

As shown in section 5.2.2, theoretical calculations predict dependence of the QD

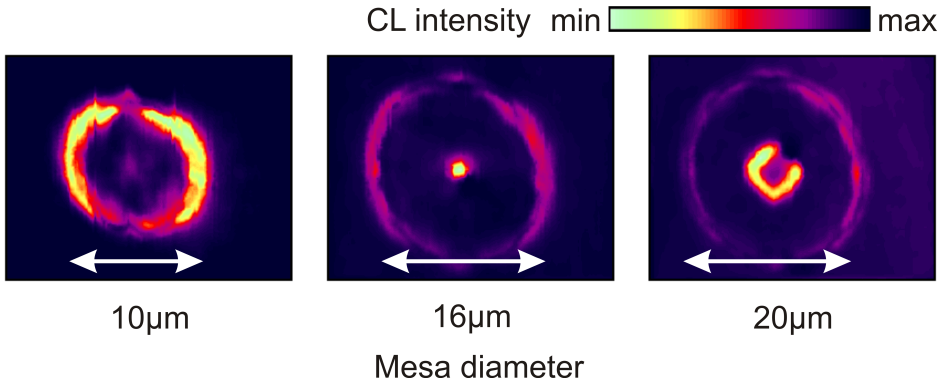

Figure 5.10: CLSIs of mesa structures with increasing mesa diameter showing integrated CL intensity for detection energies of 1.25 - 1.37 eV. CL spectra were measured with a spectral resolution of 560 µeV (30 µm slit, grating 300 lines per mm).

alignment on the size of the aperture. To verify this experimentally, mesa of diameters of 10 µm, 16 µm, and 20 µm were investigated. Due to the same oxidation time these mesa structures have following aperture sizes: 0 (the stressor layer is fully oxidized), 0.9 µm and 2 µm respectively. Figure 5.10 shows the CLSIs of integral intensity distribution for these mesa structures, displayed for detection energies between 1.25 eV and 1.37 eV. All three mesa show the intense luminescence of high-energy QDs on the edge of the mesa. No other areas of intense QD luminescence were found in the mesa structure with fully oxidized stressor. A high intensity of luminescence of high-energy QDs at the center shows up for a mesa diameter of 16 µm, which turns into a square-like pattern for a diameter of 20 µm.

The areas of intense QD luminescence in CLSIs, correlated with aperture size and position, agree very well with the theoretical predictions and AFM investigations of the uncapped QDs (figure 5.7).

5.4.2 Quantum dot luminescence bands

Figure 5.11 shows the CLWI for the emission energies 1.24 -1.35 eV ("high-energy

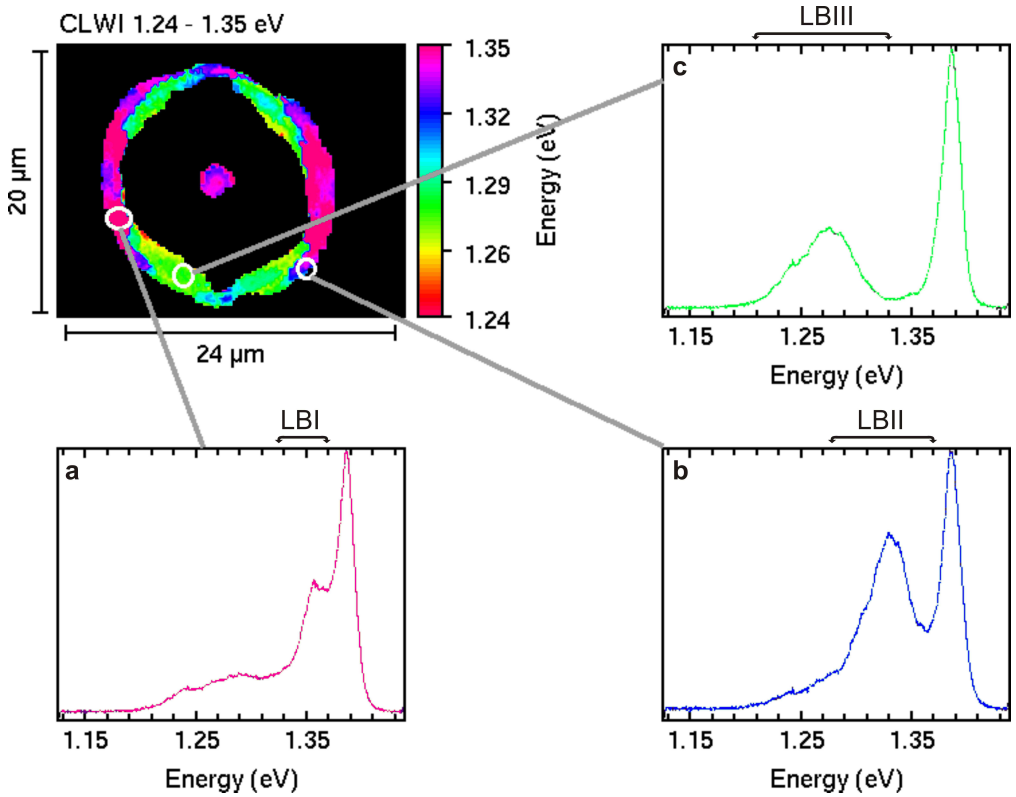

Figure 5.11: CLWI for the emission energies 1.24 -1.35 eV, for the mesa of diameter of 16 µm. The different QD luminescence bands are well spatially separated. Single integral spectra are extracted for particular sites, showing the QD luminescence bands LB I (a), LB II (b), LB III (c). CL spectra were measured with the spectral resolution of 560 µeV (30 µm slit, grating 300 lines per mm). The areas with the luminescence of low SNR are blacked out.

QDs" in the previous section), obtained from CLSI for the mesa structure with a diameter of 16 µm, shown in figure 5.8. Spatially well-separated areas of QD luminescence at different emission energies are eye-catching in the figure. For a number of these areas, CL spectra, integrated over the region of ~ 1 µm^2, are obtained and shown ibid. These spectra reveal different QD luminescence bands: LB I (centered at 1.35 eV, FWHM - 30 meV, figure 5.11 a), LB II (centered at 1.33 eV, FWHM - 50 meV, figure 5.11 b) and LB III (centered at 1.27 eV, FWHM - 60 meV, figure 5.11 c).

The knowledge about spatial distribution of high- and low-energy QD luminescence, described in the previous section, can be enlarged. To analyze the dependence of

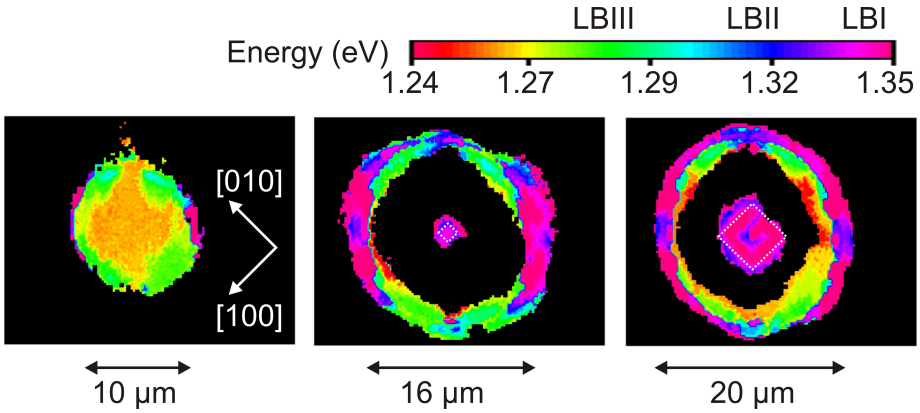

Figure 5.12: CLWI for the emission energies 1.24 -1.35 eV for the mesa structures of diameters of 10 m, 16 µm and 20 µm. LB I, LB II and LB III exhibit a clear site-dependence. Crystallographic directions are the same for all the structures and are marked with white arrows. Aperture boundaries are roughly indicated by white dashed lines. CL spectra were measured with a spectral resolution of 560 µeV (30 µm slit, grating 300 lines per mm). The areas of luminescence with low SNR are blacked out.

the QD luminescence on the size and position of the mesa structure, the CLWIs were obtained from CLSIs in figure 5.10. LB I, LB II, LB III can be well identified on the resulting CLWIs, displayed in figure 5.12.

The low-energy tail of LB III is detected over the AlO_x-area already for the fully-oxidized stressor layer (red-yellow colors in figure 5.12). On the edge of the mesa structures areas of LB III show a distinct four-fold symmetrical alignment (green color). LB I (magenta color) and LB II (blue color) of very weak intensity are observed on the edge for the mesa diameter of 10 µm. For larger diameters the areas of luminescence of both types become larger and the luminescence intensity stronger. On the edge distribution of LB II exhibits an eight-fold symmetry and of LB I - a two-fold symmetry.

Intense luminescence of the types LB I and LB II is found in the center of the mesa structures with an (Al, Ga)As-aperture. For the mesa diameters of 16 µm and 20 µm, displayed in figure 5.12, the aperture sizes are ~ 1 µm and 2 µm respectively. In the center of these mesa structures LB I is well correlated with the aperture boundary: For the small non-oxidized (Al, Ga)As the luminescence is concentrated in the very center, while for the larger aperture sizes it forms a rectangular shape on the inner part of the aperture boundary (~ 2 µm for the mesa diameter of 20 µm). LB II fringes the luminescence LB I.

Such a symmetrical distribution of the luminescence of different bands correlated with aperture position and size results from strain modulation induced by the buried stressor layer. As described in section 5.2.2, the difference of the lattice constants

between the (Al,Ga)As and AlO_x is responsible for a region of maximum compressive strain on the inner part of the aperture boundary. The volume contraction of the buried stressor layer also leads to increased compressive strain on the edge of the mesa structures. Consequently, two regions of QD alignment are created - on the edge of the mesa and at the borders of the aperture. During QD growth, the modulation of the strain energy influences the deposition of the InGaAs in pronounced correlation with these two regions. Moreover, strain fields have a strong impact on the electronic properties of the QD [Gru95]: e.g. a QD with a higher hydrostatic strain inside has a higher transition energy than a QD of the same size with lower strain fields.

The luminescence bands LB I, LB II, and LB III are distinguished spectrally. However, it is impossible to define the difference of the respective QDs only by their emission energy. Since the strain energy on the GaAs-surface favors growth of InGaAs QDs, ensembles of QDs with different size or In-content possibly grow on different sites of the mesa. The exciton transition energy indeed increases with the decrease of the dot size [Sti99] or In-content [Sch07a]; the exciton emission of a QD is red-shifted to the one of a dot with smaller a base length and the same volume [Sch07a]. Additional information about the luminescence properties of the QDs is needed to determine which parameter (geometry, composition or strain) distinguishes the dots with LB I, LB II or LB III. Additional data on e.g. spectroscopic shifts of biexciton or trion transition energy relative to exciton transition energy could help to clarify the morphological peculiarities of the QDs [Sch09a].

Theoretical predictions suggest that mesa structures with a small aperture size are the best candidates for the controlled growth of a single QD directly in the center of the mesa. Such structures are needed to create single-QD device, e.g. a single-photon source [Loc06, Shi07]. The analysis of site-dependent luminescence of QDs suggests several key points to improve the growth method for site-controlled QDs:

(i) The CL experiments showed, that the QDs still nucleate all over the mesa and that QDs with high densities grow on the edges and over the aperture boundaries. It is therefore important to lower the QD densities, emerging all over on the mesa structure.

(ii) The QDs of different luminescence types are spatially well separated, but the spectral ranges of LB I - LB III overlap. Further optimization of growth conditions should aim at the clearly distinct spectral separation of the luminescence bands. A structure with buried stressor together with spectral filtering of the particular emission energy could result in the desired structure with one or more well-positioned QDs and a certain range of luminescence (see figure 5.12 for e.g. LB I as an example).

In summary, the investigation of the CL from mesa structures with QDs grown on the buried stressor confirmed the feasibility of this QD-positioning approach. The formation of the QDs occurs in correlation with the aperture boundary. The strain in the buried stressor induces formation of different QD ensembles which can be well

distinguished spectrally and spatially.

5.4.3 Spectral diffusion

In many approaches of controlled QD growth with substrate pre-patterning, the etching procedure leads to many defects in the surrounding of a QD. This results in enhanced SD of the QD emission lines, i.e. line broadening, spectral jitter or intensity variation (see section 1.3.2). For assessment of the quality of individual QDs grown with the positioning concept presented above, linewidths of the QD emission lines were measured and SD-behavior was investigated.

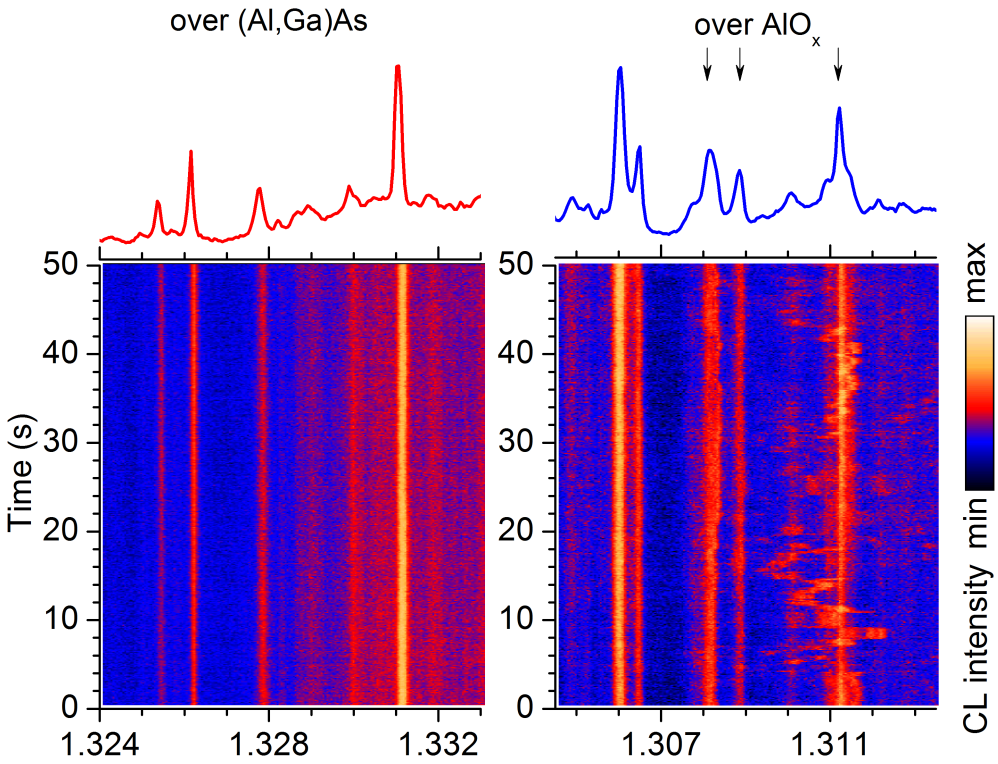

Figure 5.13: SD-patterns and respective single spectra (top), obtained from two sites of the mesa with a large oxidized stressor (diameter 25 µm, aperture size ~7 µm). Left: Measured over the non-oxidized aperture. Right: Measured over oxide-area, arrows indicate lines showing spectral jitter.

Luminescence of the QDs of luminescence types LB I and LB II is detected in the center of mesa sizes in strong correlation with aperture position and size. Closer investigation of the SD-behavior of these QDs is therefore particularly important for the characterization of the growth method. However, the QDs of luminescence type LB I , aligned over the inner parts of the aperture boundaries, exhibit rather high densities. Without further approaches, like e.g. applying a metal mask (section 2.2),

these QDs cannot be examined separately. The excitonic transitions in the spectral range of LB II and LB III could be resolved as spectrally sharp emission lines in the spectra, measured with the best spectral resolution. Thus, the SD-behavior of single dots was investigated only for the QDs with emission energies between 1.27 eV and 1.33 eV.

Some of the typical spectra with individual emission lines were already shown in figure 5.9. The FWHM values of these peaks reveal site-dependence: emission lines of QDs inside the aperture boundaries have a FWHM varying from 170 µeV down to the spectral resolution of the set-up.[3] Similar FWHM values are measured for QDs grown on planar substrates without a stressor layer underneath. In contrast, for the QDs grown above the oxide-area of the stressor layer increased values of FWHM from 190 µeV up to 350 µeV were measured. These larger FWHM suggest, that QDs grown over the (Al,Ga)As have a more defect-free environment compared to the QDs grown over AlO_x. The defects in the material, grown over oxidized regions of stressor layer enhances SD and increases the FWHM of single QD emission lines.

SD-patterns for different sites on the mesa structure were measured (the procedure is described in chapter 3). The obtained intensity-coded graph for two sites on a mesa having a diameter of 25 µm are shown in figure 5.13. For each single spectrum an integration time of 100 ms was set. The emission lines, measured at the center of the mesa (over a non-oxidized site, left panel in the figure), exhibit stable spectral positions and intensity. In contrast to these findings, the spectra measured outside the aperture boundaries over an oxide area of the stressor layer reveal spectral jitter (shown in the right panel in figure 5.13 and indicated with arrows) and on/off blinking for some lines.

For optimization of the growth it is vital to understand, which defects influence the spectral jitter and the line broadening. Since the distance of QDs from the stressor layer is too large, any Stark shift of the excitonic transition energy (see section 1.3) caused by defects in the stressor layer is negligible. The same is valid for the top and side surfaces of the mesa. Impurities, structural and native defects can influence the SD: see the discussion of the nitride-based QDs in chapter 3 and e.g. [Rod06] for SD in InGaAs/GaAs QDs. However, the obvious difference in SD-behavior between the QDs grown over oxidized and non-oxidized areas of the stressor indicates, that more defects originate in GaAs during crystal growth above the area of the AlO_x.

5.4.4 Strain-induced polarization

For polarization-dependent experiments an optical analyzer foil was mounted into a slot in front of the monochromator. To minimize the transmittance characteristics of the monochromator in dependence on the polarization of the detected light, the

[3] In the supplementary experiments on the same samples with µ-PL (not shown here), the QDs exhibit a FWHM of 80 µeV - again the resolution limit of the respective set-up.

linear polarizer foil was placed only in two perpendicular directions with respect to the direction of the polarization of the monochromator. The measurements below were performed with an integration time of 30 ms and for a spectral range between 1.27 eV and 1.33 eV (this energy range is chosen for the same reason as explained in the previous section).

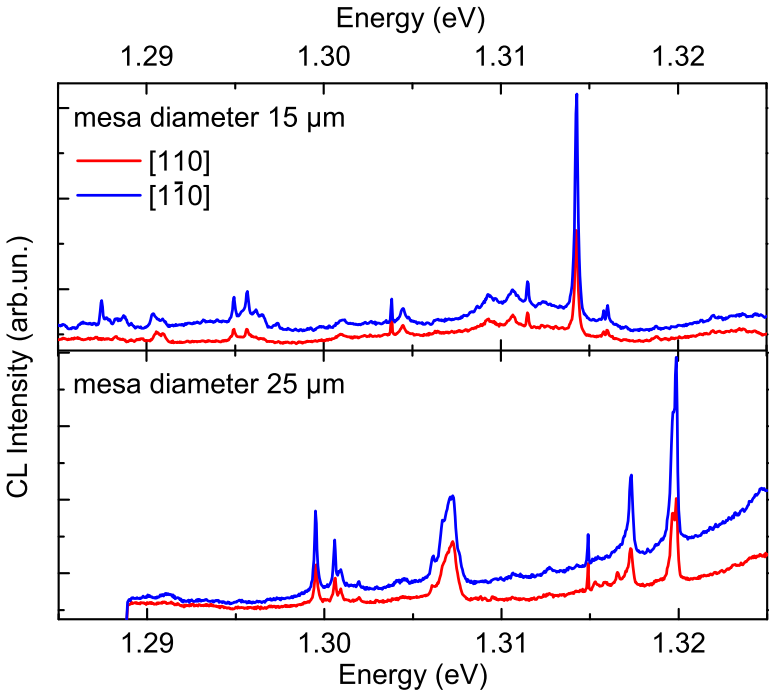

Figure 5.14: Single emission spectra measured for two polarization directions along the [110] and [1$\bar{1}$0] crystallographic axis for QDs in the center of the mesa structures with diameters of 15.5 µm (top panel) and 25 µm (bottom panel).

The QDs grown in the center of the mesa structures showed no spectral jitter, while the QDs grown over the oxide-region of the mesa structures exhibited enhanced SD. If the bright exciton states of the QD have a fine structure splitting (FSS), these states can be resolved in the polarization-dependent measurements as cross-polarized doublets. To exclude energetic shifts of the emission peaks by means of SD, it is helpful to perform measurements on the excitonic lines without jitter. Consequently, only the single QDs in the center of the mesa were investigated with respect to polarization of their emission lines.

The linear polarizer foil was aligned along the [110] and [1$\bar{1}$0] crystallographic directions, since for InGaAs/GaAs QDs the polarization of the emission lines from bright exciton states is parallel to these directions. Figure 5.14 shows spectra for two orientations of the polarizer foil for QDs within the centers of the mesa structures. Mesa structures with either a small aperture size (mesa diameter of 15.5 µm, aperture size 0.8 µm) or a large aperture size (mesa diameter of 25 µm, aperture size 7 µm) were investigated. No doublets of cross-polarized lines could be identified

within the resolution limit of the set-up (the emission lines in the spectra, measured for two polarization directions, coincide in figure 5.14). Using line shape analysis, the difference of the energetic position of single lines could be determined with an accuracy of 30 µeV (see chapter 2).

The absence of cross-polarized doublets in polarization-dependent measurements on single QDs can be explained as follows: either the FSS is less than 30 µeV, or none of the emission lines in the spectra stem from exciton or biexciton. Other excitonic complexes show different polarization characteristics, e.g. charged trions do not exhibit polarization.

Additionally to the individual QDs, polarization properties of the luminescence of

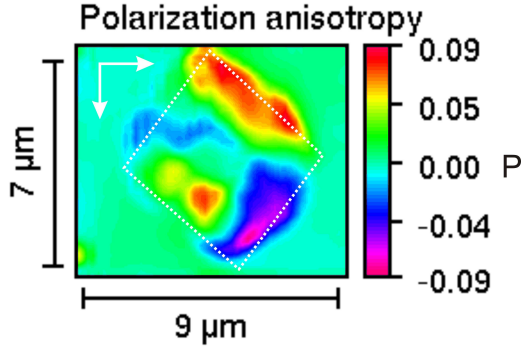

Figure 5.15: Spatial distribution of the polarization degree P of CL, recorded for integral intensities of the QD with emission energies of 1.31 eV-1.36 eV and polarization directions along the [110] and [1$\bar{1}$0], indicated with white arrows. The aperture boundary is approximately marked by a dashed line.

QD ensemble was investigated. For a mesa structure with a large aperture size (mesa diameter of 25 µm) the CLSIs were measured for emission energies of 1.31 eV-1.36 eV in polarization directions along the [110] and [1$\bar{1}$0]. These energies were chosen, because QD luminescence, measured in the center of the mesa, falls in this spectral range (LB I and LB II in figure 5.12). Figure 5.15 shows the spatial distribution of the polarization degree

$$P = \frac{I_{[110]} - I_{[1\bar{1}0]}}{I_{[110]} + I_{[1\bar{1}0]}}$$

where $I_{[110]}$ and $I_{[1\bar{1}0]}$ are the integrated CL intensities, resolved in polarization along [110] and [1$\bar{1}$0] crystallographic directions.

A strong anisotropy is observed for the polarization of QD luminescence over the aperture boundary: Along one side of the rectangle of the aperture luminescence intensity polarized along [110] is larger than the one along [1$\bar{1}$0]: $P > 0$, for the perpendicular side, on the contrary, luminescence intensity polarized along [110] is smaller than the one along [1$\bar{1}$0] $I_{[110]} < I_{[1\bar{1}0]}$. On the remaining parts of the mesa structure no significant polarization is observed.

Various factors can lead to polarization of the QD ensemble: anisotropy of the QD form, material content, or strain in the matrix. E.g. in [Nak02] in polarization-resolved measurements showed that lateral patterning of the matrix with so-called wall-shaped structures resulted in strong optical anisotropy of InGaAs/GaAs. Furthermore, changing the matrix into free-standing air-bridge structures reduced the anisotropy. The excitonic transitions of strong elongated CdTe/CdMgTe QDs in [Bes00] were observed to be linearly polarized along the two orthogonal principal axes of the dot. The effect of composition modulation of polarization of the luminescence of heterostructures was reported for AlAs/InAs short-period super-lattice in [Fra00] and InP/InGaP QDs in [Sug99].

Without further experiments it is impossible to define the decisive reason for polarization anisotropy within the framework of this work. Figure 5.16 schematically shows the deformation of a unit cell of the InGaAs under the influence of compressive strain in GaAs, induced by the buried aperture. Along the perpendicular sides of the boundaries the ratio $\varepsilon_{xx}/\varepsilon_{yy}$ is different. In addition, the significant difference of ad-atom mobilities for different crystallographic directions is responsible for the formation of elongated QDs. QD elongation and strain anisotropy influence the spatial distribution and overlap of the charge carrier wave-functions (e.g. [Seg05, Sch07a]). As a result, different polarization of the QD luminescence is observed for QDs along the perpendicular aperture sides, as shown in figure 5.15.

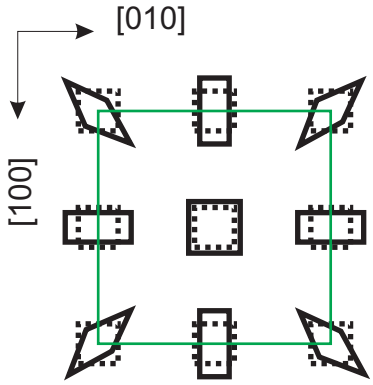

Figure 5.16: Schema of the deformation of the InGaAs unit-cell (solid lines) under the influence of the strain induced by the buried stressor in comparison to the non-strained shape of the unit-cell (dashed line). The green line indicates the aperture boundary.

In the scope of the present work no individual QDs grown along the aperture boundary were investigated. It is, however, possible to speculate about the FSS of the bright exciton states of these dots. The anisotropy of the QD morphology and of the strain in the material results in a reduced potential symmetry of the charge carrier confinement and consequently in non-zero FSS of the bright exciton states. Similar to the site-dependence of the QD ensemble polarization, there should be a correlation between the excitonic FSS value and the QD position relative to the

aperture. Moreover, monotonous change of the strain components along the aperture boundary (figure 5.16) can result in monotonous variation of the excitonic FSS. If for some dot the external strain together with the piezoelectric potential of the InGaAs/GaAs QD result in C4v symmetry of the confinement potential, the excitonic FSS is zero for this dot. This strongly suggests that the proposed growth approach is a promising method to produce QDs with desirable FSS.

Conclusion

By the CL experiments, a novel technique for the site-controlled growth was proved. The method was applied to grow QDs in the technologically important InGaAs/GaAs material system. The principle of the method relies on the modulation of the strain energy of the surface, on which the QDs are grown. The modulation is created by a buried stressor. In the present work the stressor layer is formed by partial oxidation of an (Al,Ga)As layer underneath the GaAs in an etched mesa structures. The calculation of the strain distribution on the GaAs surface predict the growth of the QDs above the inner regions of the boundary of non-oxidized (Al,Ga)As region as a result of the minimization of the surface free energy during growth of QD layer.

The characterization of optical properties of the QDs in the first test-structures, grown with the method described was performed by CL. In these investigations CL has been proven as the method of choice due to its large spatial and spectral resolution. Strong influence of the buried stressor on the growth and luminescence properties of the overgrown heterostructures was observed. In contrast to the formation of QDs with small areal density over the whole mesa, two regions of nucleation of QDs were identified on the boundaries of the apertures and edges of the mesa structure. Here growth of QDs is triggered by the strain in the buried stressor, which leads to the self-organized formation of QDs with a high areal density.

The luminescence of the QDs in the areas of a high-density growth decomposes into three distinct bands, which can be distinguished spectrally and spatially. The strain modulation due to volume contraction in the stressor layer results in anisotropic InGaAs deposition during the QD growth and may lead to formation of QDs with different In-content, aspect ratio and size. The QDs, grown in this structures, experience anisotropic strain distribution, induced by the stressor. As a result QDs of different emission energies correlated to position on the mesa are observed. Also, anisotropic strain distribution results in a strong polarization anisotropy of QD ensemble luminescence of the QDs grown along the sides of the aperture boundaries.

When spectrally resolved, the QD luminescence on the areas with low dot densities disintegrates into sharp emission lines. Site-dependence of the SD of emission lines of individual QDs indicates enhanced formation of defects in the GaAs above the oxidized regions of the stressor layer. Best FWHMs (170 µeV down to resolution of the set-up), stable spectral positions and intensities were found only for the individual QDs in the center of the mesa structures over the (Al,Ga)As region. These characteristics are similar to the self-assembled QDs, grown without a buried stressor. Therefore, the new approach allows for growth of the QDs with good optical quality.

Mesa structures with very small apertures ($\leq$ 1 µm) seem best suited to further develop test-structures resulting in a single QD in the center of the mesa. The CL investigations of test-structures suggest the key issues for further growth optimization: QD densities, formed all over on the mesa structure, should be lowered, or the

QDs aligned on the aperture boundaries should be better separated spectrally.

Summary and outlook

Summary

This work presents the results of the investigation of the optical properties of nitride-based and arsenide-based quantum dots (QDs) by means of cathodoluminescence (CL) spectroscopy. Both QD material systems are vital for quantum-communication and solid-state quantum computing systems. Nitride-based QDs are promising candidates for the development of single-QD applications functioning at elevated temperatures. The InGaAs/GaAs QD material system was chosen for the present investigation to verify a new method of controlled QD growth. Development of new approaches of deterministic positioning of QDs with desirable optical properties is of tremendous importance for tailoring single QD-devices. In the investigations CL has been proven as the method of choice due to its large spatial and spectral resolution combined with the possibility to directly image topographic structures of the sample surface by means of conventional SEM imaging.

Charge trapping and release processes in the vicinity of a QD influence the QD excitonic emission. This effect - so-called spectral diffusion of single-QD luminescence (SD) - can be detrimental for the performance of single-QD based devices, which require stable spectral position and intensity of the single QD emission line. Pyro- and piezoelectric effects result in huge built-in fields in nitride-based heterostructure and cause a significant spatial separation of the electron and the hole wave-functions. The created electrostatic dipole moment makes the nitride-based QDs particularly sensitive to local electric field fluctuations, induced by defects. Therefore, SD was thoroughly investigated in the present work on the example of nitride-based QDs.

In the present work it was shown, that SD is composed of different components, which exhibit significantly different timescales. Different mechanisms originate each of the components. The analysis of the dependence of SD on various excitation conditions and sample fabrication methods allowed to conclude which defect types are responsible for each type of SD and what are the way to possibly eliminate the negative effects of SD. Large emission linewidths, as a result of fast spectral jitter, appear to be an intrinsic property of the nitride-based QD material system in the current fabrication methods and cannot be avoided even by the resonant excitation of the QD. In contrast, the slow spectral jitter is induced only in non-resonant excitation. The phenomenon of luminescence intermittence of the emission lines is related to a defect, specific for certain growth procedure (in the present work - growth with metal-organic vapor deposition) or impurity concentrations. However, such effect of on/off blinking can be reduced by means of post processing, like e.g.

thermal annealing.

The investigation of slow spectral jitter revealed aspects of fundamental importance. A specific pattern of the oscillation of single-QD emission lines, the so-called χ-pattern, was reported for the first time. This pattern allows to obtain absolute values of the built-in dipole moment of excitonic complexes of the investigated QDs without applying an external electric field. Also, a model of a moving charge, suggested to explain these patterns, can be generalized for the slow spectral jitter in nitride-based QDs. For the first time the ratio of the built-in dipole moments of excitonic complexes of the same dot were determined quantitatively from the characteristic shifts of the emission lines, stemming from the same QD. Built-in dipole moments of various excitonic complexes from the same dot were shown to differ significantly.

The interaction of excitons confined in the dots with acoustic phonons increases at elevated temperatures and coupling to phonons can be a limiting factor for QD-applications, requiring strong coherence of the exciton state. Therefore, another focus of the work was placed onto investigation of the interactions of excitons in GaN/AlN QDs with lattice vibrations. Temperature-dependent CL experiments on the single QDs revealed enhanced coupling to acoustic phonons, much stronger than observed e.g. in arsenide-based QDs.

Theoretical modeling performed in the frames of this work accounts very well for the experimental observations of the shape and position of the phonon side-bands. The analysis of the impact of the QD geometry on the exciton acoustic-phonon coupling mechanisms revealed the enhanced role of piezoelectric coupling for this QD material system. As a result, the acoustic-phonon side-bands scale together with the built-in dipole-moment. As was shown in [Kru05b] increased piezoelectric coupling to phonons enhances the dephasing of exciton state, the interaction with acoustic phonons can therefore become an obstacle for utilization of nitride-based QDs.

The CL spectroscopy proved to be the most useful tool for the characterization of the optical properties of QDs in test-structures, grown using a new method of controlled QD alignment. The feasibility of the growth concept was proven on the example of InGaAs/GaAs QD material system. The unambiguous influence of the strain from the buried stressor structure on luminescence properties, such as spectral diffusion and ensemble polarization, was evidenced in CL experiments. Single QDs, grown with the new method show a good optical quality, comparable with the self-assembled QDs, grown by conventional methods. The formation of different spectrally distinguishable QD luminescence bands was revealed. These bands are located in strong correlation with the stressor position. These site-dependent luminescence properties prove the possibility to control fundamental QD properties and formation by means of strain from a buried stressor structure. Also, the CL experiments suggested the key issues for further growth optimization: lowering of QD densities or spectral separation of the QD luminescence bands.

Outlook

Despite new knowledge gained in the frames of the present work, in the field of the investigated QD systems there remain further problems to be solved. Also, new questions arose during this work. Some ideas for further complementing experiments are listed below.

The investigation of fundamental optical properties of single GaN/AlN QDs should be continued. The fingerprint of the single QD luminescence can be exploited for deciphering the QD spectrum. Polarization-dependent measurements should be performed as a next step. Linear polarized luminescence of GaN/AlN has been often reported for the single GaN/AlN QDs [Bar08, Kin09, Aml11] and is usually attributed to valence band mixing effects [Bar08, Win08]. A thorough experiments on polarization characteristics and investigation of fine structure splitting is of particular importance for applications of nitride-based QDs as single- or entangled photon sources.

Since one and the same mesa can be investigated in cathodoluminescence (CL) and micro-photoluminescence (µPL) spectroscopy, combined experiments with both techniques can be performed on a single QD in a sample processed as mesa structures. Lines stemming from the same QD can be identified from SD-patterns by means of CL excitation. The dependence of the QD luminescence on the excitation density and polarization of excitation light can be then measured by means of µPL. Polarization-dependent measurements of QD emission lines is possible to obtain with either of the techniques. As a result the origin of the emission lines can be identified.

Influence of acoustic phonons on stable single-photon emission up to elevated temperatures should be investigated further. Experiments revealing the dephasing time in nitride-based QDs are of particular importance for the quantum computing applications. Also, experimental and theoretical investigation of coupling between the optical phonons and excitons in QDs is needed to substantiate the knowledge about exciton-phonon interaction in GaN/AlN QDs.

In the investigations of SD the built-in dipole moment of the different excitonic (multi)complexes were found to differ significantly. Since the exitonic dipole-moment influences the piezo-electric coupling to acoustic phonons, it can result in significantly different acoustic-phonon coupling to these complexes and different dephasing due to phonons. A thorough modeling of the exciton-phonon interaction is necessary to explore and, probably, exploit this fact.

Non-polar nitride QDs is another interesting QD material system for further investigations [Dau08]. Since the huge built-in field should be absent in these heterostructures, it is important to investigate spectral diffusion issues and interaction with lattice vibrations in this material system as well.

The development of the proposed approach of QD positioning appears feasible and should be continued further. Several key points to improve the growth method were suggested, based on the CL experiments on the first test-structures. Reduction of the QD densities or distinct spectral separation of the luminescence bands is needed. Also, a different stressor shape might be exploited.

Applying a shadow mask to the existing mesa structures with site-controlled InGaAs/GaAs QDs and performing single-dot spectroscopy could be employed to investigate the optical properties of these novel QDs for a complete comparison to conventional self-assembled QDs. Information about fine structure splitting of the excitonic states of these QD is important for the further implementation of these structures for quantum information applications.

Appendix

Acknowledgments

I want to express my deep gratitude to Prof. Dr. Dieter Bimberg for managing my PhD Thesis. I appreciate this great opportunity to learn much during the years of work in his group.

I am greatly indebted to Prof. Dr. Axel Hoffmann for his steady support and guidelines.

I thank Prof. Yasuhiko Arakawa and Prof. Nicolas Grandjean for providing interesting samples for the investigations.

Countless thanks to Dr. Sven Rodt for all the years of supervising me and advising, how to cope with CL-lab, physics, computers and people. Dr. Volker Türck I thank for valuable support in interpretation of the main results. I am very much obliged to both of them for critical reading of the current work.

I thank Dr. Andrei Schliwa, Gerald Hönig and Matthias-René Dachner for their calculations, and for their patience to explain me everything all over again. Dr. Christian Kindel I thank for introducing me into the nitride-world. I thank Dr. Andrei Schliwa for enthusiasm and wise advises. I also thank Dr. André Strittmatter and the TU growth team for the sample growth. I am grateful to Dr. Erik Stock among other things for his help with thesis layout. I acknowledge Dr. Robert Seguin for kind introduction to the lab and QD-field.

I am grateful to Dr. María Machón and Svenja Neupert for help with self-management. I am also indebted to the TU-Frauenbeauftragten and ProMotion for the support in the last part of my PhD study.

I thank all former and present members of AG Bimberg and SFB 787 for very pleasant work atmosphere.

I appreciate all support and encouragement of my friends and family. I am very grateful to Gisela Türck for correcting my English.

I will be always grateful to my father for showing me the door into the world of physics and to V. V. Ptschoelkin for opening it. I gratefully acknowledge my University for those marvelous years and education in physics.

I thank Volker at least for all his three roles during writing of the thesis and for all his help and encouragement.

Abbreviations

0D	zero-dimensional (for 1D, 2D, 3D one-/two-/three-dimensional respectively)
µPL	micro-photoluminescence
AFM	atomic force microscopy
CL	cathodoluminescence
CLSI	cathodoluminescence spectra images
CLWI	cathodoluminescence wavelength images
def	deformation potential (coupling)
FSS	fine structure splitting
FWHM	full width at half maximum
LA	longitudinal acoustic (phonons)
MBE	molecular beam epitaxy
ML	monolayer
MOCVD	metal-organic chemical vapor deposition
piezo	piezo-electrical (coupling)
QCSE	quantum confined Stark effect
QD	quantum dot
QW	quantum well
RT	room temperature
SD	spectral diffusion
SEM	scanning electron microscope
S-K	Stranski-Krastanow (growth mode)
SNR	signal to noise ratio
TA	transverse acoustic (phonons)
TEM	transmission electron microscopy
WL	wetting layer

X (XX)	exciton (biexciton)
X-aP	exciton-acoustic phonon (coupling/interaction etc.)
ZPL	zero-phonon line

Bibliography

[Abb08] M. Abbarchi, F. Troiani, C. Mastrandrea, G. Goldoni, T. Kuroda, T. Mano, K. Sakoda, N. Koguchi, S. Sanguinetti, A. Vinattieri and M. Gurioli. Applied Physics Letters **93**, 162101 (2008).

[Ama89] H. Amano, M. Kito, K. Hiramatsu and I. Akasaki. Japanese Journal of Applied Physics **28**, L2112 (1989).

[Aml11] S. Amloy, K. H. Yu, K. F. Karlsson, R. Farivar, T. G. Andersson and P. O. Holtz. Applied Physics Letters **99**, 251903 (2011).

[And00] A. D. Andreev and E. P. O'Reilly. Physical Review B **62**, 15851 (2000).

[And01] A. D. Andreev and E. P. O'Reilly. Applied Physics Letters **79**, 521 (2001).

[Ape95] R. Apetz, L. Vescan, A. Hartmann, C. Dieker and H. Lüth. Applied Physics Letters **66**, 445 (1995).

[Ara82] Y. Arakawa and H. Sakaki. Applied Physics Letters **40**, 939 (1982).

[Atk08] P. Atkinson, S. Kiravittaya, M. Benyoucef, A. Rastelli and O. G. Schmidt. Applied Physics Letters **93**, 101908 (2008).

[Bar04] T. Bartel, M. Dworzak, M. Strassburg, A. Hoffmann, A. Strittmatter and D. Bimberg. Applied Physics Letters **85**, 1946 (2004).

[Bar06] R. Bardoux, T. Guillet, P. Lefebvre, T. Taliercio, T. Bretagnon, S. Rousset, B. Gil and F. Semond. Physical Review B **74**, 195319 (2006).

[Bar07] T. P. Bartel, P. Specht, J. C. Ho and C. Kisielowski. Philosophical Magazine **87**, 1983 (2007).

[Bar08] R. Bardoux, T. Guillet, B. Gil, P. Lefebvre, T. Bretagnon, T. Taliercio, S. Rousset and F. Semond. Physical Review B **77**, 235315 (2008).

[Bay02a] M. Bayer and A. Forchel. Physical Review B **65**, 041308 (2002).

[Bay02b] M. Bayer, G. Ortner, O. Stern, A. Kuther, A. Gorbunov, A. Forchel, P. Hawrylak, S. Fafard, K. Hinzer, T. Reinecke, S. Walck, J. Reithmaier, F. Klopf and F. Schäfer. Physical Review B **65**, 195315 (2002).

[Ben00] O. Benson, C. Santori, M. Pelton and Y. Yamamoto. Physical Review Letters **84**, 2513 (2000).

[Ber97] F. Bernardini, V. Fiorentini and D. Vanderbilt. Physical Review B **56**, R10024 (1997).

[Ber99] D. Bertram, M. C. Hanna and A. J. Nozik. Applied Physics Letters **74**, 2666 (1999).

[Ber06] A. Berthelot, I. Favero, G. Cassabois, C. Voisin, C. Delalande, Ph. Roussignol, R. Ferreira and J.-M. Gérard. Nature Physics **2**, 759 (2006).

[Bes00] L. Besombes, K. Kheng and D. Martrou. Physical Review Letters **85**, 425 (2000).

[Bes01] L. Besombes, K. Kheng, L. Marsal and H. Mariette. Physical Review B **63**, 155307 (2001).

[Bes02] L. Besombes, K. Kheng, L. Marsal and H. Mariette. Physical Review B **65**, 121314 (2002).

[Bim97] D. Bimberg, N. Kirstaedter, N.N. Ledentsov, Zh. I. Alferov, P. S. Kop'ev and V. M. Ustinov. IEEE Journal of Selected Topics in Quantum Electronics **3**, 196 (1997).

[Bim98] D. Bimberg, M. Grundmann and N.N. Ledentsov. *Quantum Dot Heterostructures*. 1st Edition. (John Wiley and Sons, Inc., 1998).

[Bim05] D. Bimberg. Journal of Physics D: Applied Physics **38**, 2055 (2005).

[Bim09] D. Bimberg, E. Stock, A. Lochmann, A. Schliwa, J. A. Töfflinger, W. Unrau, M. Munnix, S. Rodt, V. A. Haisler, A. I. Toropov, A. K. Bakarov and A. K. Kalagin. IEEE Photonics Journal **1**, 58 (2009).

[Bir01] D. Birkedal, K. Leosson and J. Hvam. Physical Review Letters **87**, 227401 (2001).

[Blo00] P. Blome, M. Wenderoth, M. Hübner, R. Ulbrich, J. Porsche and F. Scholz. Physical Review B **61**, 8382 (2000).

[Bor01] P. Borri, W. Langbein, S. Schneider, U. Woggon, R. Sellin, D. Ouyang and D. Bimberg. Physical Review Letters **87**, 157401 (2001).

[Bra00] M. Braskén, M. Lindberg, D. Sundholm and J. Olsen. Physical Review B **61**, 7652 (2000).

[Bra05] P.-F. Braun, X. Marie, L. Lombez, B. Urbaszek, T. Amand, P. Renucci, V. K. Kalevich, K. V. Kavokin, O. Krebs, P. Voisin and Y. Masumoto. Physical Review Letters **94**, 116601 (2005).

[Bre03] T. Bretagnon, S. Kalliakos, P. Lefebvre, P. Valvin, B. Gil, N. Grandjean, A. Dussaigne, B. Damilano and J. Massies. Physical Review B **68**, 205301 (2003).

[Bre06] T. Bretagnon, P. Lefebvre, P. Valvin, R. Bardoux, T. Guillet, T. Taliercio, B. Gil, N. Grandjean, F. Semond, B. Damilano, A. Dussaigne and J. Massies. Physical Review B **73**, 113304 (2006).

[Car10] A. Carmele, F. Milde, M.-R. Dachner, M. B. Harouni, R. Roknizadeh, M. Richter and A. Knorr. Physical Review B **81**, 195319 (2010).

[Cha89] D. J. Chadi and K. J. Chang. Physical Review B **39**, 10063 (1989).

[Cha97] D. J. Chadi and H. Park. Physical Review B **55**, 12995 (1997).

[Cho97] K. D. Choquette, K. M. Geib, C. I. H. Ashby, R. D. Twesten, O. Blum, H. Q. Hou, D. M. Follstaedt, B. E. Hammons, D. Mathes and R. Hull. IEEE Journal of Selected Topics in Quantum Electronics **3**, 916 (1997).

[Chr91] J. Christen, M. Grundmann and D. Bimberg. Journal of Vacuum Science & Technology B: Microelectronics and Nanometer Structures **9**, 2358 (1991).

[Dal10] D. Dalacu, M.E. Reimer, S. Fréderick, D. Kim, J. Lapointe, P.J. Poole, G.C. Aers, R.L. Williams, W. Ross McKinnon, M. Korkusinski and P. Hawrylak. Laser Photonics Reviews **4**, 283 (2010).

[Dam99] B. Damilano, N. Grandjean, F. Semond, J. Massies and M. Leroux. Applied Physics Letters **75**, 962 (1999).

[Dau97] B. Daudin, F. Widmann, G. Feuillet, Y. Samson, M. Arlery and J. L. Rouvie. Physical Review B **56**, 7069 (1997).

[Dau98] B. Daudin, F. Widmann, J. Simon, G. Feuillet, J. L. Rouviere, N. T. Pelekanos and G. Fishman. Piezoelectric Properties of GaN Self-Organized Quantum Dots. Band 537, Seite G9.2, MRS Proceedings, 1998.

[Dau08] B. Daudin. Journal of Physics: Condensed Matter **20**, 473201 (2008).

[DB68] B. Di Bartolo. *Optical Interactions in Solids*. 1st Edition. (John Wiley and Sons, Inc., 1968).

[De 02] S. De Rinaldis, I. D'Amico, E. Biolatti, R. Rinaldi, R. Cingolani and F. Rossi. Physical Review B **65**, R081309 (2002).

[Dem09] F. Demangeot, D. Simeonov, A. Dussaigne, R. Butte and N. Grandjean. Physica Status Solidi (c) **6**, S598 (2009).

[Emp96] S. A. Empedocles, D. J. Norris and M. G. Bawendi. Physical Review Letters **77**, 3873 (1996).

[Erl02] S. I. Erlingsson and Y. V. Nazarov. Physical Review B **66**, 155327 (2002).

[Faf00] S. Fafard. Applied Physics Letters **76**, 2707 (2000).

[Fan98] X. Fan, T. Takagahara, J. E. Cunningham and H. Wang. Solid State Communications **108**, 857 (1998).

[Fav03] I. Favero, G. Cassabois, R. Ferreira, D. Darson, C. Voisin, J. Tignon, C. Delalande, G. Bastard, Ph. Roussignol and J.-M. Gérard. Physical Review B **68**, 233301 (2003).

[Fav07] I. Favero, A. Berthelot, G. Cassabois, C. Voisin, C. Delalande, Ph. Roussignol, R. Ferreira and J.-M. Gérard. Physical Review B **75**, 073308 (2007).

[Fel09] M. Felici, P. Gallo, A. Mohan, B. Dwir, A. Rudra and E. Kapon. Small (Weinheim an der Bergstrasse, Germany) **5**, 938 (2009).

[Fon03] V. A. Fonoberov and A. A. Balandin. Journal of Applied Physics **94**, 7178 (2003).

[För03] J. Förstner, C. Weber, J. Danckwerts and A. Knorr. Physica Status Solidi (b) **238**, 419 (2003).

[Fra00] S. Francoeur, Y. Zhang, A. G. Norman, F. Alsina, A. Mascarenhas, J. L. Reno, E. D. Jones, S. R. Lee and D. M. Follstaedt. Applied Physics Letters **77**, 1765 (2000).

[Fry00] P. W. Fry, I. E. Itskevich, D. J. Mowbray, M. S. Skolnick, J. Finley, J. Barker, E. P. O'Reilly, L. R. Wilson, I. A. Larkin, P. A Maksym, M. Hopkinson, M. Al-Khafaji, J. P. David, A. G. Cullis, G. Hill and J. C. Clark. Physical review letters **84**, 733 (2000).

[Gal08] P. Gallo, M. Felici, B. Dwir, K. A. Atlasov, K. F. Karlsson, A. Rudra, A. Mohan, G. Biasiol, L. Sorba and E. Kapon. Applied Physics Letters **92**, 263101 (2008).

[Gis02] N. Gisin, G. Ribordy, W. Tittel and H. Zbinden. Reviews of Modern Physics **74**, 145 (2002).

[Gol85] L. Goldstein, F. Glas, J. Y. Marzin, M. N. Charasse and G. Le Roux. Applied Physics Letters **47**, 1099 (1985).

[Gol04] V. N. Golovach, A. Khaetskii and D. Loss. Physical Review Letters **93**, 016601 (2004).

[Göt95] W. Götz, N. M. Johnson, R. A. Street, H. Amano and I. Akasaki. Applied Physics Letters **66**, 1340 (1995).

[Gra09] T. Grange. Physical Review B **80** (2009).

[Gru95] M. Grundmann, O. Stier and D. Bimberg. Physical Review B **52**, 11969 (1995).

[Hak10] T. V. Hakkarainen, J. Tommila, a. Schramm, a. Tukiainen, R. Ahorinta, M. Dumitrescu and M. Guina. Applied Physics Letters **97**, 173107 (2010).

[Har97] A. Hartmann, L. Loubies, F. Reinhardt and E. Kapon. Applied Physics Letters **71**, 1314 (1997).

[Har99] A. Hartmann, Y. Ducommun, K. Leifer and E. Kapon. Journal of Physics: Condensed Matter **11**, 5901 (1999).

[Hei96] R. Heitz, M. Grundmann, N. N. Ledentsov, L. Eckey, M. Veit, D. Bimberg, V. M. Ustinov, A. Yu. Egorov, A. E. Zhukov, P. S. Kop'ev and Zh. I. Alferov. Applied Physics Letters **68**, 361 (1996).

[Hei99] R. Heitz, I. Mukhametzhanov, O. Stier, A. Madhukar and D. Bimberg. Physical Review Letters **83**, 4654 (1999).

[Hen07] K. Hennessy, A. Badolato, M. Winger, D. Gerace, M. Atatüre, S. Gulde, S. Fält, E. L. Hu and A. Imamoglu. Nature **445**, 896 (2007).

[Hög04] A. Högele, S. Seidl, M. Kroner, K. Karrai, R. Warburton, B. Gerardot and P. M. Petroff. Physical Review Letters **93**, 217401 (2004).

[Hoh07] U. Hohenester, G. Pfanner and M. Seliger. Physical Review Letters **99**, 047402 (2007).

[Hos04] K. Hoshino, S. Kako and Y. Arakawa. Applied Physics Letters **85**, 1262 (2004).

[Hua50] K. Huang and A. Rhys. In *Proc. R. Soc.*, vol. 204, p. 406, London, ser A, 1950.

[Hug11] A. Huggenberger, S. Heckelmann, C. Schneider, S. Höfling, S. Reitzenstein, L. Worschech, M. Kamp and A. Forchel. Applied Physics Letters **98**, 131104 (2011).

[Jai00] S. C. Jain, M. Willander, J. Narayan and R. Van Overstraeten. Journal of Applied Physics **87**, 965 (2000).

[Joh08] R. Johne, N. Gippius, G. Pavlovic, D. Solnyshkov, I. Shelykh and G. Malpuech. Physical Review Letters **100**, 240404 (2008).

[Kak03] S. Kako, M. Miyamura, K. Tachibana, K. Hoshino and Y. Arakawa. Applied Physics Letters **83**, 984 (2003).

[Kak04] S. Kako, K. Hoshino, S. Iwamoto, S. Ishida and Y. Arakawa. Applied Physics Letters **85**, 64 (2004).

[Kak05] S. Kako. *Optical Properties of Gallium Nitride Self-Assembled Quantum Dots and Application to Generation of Non-Classical Light*. PhD in physics, Department of Advanced Interdisciplinary Studies, The University of Tokyo, Japan, 2005.

[Kak06] S. Kako, C. Santori, K. Hoshino, S. Götzinger, Y. Yamamoto and Y. Arakawa. Nature materials **5**, 887 (2006).

[Kam98] I. Kamiya. Physica E: Low-dimensional Systems and Nanostructures **2**, 637 (1998).

[Kam02] C. Kammerer, C. Voisin, G. Cassabois, C. Delalande, Ph. Roussignol, F. Klopf, J. Reithmaier, A. Forchel and J.-M. Gérard. Physical Review B **66**, 041306 (2002).

[Kan72] K Kanaya and S Okayama. J. Phys. D **5** (1972).

[Kel04] R. R. Keller, A. Roshko, R. H. Geiss, K. A. Bertness and T. P. Quinn. Microelectronic Engineering **75**, 96 (2004).

[Kha00] A. V. Khaetskii and Y. V. Nazarov. Physical Review B **61**, 12639 (2000).

[Kha02] A. Khaetskii, D. Loss and L. Glazman. Physical Review Letters **88**, 186802 (2002).

[Kim99] J. Kim, O. Benson, H. Kan and Y. Yamamoto. Nature **397**, 500 (1999).

[Kin09] C. Kindel, S. Kako, T. Kawano, H. Oishi and Y. Arakawa. Japanese Journal of Applied Physics **48**, 04C116 (2009).

[Kin10a] C. Kindel, S. Kako, T. Kawano, H. Oishi, Y. Arakawa, G. Hönig, M. Winkelnkemper, A. Schliwa, A. Hoffmann and D. Bimberg. Physical Review B **81**, 241309 (2010).

[Kin10b] C. H. Kindel. *Study on Optical Polarization in Hexagonal Gallium Nitride Quantum Dots*. PhD thesis, University of Tokyo, Japan, 2010.

[Kom00] S. Komiyama, O. Astafiev, V. Antonov, T. Kutsuwa and H. Hirai. Nature **403**, 405 (2000).

[Kow05] K. Kowalik, O. Krebs, A. Lemaitre, S. Laurent, P. Senellart, P. Voisin and J. A. Gaj. Applied Physics Letters **86**, 041907 (2005).

[Kre74] H. Kressel and H. F. Lockwood. J. Phys. Colloques (Paris) **35**, C3–223 (1974).

[Kri03] S. Krishnamurthy, M. van Schilfgaarde and N. Newman. Applied Physics Letters **83**, 1761 (2003).

[Kri05] S. Krishna, D. Forman, S. Annamalai, P. Dowd, P. Varangis, T. Tumolillo, A. Gray, J. Zilko, K. Sun, M. Liu, J. Campbell and D. Carothers. Applied Physics Letters **86**, 193501 (2005).

[Kru02] B. Krummheuer, V. Axt and T. Kuhn. Physical Review B **65**, 195313 (2002).

[Kru05a] B. Krummheuer, V. Axt and T. Kuhn. Physical Review B **72**, 245336 (2005).

[Kru05b] B. Krummheuer, V. Axt, T. Kuhn, I. D'Amico and F. Rossi. Physical Review B **71**, 235329 (2005).

[Kry07] M. Kryśko, G. Franssen, T. Suski, M. Albrecht, B. Lucznik, I. Grzegory, S. Krukowski, R. Czernecki, S. Grzanka, I. Makarowa, M. Leszczynski and P. Perlin. Applied Physics Letters **91**, 211904 (2007).

[Kur07] T. Kuroda, Y. Sakuma, K. Sakoda, K. Takemoto and T. Usuki. Applied Physics Letters **91**, 223113 (2007).

[Lag08] D. Lagarde, A. Balocchi, H. Carrère, P. Renucci, T. Amand, X. Marie, S. Founta and H. Mariette. Physical Review B **77**, R041304 (2008).

[Lan04] W. Langbein, P. Borri and U. Woggon. Physical Review B **69**, 161301 (2004).

[Led08] N. N. Ledentsov, D. Bimberg and Zh. I. Alferov. J. Lightwave Technol. **26**, 1540 (2008).

[Lee01] H. Lee, J. A. Johnson, M. Y. He, J. S. Speck and P. M. Petroff. Applied Physics Letters **78**, 105 (2001).

[Lee11] J. Lee, T. W. Saucer, A. J. Martin, D. Tien, J. M. Millunchick and V. Sih. Nano letters **11**, 1040 (2011).

[Les95] S. D. Lester, F. A. Ponce, M. G. Craford and D. A. Steigerwald. Applied Physics Letters **66**, 1249 (1995).

[Loc06] A. Lochmann, E. Stock, O. Schulz, F. Hopfer, D. Bimberg, V. A. Haisler, A. I. Toropov, A. K. Bakarov and A. K. Kalagin. Electronics Letters **42**, 22 (2006).

[Mac05] P. Machnikowski and L. Jacak. Physical Review B **71**, 115309 (2005).

[Mar11] A. Marent, T. Nowozin, M. Geller and D. Bimberg. Semiconductor Science and Technology **26**, 014026 (2011).

[Mat05] A. Matsuse, N. Grandjean, B. Damilano and J. Massies. Journal of Crystal Growth **274**, 387 (2005).

[McC98] M. D. McCluskey, N. M. Johnson, C. G. Van de Walle, D. P. Bour, M. Kneissl and W. Walukiewicz. Physical Review Letters **80**, 4008 (1998).

[McW69] R. McWeeny. *Methods of Molecular Quantum Mechanics*. (Academic Press, 1969).

[Mer02] I. A. Merkulov, Al. L. Efros and M. Rosen. Physical Review B **65**, 205309 (2002).

[Mer09] L. O. Mereni, V. Dimastrodonato, R. J. Young and E. Pelucchi. Applied Physics Letters **94**, 223121 (2009).

[Mil85] D. A. B. Miller, D. S. Chelma, T. C. Damen, A. C. Gossard, W. Wiegmann, T. H. Wood and C. A. Burrus. Physical Review B **32**, 1043 (1985).

[Mil86] D. A. B. Miller, D. S. Chelma and S. Schmitt-Rink. Physical Review B **33**, 6976 (1986).

[Moe04] S. Moehl, F. Tinjod, K. Kheng and H. Mariette. Physical Review B **69**, 245318 (2004).

[Moh10a] A. Mohan, M. Felici, P. Gallo, B. Dwir, A. Rudra, J. Faist and E. Kapon. Nature Photonics **4**, 302 (2010).

[Moh10b] A. Mohan, P. Gallo, M. Felici, B. Dwir, A. Rudra, J. Faist and E. Kapon. Small **6**, 1268 (2010).

[MS05] J. Martían-Sánchez, Y. González, L. González, M. Tello, R. García, D. Granados, J.M. García and F. Briones. Journal of Crystal Growth **284**, 313 (2005).

[Mul04] E. Muljarov and R. Zimmermann. Physical Review Letters **93**, 237401 (2004).

[Mul05] E. Muljarov, T. Takagahara and R. Zimmermann. Physical Review Letters **95**, 177405 (2005).

[Mul07] E. Muljarov and R. Zimmermann. Physical Review Letters **98**, 187401 (2007).

[Nak02] T. Nakaoka, S. Kako, S. Ishida, M. Nishioka and Y. Arakawa. Applied Physics Letters **81**, 3954 (2002).

[Nak06a] T. Nakaoka, S. Kako and Y. Arakawa. Physica E: Low-dimensional Systems and Nanostructures **32**, 148 (2006).

[Nak06b] T. Nakaoka, S. Kako and Y. Arakawa. Physical Review B **73**, 121305 (2006).

[Neu00] R. G. Neuhauser, K. T. Shimizu, W. K. Woo, S. A. Empedocles and M. G. Bawendi. Physical review letters **85**, 3301–4 (2000).

[Nir96] M. Nirmal, B. O. Dabbousi, M. G. Bawendi, J.J. Macklin, J. K. Trautman, T. D. Harris and L. E. Brus. Nature **383**, 802 (1996).

[Nöt98] R. Nötzel, N. Zhichuan, M. Ramsteiner, H.-P. Schönherr, A. Tranpert, L. Däweritz and H. K. Ploog. Nature **392**, 56 (1998).

[Noz02] A. J. Nozik. Physica E: Low-dimensional Systems and Nanostructures **14**, 115 (2002).

[Ort04] G. Ortner, D. Yakovlev, M. Bayer, S. Rudin, T. Reinecke, S. Fafard, Z. Wasilewski and A. Forchel. Physical Review B **70**, 201301 (2004).

[Pal03] P. Palinginis, S. Tavenner, M. Lonergan and H. Wang. Physical Review B **67**, 201307 (2003).

[Pan01] N. Panev, M.-E. Pistol, V. Zwiller, L. Samuelson, W. Jiang, B. Xu and Z. Wang. Physical Review B **64**, 045317 (2001).

[Pan02] N. Panev, M.-E. Pistol, S. Jeppesen, V. P. Evtikhiev, A. A. Katznelson and E. Y. Kotelnikov. Journal of Applied Physics **92**, 7086 (2002).

[Per95] P. Perlin, T. Suski, H. Teisseyre, M. Leszczynski, I. Grzegory, J. Jun, S. Porowski, P. Boguslawski, J. Bernholc, J. C. Chervin, A. Polian and T. D. Moustakas. Physical Review Letters **75**, 296 (1995).

[Per09] P. Perlin, G. Franssen, J. Szeszko, R. Czernecki, G. Targowski, M. Krysko, S. Grzanka, G. Nowak, E. Litwin-Staszewska, R. Piotrzkowski, M. Leszczynski, B. Lucznik, I. Grzegory, R. Jakiela, M. Albrecht and T. Suski. Physica Status Solidi (a) **206**, 1130 (2009).

[Pet04] E. Peter, J. Hours, P. Senellart, A. Vasanelli, A. Cavanna, J. Bloch and J.-M. Gérard. Physical Review B **69**, 041307 (2004).

[Pis99] M.-E. Pistol, P. Castrillo, D. Hessman, J. Prieto and L. Samuelson. Physical Review B **59**, 10725 (1999).

[Pis01] M.-E. Pistol. Physical Review B **63**, 113306 (2001).

[Plu11] J. Plumhof, V. Krápek, F. Ding, K. Jöns, R. Hafenbrak, P. Klenovský, A. Herklotz, K. Dörr, P. Michler, A. Rastelli and O. Schmidt. Physical Review B **83**, 121302 (2011).

[Pon02] F. A. Ponce. Defects and interfaces in GaN epitaxy. Seiten vol.22(2), 51, Mater. Res. Soc, 2002.

[Ran03] V. Ranjan, G. Allan, C. Priester and C. Delerue. Physical Review B **68**, 115305 (2003).

[Rei08] S. Reitzenstein, C. Böckler, A. Bazhenov, A. Gorbunov, A. Löffler, M. Kamp, V. D. Kulakovskii and A. Forchel. Optics Express **16**, 4848 (2008).

[Ric04] J. H. Rice, J. W. Robinson, A. F. Jarjour, R. A. Taylor, R. A. Oliver, G. A. D. Briggs, M. J. Kappers and C. J. Humphreys. Applied Physics Letters **84**, 4110 (2004).

[Rin08] P. Rinke, M. Winkelnkemper, A. Qteish, D. Bimberg, J. Neugebauer and M. Scheffler. Physical Review B **77**, 075202 (2008).

[Rob00] H. Robinson and B. Goldberg. Physical Review B **61**, R5086 (2000).

[Rob05] J. W. Robinson, J. H. Rice, K. H. Lee, J. H. Na, R. A. Taylor, D. G. Hasko, R. A. Oliver, M. J. Kappers, C. J. Humphreys and G. A. D. Briggs. Applied Physics Letters **86**, 213103 (2005).

[Rod03] S. Rodt, R. Heitz, A. Schliwa, R. Sellin, F. Guffarth and D. Bimberg. Physical Review B **68**, 035331 (2003).

[Rod05] S. Rodt, A. Schliwa, F. Guffarth and D. Bimberg. Physical Review B **71**, 155325 (2005).

[Rod06] S. Rodt. *Exzitonische Komplexe in einzelnen III-V Quantenpunkten*. PhD thesis, Technischen Universität Berlin, Germany, 2006.

[Rol06] F. Rol, B. Gayral, S. Founta, B. Daudin, J. Eymery, J.-M. Gérard, H. Mariette, Le Si Dang and D. Peyrade. Physica Status Solidi (b) **243**, 1652 (2006).

[Rol07] F. Rol, S. Founta, H. Mariette, B. Daudin, Le Si Dang, J. Bleuse, D. Peyrade, J.-M. Gérard and B. Gayral. Physical Review B **75**, 125306 (2007).

[Ros97] S. J. Rosner, E. C. Carr, M. J. Ludowise, G. Girolami and H. I. Erikson. Applied Physics Letters **70**, 420 (1997).

[Ros99] A. Rosenauer and D. Gerthsen. Advances in Imaging and Electron Physics **107**, 121 (1999).

[Rud90] S. Rudin, T. Reinecke and B. Segall. Physical Review B **42**, 11218 (1990).

[Ruf07] S. Ruffenach, O. Briot, M. Moret and B. Gil. Applied Physics Letters **90**, 153102 (2007).

[Sai02] T. Saito and Y. Arakawa. Physica E: Low-dimensional Systems and Nanostructures **15**, 169 (2002).

[Sal10a] G. Sallen, A. Tribu, T. Aichele, R. André, L. Besombes, C. Bougerol, M. Richard, S. Tatarenko, K. Kheng and J.-Ph. Poizat. Nature Photonics **4**, 696 (2010).

[Sal10b] C. L. Salter, R. M. Stevenson, I. Farrer, C. A. Nicoll, D. A. Ritchie and A. J. Shields. Nature **465**, 594 (2010).

[Sch07a] A. Schliwa, M. Winkelnkemper and D. Bimberg. Physical Review B **76**, 205324 (2007).

[Sch07b] O. Schmidt. *Lateral alignment of epitaxial quantum dots*. Nanoscience and technology. (Springer, 2007).

[Sch08a] A. Schliwa, M. Winkelnkemper and D. Bimberg. Nr. 10 2008 036 400.2, German Patent Application, 2008.

[Sch08b] C. Schneider, M. Strauß, T. Sünner, A. Huggenberger, D. Wiener, S. Reitzenstein, M. Kamp, S. Höfling and A. Forchel. Applied Physics Letters **92**, 183101 (2008).

[Sch09a] A. Schliwa, M. Winkelnkemper and D. Bimberg. Physical Review B **79**, 075443 (2009).

[Sch09b] Andrei Schliwa, Momme Winkelnkemper, Anatol Lochmann, Erik Stock and Dieter Bimberg. Physical Review B **80**, 075443 (2009).

[Sch09c] C. Schneider, T. Heindel, A. Huggenberger, P. Weinmann, C. Kistner, M. Kamp, S. Reitzenstein, S. Höfling and A. Forchel. Applied Physics Letters **94**, 111111 (2009).

[Seg04] R. Seguin, S. Rodt, A. Strittmatter, L. Reiß mann, T. P. Bartel, A. Hoffmann, D. Bimberg, E. Hahn and D. Gerthsen. Applied Physics Letters **84**, 4023 (2004).

[Seg05] R. Seguin, A. Schliwa, S. Rodt, K. Pötschke, U. Pohl and D. Bimberg. Physical Review Letters **95**, 257402 (2005).

[Seg06] R. Seguin, A. Schliwa, T. D. Germann, S. Rodt, K. Pötschke, A. Strittmatter, U. W. Pohl, D. Bimberg, M. Winkelnkemper, T. Hammerschmidt and P. Kratzer. Applied Physics Letters **89**, 263109 (2006).

[Sei06] S. Seidl, M. Kroner, A. Högele, K. Karrai, R. J. Warburton, A. Badolato and P. M. Petroff. Applied Physics Letters **88**, 203113 (2006).

[Sem03] Y. G. Semenov and K. W. Kim. Physical Review B **67**, 073301 (2003).

[Seu00] J. Seufert, R. Weigand, G. Bacher, T. Kümmell, A. Forchel, K. Leonardi and D. Hommel. Applied Physics Letters **76**, 1872 (2000).

[Shc95] V. A. Shchukin, N. N. Ledentsov, P. S. Kop'ev and D. Bimberg. Physical Review Letters **75**, 2968 (1995).

[Shc98] V.A. Shchukin and D. Bimberg. Applied Physics A: Materials Science and Processing **67**, 687 (1998).

[Shc04] V. A. Shchukin, D. Bimberg, T. P. Munt and D. E. Jesson. Physical Review B **70**, 085416 (2004).

[Shi07] A. J. Shields. Nature Photonics **1**, 215 (2007).

[Sim03] J. Simon, N. Pelekanos, C. Adelmann, E. Martinez-Guerrero, R. André, B. Daudin, Le Si Dang and H. Mariette. Physical Review B **68**, 035312 (2003).

[Sim08a] D. Simeonov. *Study on Optical Polarization in Hexagonal Gallium Nitride Quantum Dots*. PhD in physics, Ecole Polytechnique Fédérale de Lausanne, IPEQ, Lausanne, Switzerland, 2008.

[Sim08b] D. Simeonov, A. Dussaigne, R. Butté and N. Grandjean. Physical Review B **77**, 075306 (2008).

[Sin03] J. Singh. *Electronic and Optoelectronic Properties of Semiconductor Structures*. 1st Edition. (Cambridge University Press, 2003).

[Sin09] R. Singh and G. Bester. Physical Review Letters **103**, 063601 (2009).

[Sla74] J. C. Slater. *The Self-consistent Field for Molecules and Solids: Quantum Theory of Molecules and Solids*. Nanoscience and technology. (McGraw-Hill, 1974).

[Sme03] T. M. Smeeton, M. J. Kappers, J. S. Barnard, M. E. Vickers and C. J. Humphreys. Applied Physics Letters **83**, 5419 (2003).

[SR87] S. Schmitt-Rink, D. A. B. Miller and D. S. Chelma. Physical Review B **35**, 8113 (1987).

[SS11] J. Skiba-Szymanska, A. Jamil, I. Farrer, M. B. Ward, C. A. Nicoll, D. J. P. Ellis, J. P. Griffiths, D. Anderson, G. A. C. Jones, D. A. Ritchie and A. J. Shields. Nanotechnology **22**, 065302 (2011).

[Sti99] O. Stier, M. Grundmann and D. Bimberg. Physical Review B **59**, 5688 (1999).

[Sti01] O. Stier, a. Schliwa, R. Heitz, M. Grundmann and D. Bimberg. Physica Status Solidi (b) **224**, 115 (2001).

[Sto10] T. Stock, E. andl Warming, I. A. Ostapenko, S. Rodt, A. Schliwa, J. A. Tofflinger, A. Lochmann, A. I. Toropov, S. A. Moshchenko, Dmitriev. D. V., V. A. Haisler and D. Bimberg. Applied Physics Letters **96**, 093112 (2010).

[Sto11] E. Stock, M.-R. Dachner, T. Warming and A. Schliwa. Physical Review B **83**, 041304 (2011).

[Sug98] T. Sugahara, H. Sato, M. Hao, Y. Naoi, S. Kurai, S. Tottori, K. Yamashita, K. Nishino, L. T. Romano and S. Sakai. Japanese Journal of Applied Physics **37**, L398 (1998).

[Sug99] M. Sugisaki, H.-W. Ren, S. Nair, K. Nishi, S. Sugou, T. Okuno and Y. Masumoto. Physical Review B **59**, R5300 (1999).

[Sün08] T. Sünner, C. Schneider, M. Strauss, A. Huggenberger, D. Wiener, S. Höfling, M. Kamp and A. Forchel. Optics Letters **33**, 1759 (2008).

[Tac99] K. Tachibana, T. Someya, Y. Arakawa, R. Werner and A. Forchel. Applied Physics Letters **75**, 2605 (1999).

[Tak93] T. Takagahara. Physical Review Letters **71**, 3577 (1993).

[Tak98] T. Takeuchi, C. Wetzel, S. Yamaguchi, H. Sakai, H. Amano, I. Akasaki, S. Kaneko, Y .and Nakagawa, Y. Yamaoka and N. Yamada. Applied Physics Letters **73**, 1691 (1998).

[Tak99] T. Takagahara. Physical Review B **60**, 2638 (1999).

[Toy93] H. Toyoshima, T. Niwa, J. Yamazaki and a. Okamoto. Applied Physics Letters **63**, 821 (1993).

[Tsi05] E. Tsitsishvili, R. v. Baltz and H. Kalt. Physical Review B **72**, 155333 (2005).

[Tür00a] V. Türck, S. Rodt, O. Stier, R. Heitz, R. Engelhardt, U. Pohl, D. Bimberg and R. Steingrüber. Physical Review B **61**, 9944 (2000).

[Tür00b] V. Türck, S. Rodt, O. Stier, R. Heitz, U.W. Pohl, R. Engelhardt and D. Bimberg. Journal of Luminescence **87-89**, 337 (2000).

[Tür01] V. Türck. *Elektronische Eigenschaften einzelner Halbleiterquantenpunkte*. Dissertation, Technische Universität Berlin. (Mensch und Buch Verlag, 2001).

[Usk00] A. V. Uskov, A. Jauho, B. Tromborg, J. Mork and R. Lang. Physical review letters **85**, 1516 (2000).

[Vag11] A. Vagov, M. D. Croitoru, V. M. Axt, P. Machnikowski and T. Kuhn. Physica Status Solidi (b) **248**, 839 (2011).

[Van04] C. G. Van de Walle and J. Neugebauer. Journal of Applied Physics **95**, 3851 (2004).

[VdW98] C. G. Van de Walle. Physical Review B **57**, R2033 (1998).

[Vog07] M. M. Vogel, S. M. Ulrich, R. Hafenbrak, P. Michler, L. Wang, A. Rastelli and O. G. Schmidt. Applied Physics Letters **91**, 051904 (2007).

[Vur03] I. Vurgaftman and J. R. Meyer. Journal of Applied Physics **94**, 3675 (2003).

[Wan04] C. F. Wang, A. Badolato, I. Wilson-Rae, P. M. Petroff, E. Hu, J. Urayama and A. Imamoglu. Applied Physics Letters **85**, 3423 (2004).

[Wat04] S. Watanabe, E. Pelucchi, B. Dwir, M. H. Baier, K. Leifer and E. Kapon. Applied Physics Letters **84**, 2907 (2004).

[Wet97] C. Wetzel, T. Suski, J. W. Ager III, E. R. Weber, E. E. Haller, S. Fischer, B. K. Meyer, R. J. Molnar and P. Perlin. Physical Review Letters **78**, 3923 (1997).

[Wid98] F. Widmann, J. Simon, B. Daudin, G. Feuillet, J. Rouviere, N. Pelekanos and G. Fishman. Physical Review B **58**, R15989 (1998).

[Wil01] A. J. Williamson, A. Franceschetti and Al. Zunger. Europhysics Letters **53**, 59 (2001).

[Wil04] D.P. Williams, A.D. Andreev and E.P. O'Reilly. Superlattices and Microstructures **36**, 791 (2004).

[Win06] M. Winkelnkemper, A. Schliwa and D. Bimberg. Physical Review B **74**, 155322 (2006).

[Win07] M. Winkelnkemper, R. Seguin, S. Rodt, A. Schliwa, L. Reiß mann, A. Strittmatter, A. Hoffmann and D. Bimberg. Journal of Applied Physics **101**, 113708 (2007).

[Win08] M. Winkelnkemper, R. Seguin, S. Rodt, A. Hoffmann and D. Bimberg. Journal of Physics: Condensed Matter **20**, 454211 (2008).

[Woo02] L. Woods, T. Reinecke and Y. Lyanda-Geller. Physical Review B **66**, 161318 (2002).

[Yac86] B.G. Yacobi and D.B. Holt. Journal of Applied Physics **59**, R1 (1986).

[Yi96] G.-C. Yi and B. W. Wessels. Applied Physics Letters **68**, 3769 (1996).

[You05] R. J. Young, R. M. Stevenson, A. J. Shields, P. Atkinson, K. Cooper, D. A. Ritchie, K. M. Groom, A. I. Tartakovskii and M. S. Skolnick. Physical Review B **72**, 113305 (2005).

[Zim02] R. Zimmermann and E. Runge. Dephasing in quantum dots via electron-phonon interaction. In A. R. Long and J. H. Davies, Hrsg., *Proc. 26th ICPS Edinburgh*, Band 171 von *IOP Conf. Series*, IOP Publishing Bristol (UK), 2002.

	Nitride-based QDs				Positioned InGaAs/GaAs QDs
Name in this work	***T***	***L***	***B***	***W***	
QD material	GaN		In-concentrations fluctuations in InGaN		InGaAs
Active layer	6.4 ML	5 ML	8 ML	indeterminable	2 ML
Matrix material	AlN		InGaN/GaN	InGaN	GaAs
Substrate	SiC	GaN	Si(111)	GaN with miscut of 2.3 °	GaAs
Growth technique	MOCVD	MBE	MOCVD	MBE	MOCVD
Original name	unknown	L29	tu6938	nb1372C	np4513
Origin	University of Tokyo	ÉPFL	TU Berlin	Unipress, Poland	TU Berlin